

Investigation of electrokinetic forces on single particles

DISSERTATION

zur Erlangung des Grades eines Doktors
der Naturwissenschaften

vorgelegt von

Dipl.-Ing. Elmar Bonaccorso

aus Brunico/Bruneck

eingereicht beim Fachbereich 8
der Universität-Gesamthochschule-Siegen
Siegen 2001

1. Gutachter: Prof. Dr. H.-J. Butt, Universität Siegen
2. Gutachter: Prof. Dr. A. Meixner, Universität Siegen
3. Mitglied der Promotionskommission: Prof. M. Grattarola, Università degli Studi di Genova

Datum der mündlichen Prüfung: 15. Dezember 2001

Index

Index	III
Introduction	1
Motivation	5
1 Fundamentals	6
1.1 Surface Forces	6
1.1.1 Forces between atoms and molecules	6
1.1.2 The van der Waals force between two molecules	7
1.1.3 The van der Waals energy between macroscopic solids	8
1.2 Electrostatic Force	9
1.2.1 Gouy-Chapman theory of the electric double layer	10
1.2.2 Debye-Hückel theory	13
1.2.3 Electrostatic Force – Derjaguin's Approximation	13
1.3 Hydrodynamic Force	14
1.4 Electrokinetic Force	18
1.5 AFM and SFA	20
1.5.1 Surface Force Apparatus	20
1.5.2 Atomic Force Microscope	21
1.5.3 AFM vs. SFA	22
2 Materials and Methods	24
2.1 Particle Interaction Apparatus (PIA)	24
2.2 Cantilevers and Spheres	27
2.3 Chemicals	27
2.4 Probe Preparation and Cleaning	28
2.5 Cantilever Calibration	30
2.5.1 Added mass method	30
2.5.2 Sader method	31
2.5.3 Reference spring method	33
2.5.4 Comparison of the calibration procedures	35
2.6 Force Curves and their Evaluation	35
2.6.1 Force versus distance curves and sphere-sample interaction force	36
2.6.2 Hydrodynamic force curves	39
2.7 Simulation of Force Curves	40
2.7.1 Electrostatic force	40
2.7.2 Hydrodynamic force	42
2.7.3 Electrokinetic force	44

3	Cantilever Fabrication Process	46
3.1	Types of Cantilevers and Materials	46
3.2	Coating Techniques	47
3.2.1	Thermal oxidation	47
3.2.2	Chemical vapour deposition (CVD)	48
3.2.3	Physical vapour deposition (PVD)	48
3.3	Structuring Techniques	48
3.3.1	Photolithography	49
3.3.2	Chromium mask	49
3.3.3	Etching processes	51
3.3.3.1	Dry etching	51
3.3.3.2	Wet etching	51
3.3.3.3	Silicon wet etching	52
3.4	Example of Flow-Chart for poly-silicon Cantilevers	52
4	Results and Discussion	55
4.1	The Electric Double Layer on Oxide Surfaces and Mica	56
4.2	Hysteresis in High-Speed Force Curves	57
4.3	The Hydrodynamic Force	58
4.4	The Electrostatic Force	67
4.5	The Electrokinetic Force	69
	Conclusions	73
	Bibliography	75
	Acknowledgements	77
	List of used mathematical symbols, constants and abbreviations	79

Introduction

Or: Why are colloidal systems important?

Evidence of man's use of colloids dates back to the earliest records of civilisation. Stone age paintings and written records of old Egyptians on papyrus were produced with stabilised colloidal pigments. Many early technological processes, such as papermaking, pottery, fabrication of soaps and cosmetics, involved manipulation of colloidal systems. The establishment of colloid science as a scientific discipline can be dated back to 1845, when Francesco Selmi described the first examples of colloidal particles. By defining their common properties, he called solutions like silver chloride, sulfur and prussian blue in water "pseudosolutions". In the 1850s Michael Faraday made extensive studies of colloidal gold sols, which he found to be thermodynamically unstable. Once they have coagulated, the process cannot be reversed. For this reason, such insoluble dispersions are called *lyophobic* (liquid hating) *colloids*. In 1861 Thomas Graham coined the term *colloid* (which means "glue" in Greek) to describe Selmi's pseudosolutions. The term emphasises their low rate of diffusion and lack of crystallinity. Graham deduced that the low diffusion rates of colloidal particles implied that they were fairly large, at least 1 nm in diameter. On the other hand, the fact that the particles did not sediment under the influence of gravity implied that they had an upper size limit of approximately 1 μm . This definition of particle sizes which characterise the colloidal domain is still widely used today.

Colloidal phenomena played an important role in the development of physical chemistry. For example, the discovery of Brownian motion resulted from the observation of colloidal-sized pollen particles by light microscopy. Later, Marian Smoluchowski derived an expression that related the kinetics of rapid coagulation of colloidal particles (in which each Brownian encounter between two particles resulted in permanent contact) to the formation of larger aggregates. His expression was extended to explain the role of diffusion in bimolecular reactions in general.

These fundamental developments encouraged an extensive use of colloidal systems by the industry. Compositions of paints and other coatings were improved, sophisticated ceramics were developed, use of emulsions increased, novel uses were found for newly discovered polymer molecules. However, the complexity of these practical systems far exceeded the ability of theoreticians to explain them, and to a large extent colloids remained an empirically descriptive field.

Significant advances in explaining the stability of colloidal sols were made in 1945. Publication of the *Derjaguin-Landau* and *Verwey-Overbeek* (DLVO) theory provided a quantitative relationship between the attractive van der Waals forces, which lead to coagulation, and the repulsive electrostatic forces, which stabilise colloidal dispersions. The DLVO theory nowadays constitutes a cornerstone of colloid science.

The behaviour of many colloidal systems is successfully explained by the well established *DLVO theory* (Derjaguin, Landau, Verwey, Overbeek) [1, 2, 3]. This theory describes the interactions between colloids in polar media in terms of attractive van der Waals and repulsive electric double layer (*EDL*) forces. The theory, however, describes systems at equilibrium: The energy of the interactions between particles is calculated assuming the quasi-static approach from infinity to a given distance. In most practical applications particles are subjected to motion, hence also the hydrodynamic effects should be taken into account. This was first recognised by Derjaguin, Muller and Spielman. They explained that the rate of fast coagulation was always below the one predicted by Smoluchowski. This is a result of the increased hydrodynamic drag exerted on a particle approaching a second one. I would like to start from this point, first developing independently the theories of hydrodynamic and electrostatic interactions, then coupling the two effects to obtain a description of an electrokinetic colloidal system.

It is commonly accepted that the liquid layer in contact with a solid interface (extended flat surface as well as spherical particle) assumes the velocity of the solid. This is known as the *no-slip boundary condition* and is widely used in science and engineering to model a broad spectrum of fluid flows. Though successful in many applications, this description fails in other situations, e.g. in the case of microscopic flows in confined geometries, the spreading of a liquid on a solid substrate [4, 5, 6, 7, 8, 9], corner flow [10, 11], extrusion of polymers from a capillary tube [12, 13]. Here it has been observed that the liquid molecules "slip" over the surfaces, and therefore a more general *boundary condition* must be applied.

There exist several experimental techniques to investigate colloidal interactions, such as the impinging jet cell [14], the surface force apparatus [15] and the colloidal probe technique. The last is a well-established method for exploring particle-wall and particle-particle interactions in liquids [42, 43]. A microsphere is attached to an atomic force microscope cantilever. Then it is moved towards a flat surface, or towards another particle,

and the force acting on the sphere is measured by monitoring the deflection of the cantilever. Approaching speeds in these experiments can vary from few tenths of nanometers per second (no evidence of hydrodynamic effects), up to about a hundred of micrometers per second (strong hydrodynamic effects). In recent years the possibility to use the colloidal probe technique to measure these hydrodynamic forces has been explored [44, 82].

In this work I describe results of dynamic force experiments between charged and uncharged hydrophilic colloids and surfaces in aqueous medium. The hydrodynamic force and the electric double layer force dominate the total interaction. The purpose of these measurements was twofold: First, I intended to test the validity of the no-slip boundary condition for the water at a hydrophilic interface; second, whether at high approaching velocities special electrokinetic effects arise.

The structure of the thesis is the following:

In **chapter one** I present the theory of surface forces and forces acting between atoms, molecules and macroscopic solids. I introduce as well the basics of the three forces relevant for this work: *Hydrodynamic force* (affecting colloidal particles in motion inside a liquid), *electrostatic force* (affecting charged, immobile colloidal particles inside electrolytic solutions), and the *electrokinetic force* (affecting charged colloidal particles moving inside electrolytic solutions).

In **chapter two** I give an overview of the devices used for the surface force measurements and describe the materials used for the experiments (cantilevers, microspheres, and chemicals). I also specify the techniques used for preparation of the probes, realisation of the measurements, simulation and evaluation of the results.

In **chapter three** I present the steps for developing and fabricating the cantilever sensors, along with an overview of the most used materials and of the common forms of microcantilevers. I give an insight in some simple silicon micro machining processes and describe briefly the involved technology. An example of a flow chart for the production of poly-crystalline silicon cantilevers completes the chapter.

In **chapter four** I provide detailed descriptions of the performed hydrodynamic, electrostatic and electrokinetic measurements. The slip vs. no-slip boundary condition is discussed. The additivity of electrostatic and hydrodynamic forces is examined. Numerical

simulations following the theory are presented and compared with experimental data. Interpretations of the measurements are provided.

Finally, in **chapter five** I summarise the main aspects of theory and experiments, and draw the conclusions.

Motivation

The aim of this work is to show that in many aspects of colloidal systems there exists a coupling between hydrodynamic and electrostatic interactions. I will show that for charged particles immersed in a polar medium, there is a pronounced influence of the electric field upon the motion of the particle in the fluid. Experimentally, this leads to *electrokinetic effects*, which may influence the coagulation of colloid particles and their adsorption at surfaces. These effects can be described by extending the equations of motion by an additional electrostatic term.

This work also gives evidence of the existence of the hydrodynamic phenomenon of slip between hydrophilic bodies in an aqueous medium. Recently, more general boundary conditions, differing from the *no-slip boundary condition*, have been proposed. Due to the experiments presented here, the more general boundary conditions have to be considered only for shear stresses which the liquid experiences in the vicinity of the solid interfaces.

In order to carry out these specific measurements, I designed and attended the fabrication of new types of rectangular tipless cantilevers. These have the advantage, with respect to commercial triangular cantilevers, of affecting less, or in a more predictable way, the hydrodynamics of the microsphere in vicinity of the flat surface. These home made cantilevers have also a higher sensitivity in the specific range of forces I'm interested in detecting ($0.1 \div 10$ nN).

1 Fundamentals

1.1 Surface Forces

Surface forces are the forces that act between the surfaces of two solids. Gravity does not belong to them, since the mass of the solids (which is the cause of gravity), is distributed over the whole volume. In the strict sense also the van der Waals force should not be counted to the group. It can, however, be formally treated as a surface force since it is important in many applications of the research on colloids.

Surface forces do not only determine the behaviour of dispersions, emulsions, foams and sols, but also that of phenomena like wetting, adhesion and adsorption. Useful overviews are found in [15, 16].

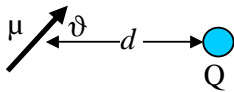
1.1.1 Forces between atoms and molecules

The cause for all surface forces is the *Coulomb force*. The potential energy between two electric charges in vacuum is

$$V = \frac{Q_1 Q_2}{4\pi\epsilon_0 \cdot d} \quad (1.1)$$

where Q_1 and Q_2 are the charges in Coulomb, d is the distance between them and ϵ_0 is the permittivity of free space.

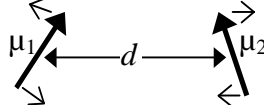
With Coulomb's force law one can deduce the potential energy between a dipole of dipole moment μ and a single charge

$$V = -\frac{Q\mu \cdot \cos \vartheta}{4\pi\epsilon_0 \cdot d^2} \quad (1.2)$$


The energy depends on the orientation. In practice the molecule with the dipole moment is mobile. For a free rotating dipole, which interacts with a single charge, the energy is

$$V = -\frac{Q^2 \mu^2}{6(4\pi\epsilon_0)^2 k_B T d^4} \quad (1.3)$$

Also two free rotating dipoles interact with each other. This is often referred to as the *Keesom energy* [17]:

$$V = -\frac{\mu_1^2 \mu_2^2}{3(4\pi\epsilon_0)^2 k_B T} \frac{1}{d^6}$$

(1.4)

When a charge approaches a molecule without a static dipole moment, then all energies considered so far would be zero. Nevertheless, there is an attractive force. An explanation can be that the charge induces a charge shift in the non-polar molecule. Thus an induced dipole moment interacts with the charge with the energy

$$V = -\frac{Q^2 \alpha}{2(4\pi\epsilon_0)^2} \frac{1}{d^4}$$
(1.5)

α is the polarizability defined by $\mu_{ind} = \alpha E$, where E is an external applied electric field and μ_{ind} is the dipole moment induced by the electric field, and is expressed in $C^2 m^2 J^{-1}$

Also a molecule with a static dipole moment interacts with a polarisable molecule. If the dipole can freely rotate the energy is

$$V = -\frac{\mu^2 \alpha}{(4\pi\epsilon_0)^2} \frac{1}{d^6}$$
(1.6)

This is called the *Debye energy* [18].

All energies considered until now can be calculated in a classical way. Unfortunately they do not completely explain the interaction between molecules, e.g. the attraction between two non-polar molecules. This interaction can be understood only in the context of quantum mechanics. The static dipole moment, which occurs in the equation of the Debye energy, is replaced by a fluctuating dipole moment in quantum mechanics. The reason for this fluctuation is the uncertainty principle. The fluctuating dipole polarises neighbouring molecules, leading to an attraction.

The energy between two molecules with the ionisation energies $h\nu_1$ and $h\nu_2$ amounts to

$$V = -\frac{3}{2} \frac{\alpha_1 \alpha_2}{(4\pi\epsilon_0)^2} \frac{1}{d^6} \frac{h\nu_1 \nu_2}{(\nu_1 + \nu_2)}$$
(1.7)

This is called the *London dispersion energy* [19]. The equation is an approximation. It is crucial that the energy grows proportionally with the polarizability of the two atoms, and that the optical characteristics enter in the form of the excitation frequencies.

1.1.2 The van der Waals force between two molecules

The *van der Waals* (vdW) force is the sum of the *Keesom*, the *Debye* and the *London* dispersion interaction, i.e. all the terms that consider dipole interactions. All three terms

contain the same distance dependence: The potential energy decreases with d^{-6} . Usually the London dispersion term is dominating.

So far I had assumed that the molecules stay so close that the propagation of the electric field is instantaneous: A dipole moment arises in a molecule, which in turn generates an electric field. The electric field expands with light speed. It polarises a second molecule in the vicinity, whose dipole moment in turn causes an electric field that reaches the first molecule with light speed. In this way the two molecules interact (*non-retarded vdW interaction*).

The process takes place as calculated only if the electric field has enough time to cover the distance d between the molecules. It takes a time $\Delta t = d/c$, where c is the speed of the light. If the alignment of the first dipole is quicker than Δt then the interaction becomes weaker. The time during which the dipole moment changes is about $1/\nu$. Hence, only if

$$\frac{d}{c} < \frac{1}{\nu}$$

the interaction takes place as considered. From $c = \lambda\nu$ follows $d < \lambda$. As a consequence, for distances greater than 10 ÷ 100 nm the vdW energy drops more rapidly (for molecules as d^{-7}) as for smaller distances (*retarded vdW interaction*).

1.1.3 The van der Waals energy between macroscopic solids

There are two approaches to calculate the vdW force between extended solids: The microscopic and the macroscopic [20].

In the microscopic approach, one calculates the interaction energy between two macroscopic solids by pair wise addition of all single potential energies between a molecule in solid A and every molecule in solid B. Practically, this is done via an integration of the molecular density ρ_{solid} over the entire volume of the solid. If we write the attractive and therefore negative potential energy V_{AB} in the general form as

$$V_{AB}(d) = -\frac{C_{AB}}{d^6} \quad (1.8)$$

this results in

$$V_{Mol/plane} = -\frac{\pi C_{AB} \rho_{solid}}{6d^3} \quad (1.9)$$

The minus sign arises because of the attraction. C_{AB} is a positive term.

The nature of this energy is of longer range compared to the potential of the single molecules because this interaction is not only determined by the closest surface molecules but also by the molecules in the bulk.

To calculate the vdW energy between two infinitely extended solids A and B , separated by a parallel gap of the thickness d equation (1.9) is integrated over all the molecules in the solid A , which results in

$$\frac{V}{A} = -\frac{A_{AB}}{12\pi} \frac{1}{d^2} \quad (1.10)$$

where $A_{AB} = \pi^2 C_{AB} \rho_A \rho_B$ is the so-called *Hamaker constant*.

In a similar way it is possible to calculate the vdW energy between solids having different geometries, like e.g. a spherical shape.

In the microscopic consideration additivity of the single potentials is assumed, although this is not correct: The vdW energy between two molecules is changed in the presence of a third molecule. In the **macroscopic Lifshitz theory** this is considered by neglecting the atomic structure, and treating the solids as continuous media with certain optical properties.

Lifshitz obtained the same expression (1.10), especially the distance dependency. But the Hamaker constant is calculated in a different way.

So far I considered the interaction of atoms, molecules or solids in vacuum. Now, I want to depict the interaction of solid surfaces in fluids with respect to water.

1.2 Electrostatic Force

In water, surface charges are generated between the interacting solids when ions are adsorbed at their surfaces or when groups dissociate. Many oxides, like SiO_2 , TiO_2 , Al_2O_3 , have surface hydroxyl groups. They can dissociate protons ($\text{OH} \rightarrow \text{O}^- + \text{H}^+$) and leave back negative surface charges which cause an electric field. This field attracts counter ions, thus forming a layer of surface charges and counter ions within the water called *electric double layer* (EDL). This EDL is characterised by the electrostatic surface potential Ψ_0 . The first theory for a quantitative description of the electric double layer came from Helmholtz. He stated that a layer of counter ions directly binds to the charges in a plain, extended surface and their charge exactly compensates that of the surface charges. The electric field generated by the surface charges is accordingly limited to the thickness of this

molecular layer of counter ions. With this model Helmholtz could interpret measurements of the capacity of double layers. Gouy and Chapman went a step further: They considered the thermal motion of the counter ions in the water. This thermal motion leads to the formation of a diffuse layer, which is extended to the water in contrast to the Helmholtz layer. Gouy and Chapman applied their theory to the electric double layer of planes [21, 22, 23]. There, the electrostatic potential as well as the charge density ρ_e is a function of the distance from the surface. Later, Debye and Hückel applied their theory to spheres [24]. In the following, I want to sketch the derivation by Gouy and Chapman to get an expression for the electrostatic potential Ψ at any given distance from the surface.

1.2.1 Gouy-Chapman theory of the electric double layer

The Poisson-Boltzmann equation

I consider a plain charged surface with homogeneously distributed charges and a surface charge density σ , exposed to a liquid. Generally, the charge density ρ_e at a certain place and the electric potential Ψ are related through the *Poisson equation*

$$\nabla^2 \Psi = \frac{\partial^2 \Psi}{\partial x^2} + \frac{\partial^2 \Psi}{\partial y^2} + \frac{\partial^2 \Psi}{\partial z^2} = -\frac{\rho_e}{\epsilon \epsilon_0} \quad (1.11)$$

The Poisson equation enables us to calculate the potential distribution once the positions of all charges are known. The complication is that the ions in solution are free to move. Since their distribution, and thus the charge distribution in the liquid, is unknown, the potential cannot be determined by applying the Poisson equation alone. Additional information is required. This additional formula is the *Boltzmann equation*, which starts from the idea that an electric work W_i has to be done in order to bring an ion in solution from far away closer to the surface. The local ion density would be

$$n_i = n_i^0 \cdot e^{-W_i/kT} \quad (1.12)$$

n_i^0 is the density of the i^{th} ion sort in the volume phase far away from the surface, given in particles/m³. The local ion concentration depends on the electrical potential at the respective place. Now I assume that only electrical work must be performed, neglecting for instance that the ion must displace other molecules. A 1:1 salt is assumed to be dissolved in the liquid. The electrical work required to bring a charged cation to a place with potential Ψ is $W^+ = q_e \Psi$. For an anion it is $W^- = -q_e \Psi$.

The local anion and cation concentrations n^- and n^+ are related with the local potential Ψ through the *Boltzmann factor*:

$$\begin{aligned} n^- &= n_0 \cdot e^{q_e \Psi / k_B T} \\ n^+ &= n_0 \cdot e^{-q_e \Psi / k_B T} \end{aligned} \quad (1.13)$$

n_0 is the volume concentration of the salt. The local charge density is

$$\rho_e = q_e (n^+ - n^-) = n_0 q_e \cdot \left(e^{\frac{q_e \Psi}{k_B T}} - e^{-\frac{q_e \Psi}{k_B T}} \right) \quad (1.14)$$

Substituting the charge density into the Poisson equation gives the *Poisson-Boltzmann equation*

$$\nabla^2 \Psi = \frac{n_0 q_e}{\epsilon \epsilon_0} \cdot \left(e^{\frac{q_e \Psi(x,y,z)}{k_B T}} - e^{-\frac{q_e \Psi(x,y,z)}{k_B T}} \right) \quad (1.15)$$

This is a partial differential equation of second order. Except for some simple cases, it cannot be solved analytically.

One dimensional geometry, small potentials

A simple case is the one-dimensional situation of a flat, infinitely extended plane. In this case the Poisson-Boltzmann equation only contains the z coordinate vertical to the plane

$$\frac{d^2 \Psi}{dz^2} = \frac{n_0 q_e}{\epsilon \epsilon_0} \cdot \left(e^{\frac{q_e \Psi(z)}{k_B T}} - e^{-\frac{q_e \Psi(z)}{k_B T}} \right) \quad (1.16)$$

This equation can be solved for arbitrary potentials, but for by "small" potentials, i.e. for

$$q_e |\Psi_0| \ll k_B T$$

it can be linearised, after expanding eq. (1.16) into a Taylor series

$$\frac{d^2 \Psi}{dz^2} = \frac{n_0 q_e}{\epsilon \epsilon_0} \cdot \left(1 + \frac{q_e \Psi}{k_B T} - 1 + \frac{q_e \Psi}{k_B T} \pm \dots \right) \approx \frac{2n_0 q_e^2}{\epsilon \epsilon_0 k_B T} \cdot \Psi \quad (1.17)$$

neglecting terms of higher order. At room temperature this is valid for ≈ 25 mV or often even for higher potentials, up to approximately $50 \div 80$ mV.

This is sometimes called the *linearised Poisson-Boltzmann equation*. The general solution of the linearised Poisson-Boltzmann equation is

$$\Psi(x) = C_1 \cdot e^{-\kappa z} + C_2 \cdot e^{\kappa z} \quad (1.18)$$

where

$$\kappa = \sqrt{\frac{2n_0 q_e^2}{\epsilon \epsilon_0 k_B T}} \quad (1.19)$$

is the *Debye-Hückel parameter*, C_1 and C_2 are constants which are defined by boundary conditions. For a simple double layer the boundary conditions are

$$\begin{aligned}\Psi(z \rightarrow \infty) &= 0 \\ \Psi(z = 0) &= \Psi_0\end{aligned}$$

The first boundary condition guarantees that at very large distances the potential disappears. From this follows $C_2 = 0$. From the second boundary condition follows $C_1 = \Psi_0$. Hence, the potential is given by the *Debye-Hückel equation*

$$\Psi = \Psi_0 \cdot e^{-\kappa z} \quad (1.20)$$

The potential decreases exponentially. The typical decay length is given by

$$\lambda_D = \kappa^{-1} \quad (1.21)$$

which is called the *Debye length*.

The Debye length decreases with increasing salt concentration. That is intuitively clear: The more ions are in the solution, the more effective is the shielding of the surface charge. If one quantifies all the factors for water at room temperature, then for a monovalent salt with concentration c the Debye length is $\lambda_D = 0.304/\sqrt{c}$ (the result is in nm), with c in mol/l. At a concentration of NaCl of 0.1 M $\lambda_D = 0.95$ nm. Through the dissociation of water, in accordance with $2H_2O \rightarrow H_3O^+ + OH^-$, the ion concentration cannot decrease below 10^{-7} M and therefore λ_D never exceeds 960 nm.

The *Grahame equation* relates in a simple way surface charge σ and surface potential Ψ_0

$$\sigma = \sqrt{8n_0 \epsilon \epsilon_0 k_B T} \cdot \sinh\left(\frac{q_e \Psi_0}{2k_B T}\right) \quad (1.22)$$

which can be further simplified, for small potentials ($\Psi_0 \leq 25$ mV), to give the relation

$$\sigma = \frac{\epsilon \epsilon_0 \Psi_0}{\lambda_D} \quad (1.23)$$

For an aqueous environment the Gouy-Chapman theory provides relatively good predictions for monovalent salts with concentrations below 0.2 M and for potentials below $50 \div 80$ mV. The fact that in reality the surface charge is not continuously but discretely distributed leads to small deviations with bivalent and trivalent charges. When the surface charges do not lie precisely in one plane (e.g. in biological membranes) larger deviations might occur.

1.2.2 Debye-Hückel theory

The *Debye-Hückel theory* describes the electric double layer around a sphere. With radial symmetry the Poisson-Boltzmann equation (1.15) in spherical coordinates becomes

$$\frac{1}{r^2} \frac{d}{dr} \left(r^2 \frac{d\Psi}{dr} \right) = -\frac{n_0 q_e}{\epsilon \epsilon_0} \cdot \left(e^{-\frac{q_e \Psi(r)}{k_B T}} - e^{\frac{q_e \Psi(r)}{k_B T}} \right) \quad (1.24)$$

This equation cannot be solved analytically. For small potentials one can expand the exponential functions in series and omit all but the linear terms. Then the equation is simplified to:

$$\frac{1}{r^2} \frac{d}{dr} \left(r^2 \frac{d\Psi}{dr} \right) = \kappa^2 \Psi \quad (1.25)$$

In order to solve this differential equation one must first substitute $\Psi \equiv u/r$. Respecting the boundary conditions $\Psi(r \rightarrow \infty) \rightarrow 0$ and $\Psi(r = R) = \Psi_0$ the differential equation can be solved:

$$\Psi = \Psi_0 \cdot \frac{R}{r} \cdot e^{-\kappa(r-R)} \quad (1.26)$$

The Debye-Hückel theory is applied in case of particles, whose radius is smaller than, or in the same order of magnitude of the Debye length. For large particles ($R \gg \lambda_D$), one can apply the Gouy-Chapman theory (planar surfaces).

1.2.3 Electrostatic Force – Derjaguin's Approximation

The approximated electrostatic force per unit area between two planar, semi-infinite surfaces separated by a distance h using the linearised Poisson-Boltzmann equation is [25]

- $f_{es}^{cp}(h) = 2\epsilon_0 \epsilon \kappa^2 \left[\Psi_1 \Psi_2 e^{-\kappa h} - \left(\Psi_1^2 + \Psi_2^2 \right) e^{-2\kappa h} \right] \quad (1.27a)$

in the case of both surfaces at constant potential, respectively Ψ_1 and Ψ_2 , and

- $f_{es}^{cc}(h) = \frac{2}{\epsilon_0 \epsilon} \left[\sigma_1 \sigma_2 e^{-\kappa h} + \left(\sigma_1^2 + \sigma_2^2 \right) e^{-2\kappa h} \right] \quad (1.27b)$

in the case of both surfaces with a constant charge density, respectively σ_1 and σ_2 .

A positive force is attractive, a negative one repulsive.

Experimental set-ups, on the other hand, measure forces between finite bodies with complicated geometries, e.g. spheres, cylinders and spheroids. For these systems exact analytical solutions are often inaccessible. To calculate the force between a flat sample and

a sphere, *Derjaguin's approximation* [26] can be used. Therefore the force per unit area f_{es} is integrated on a small circular cross-section of $2\pi r dr$:

$$F_{es}(h) = 2\pi \int_h^\infty f_{es} r \frac{dr}{dh} dh \quad (1.28)$$

According to Derjaguin's approximation the interaction of arbitrary bodies is calculated as a sum (integral) of the corresponding interaction forces per unit area of plane parallel half-spaces. The advantage of this method is that it enables us to describe the interactions between bodies of arbitrary form in terms of plate-plate interactions, provided that the distance between the bodies is smaller than the local radii of curvature.

Performing the integration leads to:

$$\bullet F_{es}^{cp}(h) = 4\epsilon_0 \epsilon \left[g_a \Psi_1 \Psi_2 e^{-\kappa h} - (g_b / 4) (\Psi_1^2 + \Psi_2^2) e^{-2\kappa h} \right] \quad (1.29a)$$

for the constant potential case, and to:

$$\bullet F_{es}^{cc}(h) = \frac{4}{\epsilon_0 \epsilon \kappa^2} \left[g_a \sigma_1 \sigma_2 e^{-\kappa h} + (g_b / 4) (\sigma_1^2 + \sigma_2^2) e^{-2\kappa h} \right] \quad (1.29b)$$

for the constant charge case, where g_a and g_b are geometrical factors. In the case of a sphere of radius R approaching an infinitely extended flat surface they correspond (approximated to the first term) to:

$$\begin{aligned} g_a &= \kappa R \\ g_b &= 2\kappa R \end{aligned}$$

1.3 Hydrodynamic Force

Any motion of a particle in a Newtonian fluid (the viscosity of the fluid does not depend on its shearing) can be described in terms of the *Navier-Stokes* equation

$$\eta \nabla^2 \vec{v} - \nabla P + F_b = \rho_f \left(\frac{\partial \vec{v}}{\partial t} + \vec{v} \cdot \nabla \vec{v} \right) \quad (1.30)$$

where v is the velocity of the fluid flow past the particle, ρ_f is the fluid density, P is the pressure, η is the dynamic viscosity of the fluid, $\vec{v} \cdot \nabla \vec{v}$ is the inertial, or quadratic, term, $\nabla^2 \vec{v}$ is the viscous term, F_b is the body volume force exerted on the particle and t is the time. The body force F_b arises when the particle is set in a fluid of a different density and a gravitational field is present. For a sphere it has the form:

$$F_b = \frac{4}{3} \pi R^3 (\rho_p - \rho_f) \vec{g} \quad (1.31)$$

where ρ_p is the density of the particle material and R is the radius of the particle.

For incompressible liquids the Navier-Stokes equation is complemented by the *continuity equation*

$$\nabla \cdot \vec{v} = \frac{\partial v_x}{\partial x} + \frac{\partial v_y}{\partial y} + \frac{\partial v_z}{\partial z} = 0 \quad (1.32)$$

To solve these equations for the fluid velocity v , the initial velocity field and the boundary conditions must be specified. The Navier-Stokes equation is a highly non-linear equation and complete analytical solutions exist only for simple geometries. In most cases it is necessary to apply numerical algorithms.

In most hydrodynamic processes the steady-state is established very fast and it is sufficient to consider the steady fluid motion. Then the time derivative $\partial v / \partial t$ can be neglected. The solution of the above equations is greatly simplified by the fact that the size of particles is of the order of micrometers. Thus the resulting Reynolds number $Re = \rho v R / \eta$ seldom exceeds 10^{-2} , R being the particle radius. Therefore, the Navier-Stokes equation can be linearised (the inertial term $\vec{v} \cdot \nabla \vec{v}$ is neglected with respect to the viscous one $\nabla^2 \vec{v}$) and as a result the *Stokes or creeping flow equation* is obtained [see 27]:

$$\eta \nabla^2 \vec{v} = \nabla P - F_b \quad (1.33)$$

Far from interfaces the mobility of a particle is isotropic, i.e. the total force and torque acting on a particle consist of external (e.g. gravity, buoyancy) or hydrodynamic forces due to the macroscopic fluid motion. In the simplest case of a spherical uncharged particle of radius R moving with the velocity v in an unbound fluid, the creeping flow equation reduces to the *Stokes formula* [27]

$$F_{hy} = -6\pi\eta Rv \quad (1.34)$$

The negative sign indicates that the hydrodynamic force is directed opposite to the velocity. In the vicinity of interfaces the hydrodynamic forces and torques are modified. At small distances from the interface, besides hydrodynamic and external forces, also specific surface interactions (e.g. electric, van der Waals, steric interactions) determine the rate of particle motion.

Hydrodynamic force in a gap upon vertical approach of a sphere [28]

We consider a symmetric system [see figure below], in which a sphere approaches perpendicularly a flat surface. The liquid is drained out from the closing gap between the surface and the lower part of the spherical body. We want to describe the hydrodynamic interaction in this specific case: The vertical component of the velocity (v_z) is zero, and

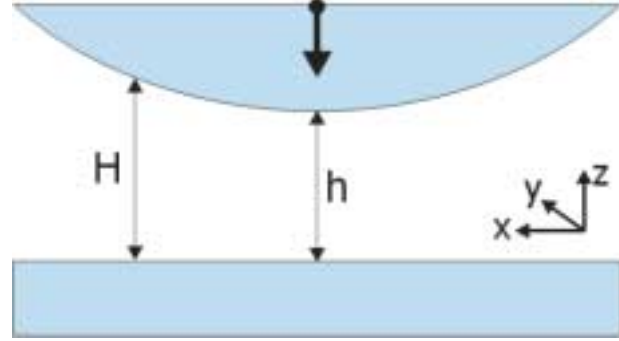
thus $v = v(x, y) = (v_x, v_y)$ and $P = P(x, y)$. The body volume force F_b is neglected and set to zero, and h is considered always much smaller than the radius R of the sphere.

Therefore the *creeping flow equation*

$$\eta \nabla^2 \vec{v} = \nabla P,$$

or extensively

$$\eta \begin{pmatrix} \frac{\partial^2 v_x}{\partial x^2} + \frac{\partial^2 v_x}{\partial y^2} + \frac{\partial^2 v_x}{\partial z^2} \\ \frac{\partial^2 v_y}{\partial x^2} + \frac{\partial^2 v_y}{\partial y^2} + \frac{\partial^2 v_y}{\partial z^2} \\ \frac{\partial^2 v_z}{\partial x^2} + \frac{\partial^2 v_z}{\partial y^2} + \frac{\partial^2 v_z}{\partial z^2} \end{pmatrix} = \begin{pmatrix} \frac{\partial P}{\partial x} \\ \frac{\partial P}{\partial y} \\ \frac{\partial P}{\partial z} \end{pmatrix},$$



Geometry of the sphere-wall interaction

becomes

$$\begin{aligned} \eta \frac{\partial^2 v_x}{\partial z^2} &= \frac{\partial P}{\partial x} \\ \eta \frac{\partial^2 v_y}{\partial z^2} &= \frac{\partial P}{\partial y} \end{aligned} \tag{1.35}$$

The problem has radial symmetry, so the solution of one equation applies also to the other.

Integration of the first equation in z leads to:

$$\eta \frac{\partial v_x}{\partial z} + C_1 = z \frac{\partial P}{\partial x} \tag{1.36}$$

because $\partial P / \partial x$ does not depend on z . Second integration leads to:

$$\eta v_x + z C_1 + C_2 = \frac{z^2}{2} \frac{\partial P}{\partial x} \tag{1.37}$$

The no-slip boundary condition

If the *no-slip boundary condition* is assumed (liquid layer in contact with the surface has the same velocity of the surface, i.e. zero):

$$\begin{aligned} v_x = 0 \text{ for } z = 0 & \Rightarrow \eta v_x + C_2 = 0 \Rightarrow C_2 = 0 \\ v_x = 0 \text{ for } z = H(x, y) & \Rightarrow \eta v_x + H C_1 = \frac{H^2}{2} \frac{\partial P}{\partial x} \Rightarrow \frac{H^2}{2} \frac{\partial P}{\partial x} = H C_1 \\ & \Rightarrow C_1 = \frac{H}{2} \frac{\partial P}{\partial x} \end{aligned}$$

Substituting these values in the equation yields:

$$\eta v_x + z \frac{H}{2} \frac{\partial P}{\partial x} = \frac{z^2}{2} \frac{\partial P}{\partial x} \quad \Rightarrow \quad v_x = \frac{z}{2\eta} \frac{\partial P}{\partial x} (z - H) \quad (1.38a)$$

The same is valid also in y-direction:

$$v_y = \frac{z}{2\eta} \frac{\partial P}{\partial y} (z - H) \quad (1.38b)$$

Considering the *continuity equation* (1.32) and developing further the calculus [see 27, 28] we get the expression for the hydrodynamic force acting on a spherical, uncharged particle moving perpendicularly towards a flat, uncharged surface

$$F_{hy} = -\frac{6\pi\eta R^2}{h} \cdot \frac{dh}{dt} \quad (1.39)$$

The negative sign indicates that the hydrodynamic force is directed opposite to the velocity

The slip boundary condition

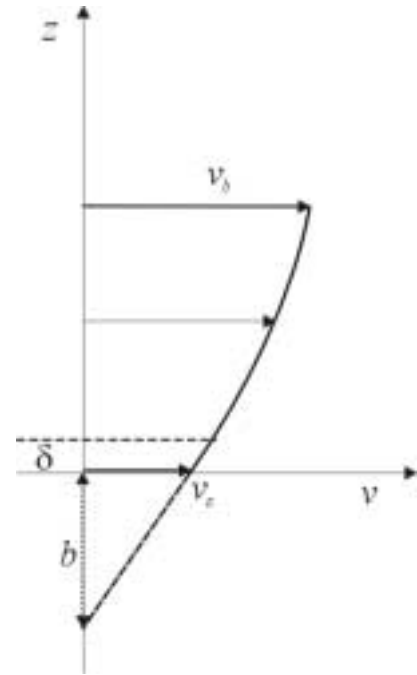
If the *slip boundary condition* is assumed, the equations are solved in a similar way, but in the result is introduced a correction factor f^* [29]:

$$F_{hy} = -\frac{6\pi\eta R^2}{h} \cdot \frac{dh}{dt} \cdot f^* \quad (1.40a)$$

with

$$f^* = \frac{h}{3b} \cdot \left[\left(1 + \frac{h}{6b} \right) \cdot \ln \left(1 + \frac{6b}{h} \right) - 1 \right] \quad (1.40b)$$

b is the so-called *slip length*, i.e. the distance behind the interface at which the liquid velocity extrapolates to zero [30]. In the figure nearby, v_b is the velocity of the bulk liquid and v_s is the velocity of the liquid in contact with the surface. We remark that f^* depends on the ratio of gap to slip lengths h/b , and is always less than or equal to unity. This means that the role of slip



Representation of the slip length

is revealed by the decrease in drag force as compared to the case where no slip occurs. This also means that at large distances compared with b , i.e. distances larger than the slip lengths of the solids, the liquid flow is the same as that described by eq. (1.39).

Alternatively, described in terms of a reduced viscosity, the slip length can be written as:

$$b = \delta \left(\frac{\eta_b}{\eta_s} - 1 \right) \quad (1.41)$$

with η_b viscosity of the liquid in the bulk and η_s viscosity of the liquid in the region of thickness δ , close to the interface.

1.4 Electrokinetic Force

Electrokinetic effects are the result of the interplay between a charged interface and the flow field around it. Theoretical and experimental research on the electrokinetic effects like electrophoresis, electroosmosis, streaming and sedimentation potential, has been extensively carried out, and the summary of the results can be found in several monographs [16, 31, 32]. However, the influence of the electrokinetic effects on the motion of a single particle in the vicinity of an interface has been considered first in recent years [33, 34].

The general framework of electrokinetic phenomena in colloidal systems is provided by the Stokes equation including an additional electrostatic force term:

$$\eta \nabla^2 \vec{v} = \nabla P + \rho_e \nabla \Psi \quad (1.42)$$

together with the continuity equation $\nabla \cdot \vec{v} = 0$. The distribution of the electric potential is governed by the Poisson equation (1.11)

$$\nabla^2 \Psi = -\frac{\rho_e}{\epsilon \epsilon_0}$$

while the distribution of ionic charges is determined by the so called "*ionic convective diffusion equation*". The solution of this set of equations is a formidable task even in the simplest geometry due to the presence of non-linear coupling terms, such as $\rho_e \nabla \Psi$.

A series of simplifying assumptions can be made in order to solve these equations:

- Small potentials ($\Psi \ll 1$)
- 1-1 symmetric electrolyte
- "*Thin double layer*" approximation [32], assuming $R_{particle} \gg 1/\kappa$. This allows to solve the problem in a locally flat geometry, and then to extend the result.

The electric potential in the vicinity of a moving particle can be expressed by a sum of three terms

$$\Psi = \Psi_{eq} + \Psi_d + \Psi_s \quad (1.43)$$

in extension to the findings in the static case, eq. (1.2). Ψ_{eq} is the potential at the static double layer, Ψ_d the distortion of the double layer from the equilibrium due to particle

motion and Ψ_s is the long range "streaming" potential outside the double layer. The origin of these effects is illustrated in Figure 1, where j represents the ionic flux.

In a first approximation the fluid flow can be separated in a *hydrodynamic* and in an *electroosmotic flow*, with $v = v_h + v_e$. The electroosmotic flow arises because of the formation of the electric field E , and vanishes for uncharged particles.

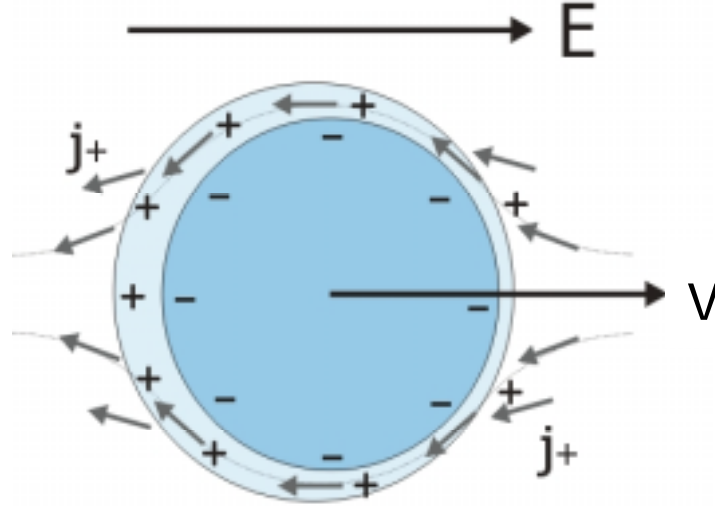


Figure 1: Schematic representation of the distorted electric double layer (EDL) and ionic fluxes j around a negatively charged spherical particle moving with a constant velocity v in a polar liquid. Due to the cationic flux on the surface of the particle and their enrichment behind the particle, an electric field E in direction of the movement arises.

The Navier-Stokes equation must be fulfilled for each flow separately

$$\begin{aligned} \eta \nabla^2 \vec{v}_h &= \nabla P_h \\ \eta \nabla^2 \vec{v}_e &= \nabla P_e + \rho \nabla \Psi \end{aligned} \quad (1.44)$$

Thus, the motion of a charged particle creates an additional electroosmotic flow field, which in turn exerts some force on the particle. This force can be calculated solving the system of the equations (1.44). Under some particular conditions, this force is a linear function of the particle velocity, but more generally it depends on higher powers of the particle velocity.

The situation turns out to be more complex when a charged particle approaches a flat charged surface [Figure 2]. This has been partially solved [35] in the thin double layer approximation, yet no analytical solution has been found so far. One fact is that charged particles are retarded up to two times stronger than uncharged ones when approaching a solid interface. The already mentioned electroosmotic flow slows down the velocity of the particle, but the most considerable delay of the microsphere is a consequence of the repulsion of the electric double layers on the surface and on the particle.

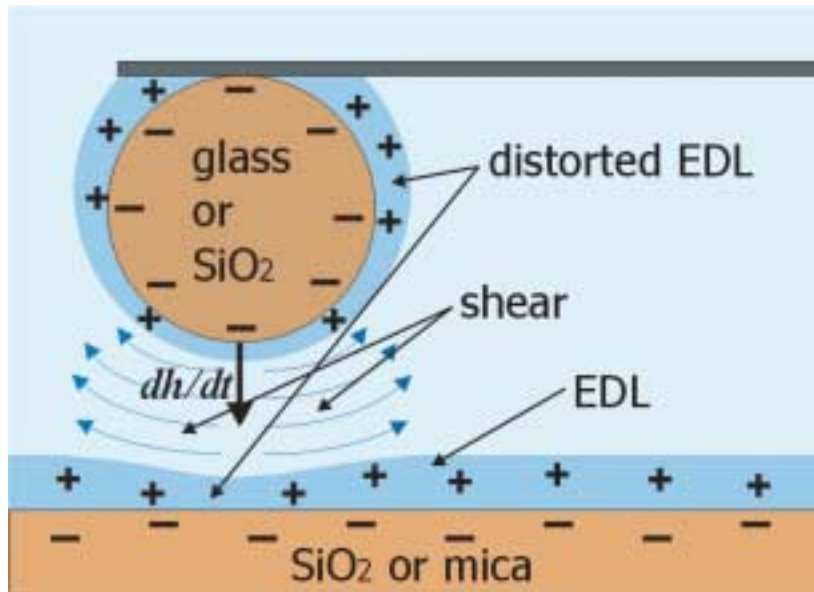


Figure 2: Charged particle approaching a charged solid interface: The shear and the distorted EDL of both the sphere and the surface are visualised.

1.5 AFM and SFA

Interaction forces between small particles and between solid surfaces can be detected by several means. In direct methods two solids are brought close together and the force between them is measured as function of the distance. A good review on this topic is [36]. The conditions for proper measurement of surface forces is a small roughness because it limits the distance resolution, and a dust-free, clean surface.

The most relevant devices in this field are the surface force apparatus [37, 38, 39], the atomic force microscope [40] and the particle interaction apparatus [41].

1.5.1 Surface Force Apparatus

With the *SFA technique* [Figure 3] two curved and atomically smooth mica surfaces immersed in a liquid can be moved towards each other in a highly controlled way (crossed cylinder geometry): The vertical resolution is in the order of 0.1 nm, the force resolution is in the order of 10 nN. As the surfaces approach each other, a very thin film of liquid gets trapped between them and the forces between the two surfaces (across the liquid film) are monitored. Although this technique has been successfully applied to the detailed study of surface interactions, it is limited by the requirements that the substrates have to be composed by semitransparent, flexible, and molecularly smooth, thin (some μm) sheets (mica).

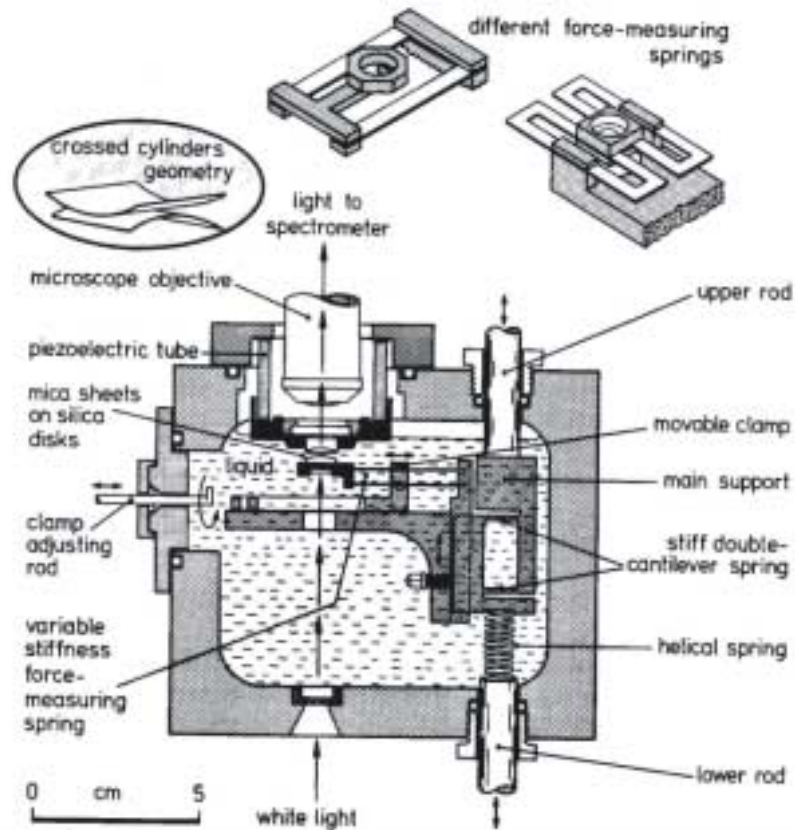


Figure 3: Surface force apparatus (SFA) for directly measuring the force laws between surfaces in liquids or vapours at the ångstrom resolution level. Picture from [15].

1.5.2 Atomic Force Microscope

With the *AFM technique* [Figure 4] the force between a sample surface and a microfabricated tip, placed at the end of an about $100 \div 200 \mu\text{m}$ long and $0.4 \div 1.5 \mu\text{m}$ thick cantilever is measured. Usually, the tip has pyramidal shape. To measure the force between a colloidal particle and a substrate surface in air and in liquid, the particle is attached to a cantilever [see Figure 5] and approaches the substrate surface from above [42, 43, 44, 45].

In an *AFM*, a piezoelectric scanner moves the sample vertically and laterally. Disabling the lateral movement used for imaging and for lateral force microscopy (in *LFM* mode the signal monitored is the torsion of the cantilever caused by friction between tip and sample surface), it is possible to measure force vs. distance curves: The sample is moved up and down while recording the deflection of the cantilever. Multiplying the deflection with the spring constant of the cantilever gives the force.

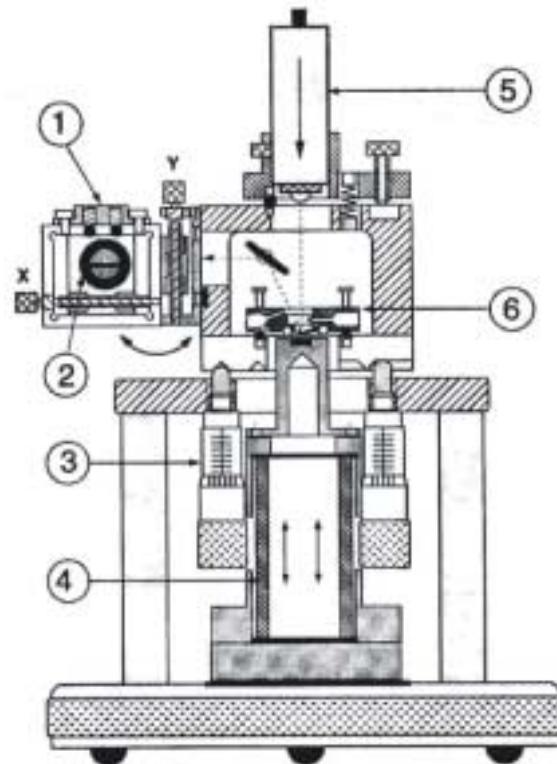


Figure 4: Modified AFM, or LLIFE (light-lever instrument for force evaluation [46]), indicating (1) miniature x-y translation stage for positioning the photo detector, (2) split photodiode for detecting the cantilever deflection, (3) micrometer screw for a rough positioning of the sample under the cantilever, (4) piezoelectric tube for scanning the sample up and down, (5) laser diode, (6) cantilever mounted in a fluid cell.

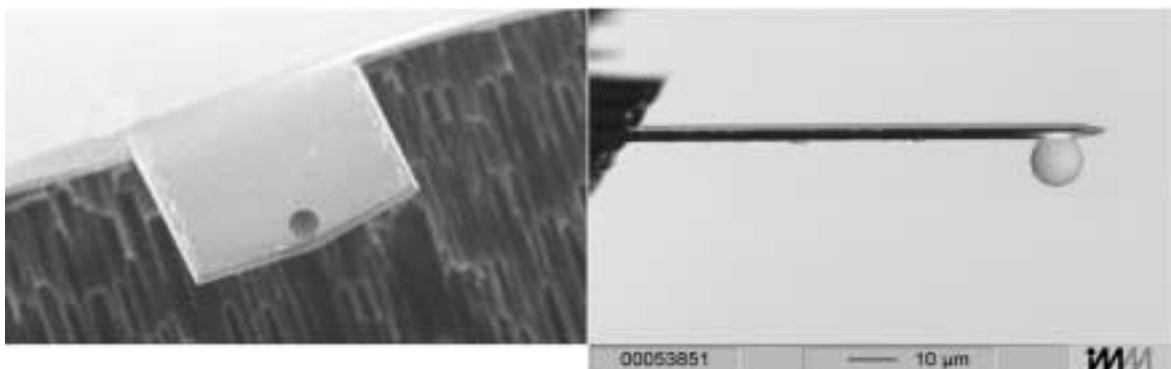


Figure 5: Colloidal particle fixed at the end of a rectangular (diving board) cantilever. The left image shows a "small" microsphere (radius of 2.5 μm), the right image shows a sphere with a radius of 5 μm .

1.5.3 AFM vs. SFA

Although there is a considerable overlap in the force measuring capabilities of the AFM and the SFA, it is useful to point out several differences:

1. The SFA only employs surfaces of known geometry, thus leading to precise measurements of surface forces and energies
2. Interacting surfaces in AFM are $10^4 \div 10^6$ times smaller than those employed in SFA, but in AFM the shape of the surfaces is unknown
3. The SFA measures the force curves with an interferometric technique, thus the substrate under research has to be optically transparent. [47]
4. The SFA needs molecularly smooth samples, and therefore it works best only with mica surfaces or thin layers of materials adsorbed on mica
5. The SFA cannot characterise indentation or topography
6. The viscous force on a spherical particle scales with the square of the particle radius. Therefore, AFM measurements can be performed at speeds 10^4 times higher while maintaining the same ratio of viscous force to surface force [48]
7. Since the interacting surfaces are smaller, and the probability of trapping a contaminant particle is proportional to the square root of the interacting surfaces, the AFM is less subject to contamination [48]

2 Materials and Methods

2.1 Particle Interaction Apparatus (PIA)

In the progress of this work I performed interparticle force measurements with an apparatus that is closely related to the AFM, the *particle interaction apparatus* (PIA), which we constructed in our lab [41]. PIA is equipped with a piezoelectric translator for horizontal movement and one for vertical movement [Figure 6]. Instead of being able to image the sample, major improvements with respect to measuring frictional and normal forces have been made:

- Both piezo translators are equipped with internal capacitance distance sensors. Thus the absolute piezo position can be controlled with Ångstrom resolution. No independent calibration is required. One piezo moves the sample vertically to record normal force curves. The other moves the sample horizontally, in a direction perpendicular to the length axis of the cantilever to measure shear and friction forces.
- In place of a standard photodiode, a two-dimensional position sensitive device (PSD) is used to monitor the position of the reflected laser beam. The output current of the detector is directly proportional to the position of the centre of the light spot.
- The measuring cell is easily accessible, easy to clean (it is made of Teflon or PEEK and glass), and the particles can be observed from different directions (one or more sides of the liquid cell are transparent) with help of a CCD camera mounted on a microscope objective. Images and videos can be acquired with a frame grabber card.
- The position of the piezo translators is controlled via a personal computer. Additionally, the deflection signals are amplified and recorded via an A/D board. Therefore, it is not only possible to measure force curves with a constant approaching speed, but arbitrary position vs. time curves can be programmed. Normal force curves can be combined with lateral forces, for instance to study normal forces of sheared liquids.

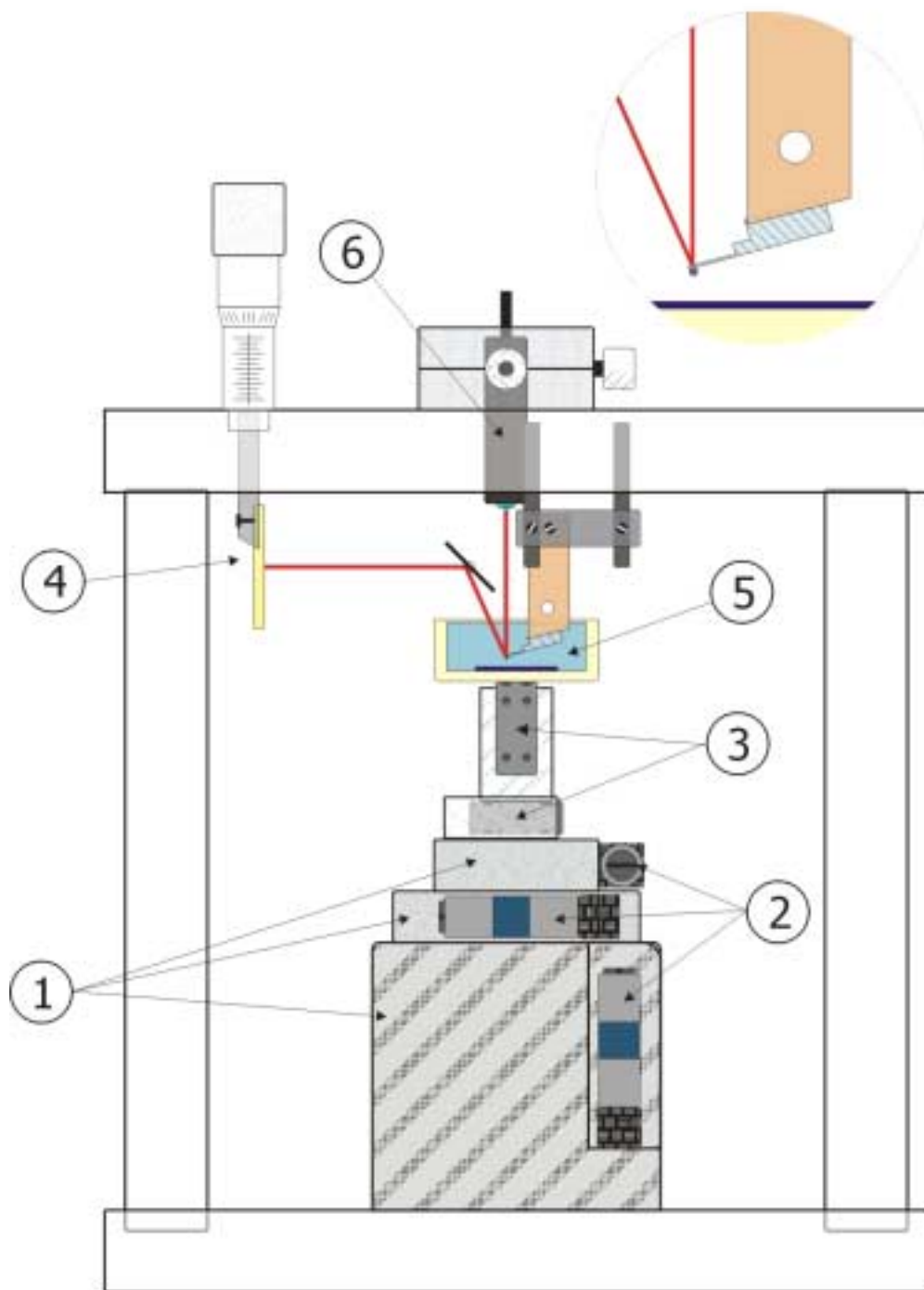


Figure 6: PIA (particle interaction apparatus), indicating (1) x - y - z translation stage, (2) stepper motors for controlling the x - y - z stage, (3) piezos for horizontal and vertical displacement, (4) PSD for monitoring the cantilever deflection, (5) liquid cell with substrate on the bottom, cantilever with particle fixed on a holder from above, (6) a 5 W and 670 nm laser light source, movable in x - y direction for focusing on the backside of the cantilever end.

Components of PIA

The position of the sample is controlled with two piezoelectric translators (Physik Instrumente GmbH, Waldbronn, Germany) for horizontal and vertical displacement. The

latter is mounted on the other piezoelectric translator which is used for lateral movements of the sample, perpendicular to the cantilever's length axis. Both piezos have a maximum range of 12 μm and a *rms*-noise of 0.1 nm. They are equipped with internal capacitance distance sensors which measure the absolute displacement. An electronic controller for each piezo monitors the signal of the capacitance distance sensor and regulates the voltage supplied to the piezo to control the position. Thus, hysteresis and creep of the piezos are avoided.

The chip with the cantilever is clamped to a holder above the sample stage. Light from a laser diode is coupled into an optical fiber and focused on the backside of the cantilever, using a micro focusing optic to obtain a circular spot of 8 μm in diameter. A two-dimensional PSD is used to monitor the movements of the reflected laser beam. It provides two output currents which are converted to the voltages U_v and U_h . These two voltages are proportional to the position of the laser spot with respect to the vertical and horizontal direction. Both voltages range from -10 V to +10 V. The PSD has an active area of $20 \times 20 \text{ mm}^2$, in order to have a large dynamic range.

For rough adjustment of the particle-sample distance a *x-y-z* stage driven by three stepper motors (Faulhaber GmbH, Schönaich, Germany) is used. The translation range of the three stages is 25 mm.

PIA is fully operated by a personal computer. The software controls the stepper motors for coarse approach, generates the driving signal for the vertical and lateral piezo translators and reads the cantilever's vertical and lateral deflection signals from the PSD, plus it can acquire an additional (auxiliary) signal. The software, developed in LabView (National Instruments Corp., Austin, USA), consists of a real-time panel to operate the instrument and procedures to handle and analyze data off-line. D/A and A/D conversions are operated by a PCI-6052E board (National Instruments Corp.) with 16-bit resolution for both input and output. The vertical and the lateral piezo translators can both be moved independently following user-defined waveforms. This allows either to record vertical force curves while keeping the lateral position fixed at an arbitrary value, or to record lateral force curves while keeping the cantilever at a constant vertical position, or to move both stages at the same time at different speeds. The maximum speed of the driving signal is hardware limited and depends on the output resolution. With 16-bit output resolution, which corresponds to a digitization error of 0.18 nm for a 12 μm movement, the maximum scanning rate is 2.5 Hz. When lowering the resolution to 12 bit is it possible to take force curves with up to 40.3 Hz. The off-line software allows to manipulate the acquired data,

calculate force vs. distance curves and perform basic analysis like fitting pre-contact and post-contact regions, extracting pull-off force, jump-into-contact distance etc.

Experiments can be performed in liquid or in air.

2.2 Cantilevers and Spheres

Tip less **cantilevers** (various shapes and dimensions [see Figure 7]) were designed and fabricated at the Institute for Microtechnology Mainz (IMM GmbH, Mainz, Germany) as described in chapter 3. Two different materials are used for the cantilevers: Silicon dioxide and poly-crystalline silicon. The advantage of the second is that there is no need of a gold coating on the back side of the cantilevers for reflecting the laser beam, thus preventing effects like bending upon temperature variation due to bimetallic effect.

Spherical borosilicate glass particles (Duke Scientific Corporation, Palo Alto, USA) are attached to the tip less cantilevers and used as probes. Typical radii of the microsphere used in this work are 5, 8 and 10 μm .

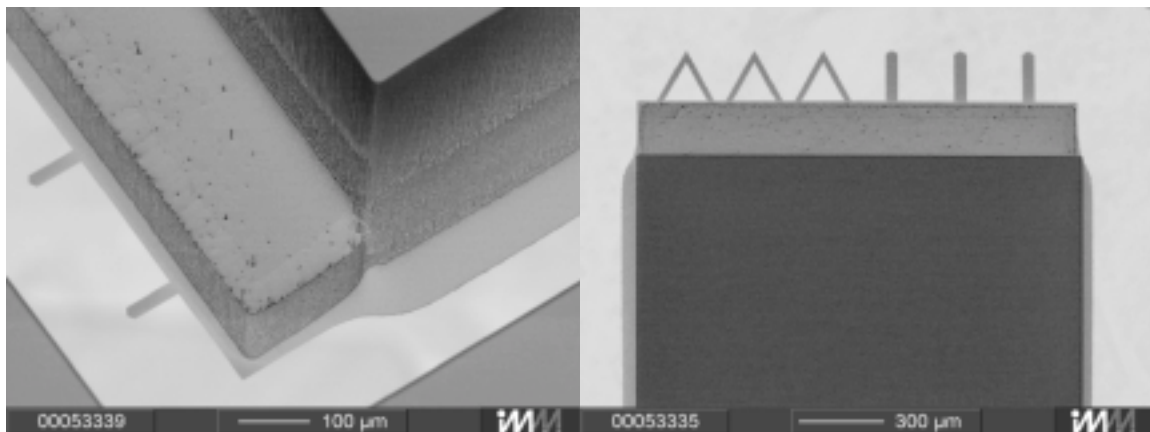


Figure 7: SEM (scanning electron microscopy) micrographs of microfabricated cantilevers. The left image shows rectangular cantilevers, having a triangular cap at the end. The right image is a top view of one end of a chip showing three triangular and three rectangular cantilevers made of SiO_2 .

2.3 Chemicals

Muscovite (white) **mica** (Plano GmbH, Wetzlar) and **silicon** (5" silicon wafer, DSP, 624 μm) are used as standard sample materials for the measurements. A clean mica surface is prepared by cleaving some layers of material with an adhesive tape. The silicon sample has a native oxide layer of about 3 nm thickness and its surface roughness is below 1 nm *rms*.

The silicon sample is plasma cleaned (PlasmaPrep₂, GaLa Instrumente, Germany) before each measurement. Standard dimensions of the sample surfaces are $20 \times 20 \text{ mm}^2$.

Solutions and chemicals: De-ionised water (Barnstead E-Pure, resistivity = $18.2 \cdot 10^6 \text{ } \Omega\text{cm}$) are used for cleaning, rinsing and for preparing aqueous solutions. Acetone and ethanol p.A. are used for cleaning and conservation of the probes. Fluka chemicals (MicroSelect, AT $\geq 99.5\%$) are used for experiments (NaCl, KCl, KOH, NaOH, KI).

2.4 Probe Preparation and Cleaning

Colloidal particles (microspheres) are attached to tip less silicon dioxide and poly-silicon cantilevers with help of a transmission light microscope [see Figure 8].

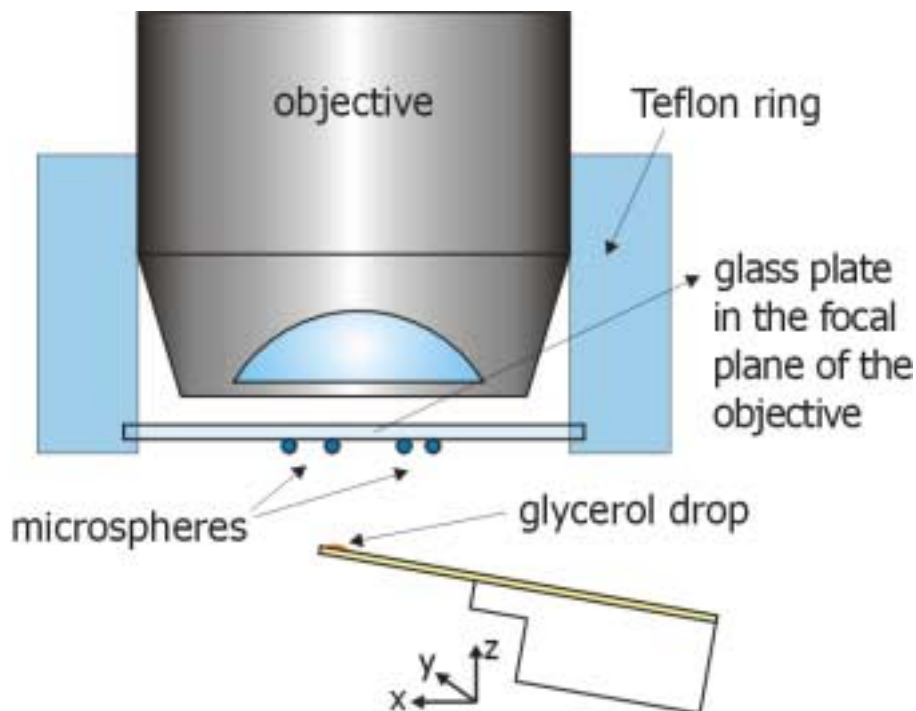


Figure 8: Schematics of the device used for attaching colloidal particles to a cantilever. The microspheres hang on a glass slide and are in the focal plane of the microscope objective. The cantilever (whose chip is fixed on the arm of a 3-D micromanipulator) approaches a microsphere from below, picks it up, and is then put into an oven for the sintering process.

A home-made Teflon ring which can be fixed around the objective of the microscope is used to lodge a circular glass platelet on the bottom. The glass sheet must be placed in the focal plane of the objective, so that the microspheres can be viewed through the microscope. The particles are poured on the glass: This can be done either by just pouring them onto the surface with a spatula and distributing them evenly by passing over them

with some fine filter paper, or by making a colloidal suspension of particles (in ethanol or water) and then pipetting a drop of this suspension on the surface (evaporation of the solvent leaves the particles behind). The microspheres adhere on the glass even if this is put upside down, due to capillary force.

The chip with the cantilever is fixed on a micromanipulator arm (three dimensional oil-hydraulic manipulator MMO–203, Narishige Group, Japan), which allows to approach single particles with high precision. Instead of gluing a particle to the cantilever with an epoxy resin as described in the literature [49, 50] we developed a sintering method to attach the particles in order to get rid of possible contaminations of the electrolyte solution in contact with the glue. I used spheres made of borosilicate glass, a material which has a much lower melting temperature (1250 °C) than silica (1700 °C). The cantilever is first dipped into a glycerol drop, then a particle is picked up from the glass plate. The glycerol serves to keep the particle fixed during the withdrawal of the cantilever from the glass sheet. The cantilevers with the attached particles are then put into an oven (Furnace 47900, Thermolyne, USA) and heated up to 780 °C (little below the softening point of 820 °C of the borosilicate glass) for two hours. All glycerol evaporates in this process, and finally a connection of the particle and the cantilever could be established [see Figure 9].

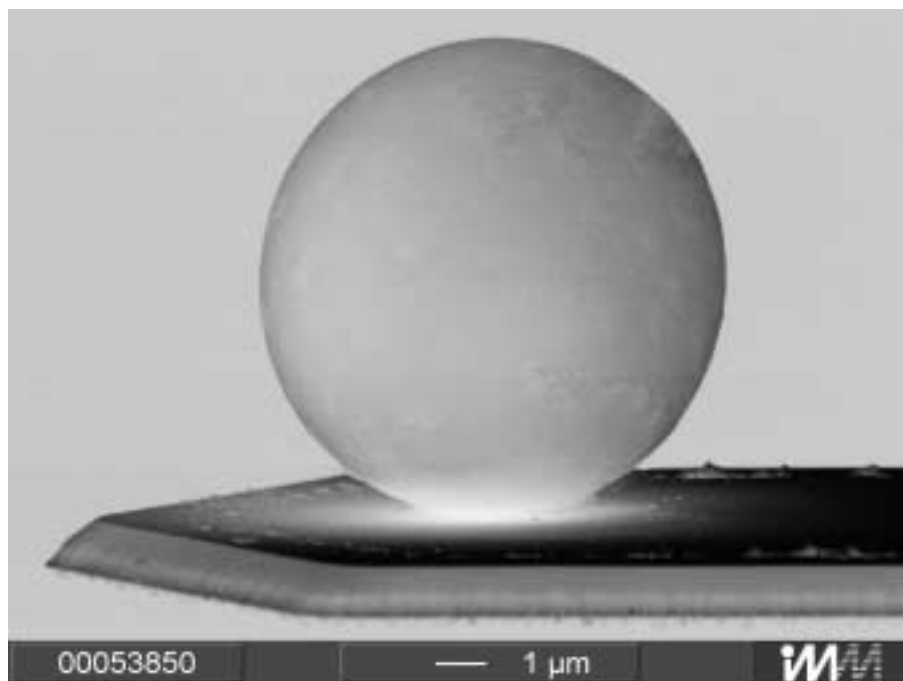


Figure 9: SEM micrograph of a colloidal particle (radius ~ 5 μm) sintered on the free end of a rectangular SiO₂ cantilever.

These probes are stored in de-ionised water or ethanol for preventing contamination, and are plasma cleaned before each measurement.

2.5 Cantilever Calibration

The spring constant calibration of the cantilever is a critical process. First of all, the exact value of the spring constant enters all force calculations. Secondly, all present experimental methods for the calibration of the spring constant suffer from uncertainties in the order of 10 to 20 per cent of the measured value. Third, it is known that cantilever spring constants vary in the course of days or weeks, due to the modification of material properties depending on environmental parameters. For these reasons the calibration procedure should be easy to implement and give a fast response. Several spring calibration methods are known in literature and commonly adopted: The thermal method [51], the added mass method [52, 53], the Sader method [54] and the reference spring method [55, 56].

The spring constant of an end-loaded cantilever of rectangular cross section is

$$k = \frac{Ea^3w}{4l^3} \quad (2.1)$$

where E is the elastic modulus of the component material, a is the cantilever thickness, w its width and l its length. Width and length can be determined with an error of less than 1%, whereas E and a can only be determined with an accuracy of around 10 ÷ 15 per cent. Thus, the obtained value is just a guideline for the order of magnitude of the spring constant.

2.5.1 Added mass method

The cantilever beam can be approximated as a spring of stiffness k with an effective mass m_{CL}^* at its end dependent on the beam geometry [see Figure 10]. For a uniform cantilever of rectangular cross section this effective mass is $m_{CL}^* = 0.24m_b$ where m_b is the mass of the beam given by the product of its length, width and thickness times its material density.

When an end mass m_{end} is added, the spring constant k of the cantilever does not change, while the resonant frequency is given by

$$\nu_0 = \frac{1}{2\pi} \sqrt{\frac{k}{m_{end} + m_{CL}^*}} \quad (2.2)$$

This equation can be rearranged to give

$$m_{end} = k(2\pi\nu)^{-2} - m_{CL}^* \quad (2.3)$$

which shows that if several known end masses are added to a cantilever and the new resonance frequencies are measured, a linear plot of added masses versus $(2\pi\nu)^{-2}$ should

give a straight line, the slope being the spring constant and the negative y-intercept the effective mass m_{CL}^* . This method allows the determination of spring constants of arbitrarily shaped cantilevers. However, due to the necessity for the attachment of spheres of different masses to the end of the cantilever, the method suffers from some practical difficulties which limit its accuracy: During the whole process (attachment of one particle, measurement of the resonance frequency, removal of that particle, attachment of another one, etc.) the risk of breaking or damaging the cantilever is high. Further, one needs to know very accurately the weight of the attached masses. Also, an error in misplacing the masses always at the same spot on the cantilever may result in a significant error in finding the correct value for the spring constant [57].

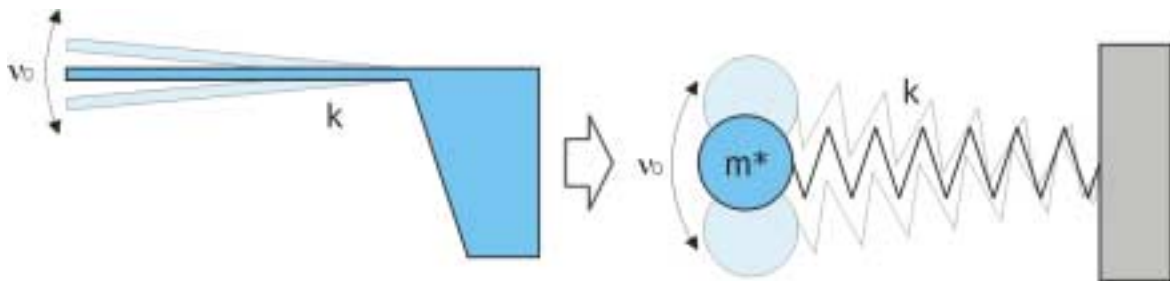
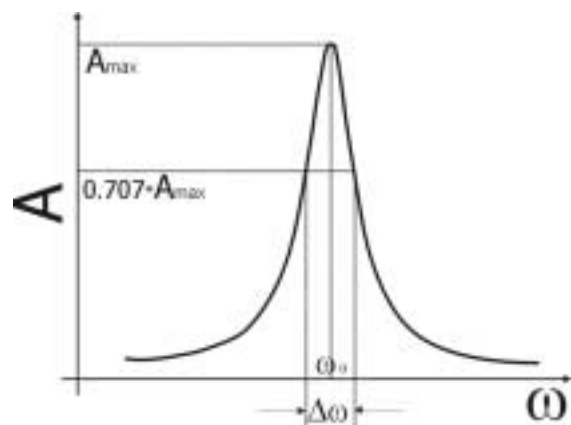


Figure 10: Real cantilever and theoretical model for determination of the spring constant k , with m^* the effective mass and ν_0 the resonance frequency of the cantilever.

2.5.2 Sader method

The Sader method is less time consuming and easier to implement. It relies solely on the measurement of the resonant frequency ν_0 , the quality factor Q_f of the cantilever and on the knowledge of its planar view dimensions (w and l). It can, however, be applied only to rectangular cantilevers. The quality factor Q_f is defined as $\omega_0 / \Delta\omega$, with ω_0 the radial resonance frequency ($\omega_0 = 2\pi\nu_0$) and $\Delta\omega$ the full bandwidth at $\sqrt{2}/2 = 0.707$ of the maximum amplitude of the spectrum A_{max} .

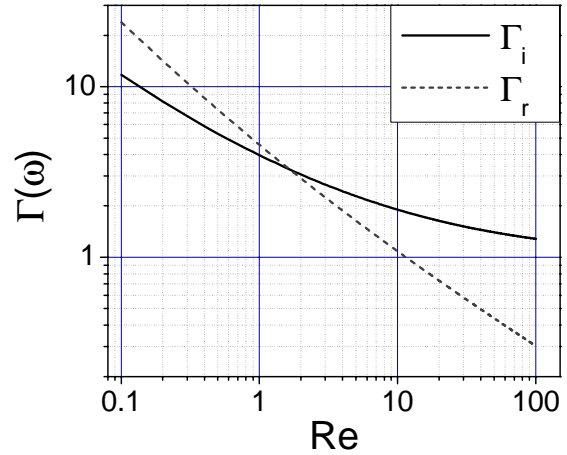


Quality factor Q_f , derived from the resonance spectrum of the cantilever.

The equation of the spring constant becomes [54]:

$$k = 0.1906 \rho_f w^2 l Q_f \Gamma_i(\omega_0) \omega_0^2 \quad (2.4)$$

ρ_f is the density of the fluid (air in my case). Γ_i is the imaginary component of the hydrodynamic function $\Gamma(\text{Re}(\omega_0))$ [see 58 and Figure nearby], which is a function of ω_0 and, according to $\text{Re} = \rho_f \omega_0 w^2 / 4\eta$, of the Reynolds number Re (η is the viscosity of the fluid surrounding the cantilever, which in my case is air again). Because of the obvious advantages and the simplicity of this method, I specifically designed and fabricated rectangular cantilevers. Two identical beams are placed on the same edge of the chip at a fixed distance from each other [see Figure 11].



Plot of the real and imaginary components of the hydrodynamic function $\Gamma(\omega)$ as a function of the Reynolds number.

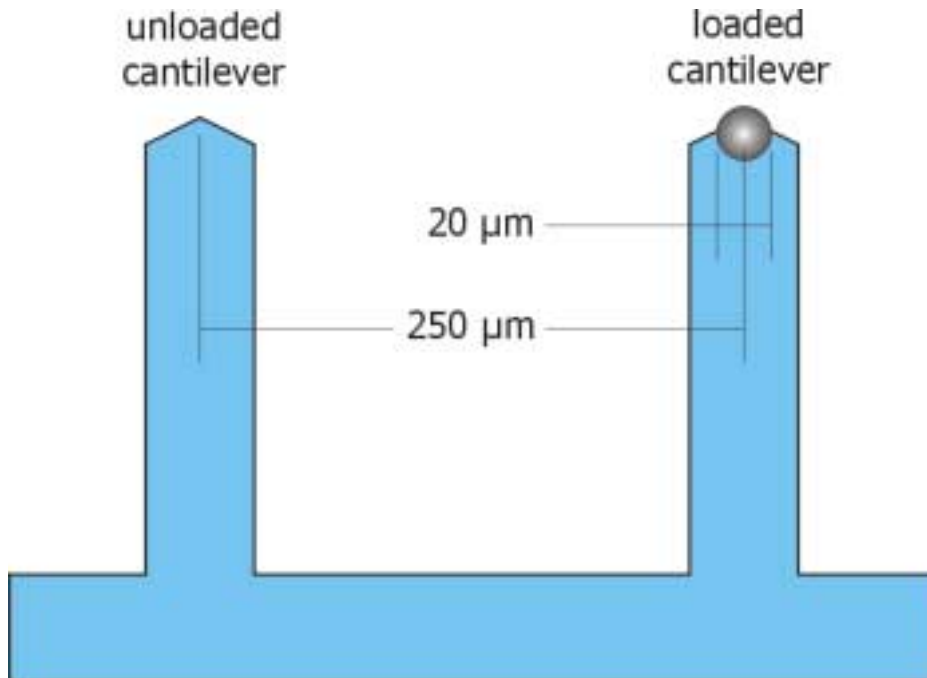


Figure 11: Pair of cantilevers used for the Sader calibration method. Cantilever lengths are: $l = 90, 140, 180, 210 \mu\text{m}$, and the width w is equal to $l/4$ for each cantilever. The triangular shape at the end of the cantilever does not alter significantly the value of the resonance frequency, while it is useful for a correct placement of the microsphere at the end of the length axis of the cantilever.

I can safely assume that the material properties as the spring constants of the two beams are the same, since they stay very close (inter-distance of 250 μm), and that the presence of the particle on one cantilever does not alter its spring constant.

Adopting this technique allows me to **calibrate the spring constant** of the cantilever with the attached particle **before every measurement**, by simply determining the resonant frequency of the blank cantilever nearby. This, in turn, results in a higher degree of precision when determining the actual forces that act on the probe.

In Figure 12 are shown three consecutive experimental power spectra of the same rectangular poly-silicon cantilever ($w = 52.5 \mu\text{m}$, $l = 210 \mu\text{m}$) and a lorentzian fit of one of the three curves. The fit provides all the necessary parameters for the application of eq. (2.4): $\omega_0 = 82575 \text{ 1/sec}$, $Q_f = 7.31$ and $\Gamma_i(\omega_0) = 2.002$. The calculated spring constant in this case is $k = 0.0128 \text{ N/m}$.

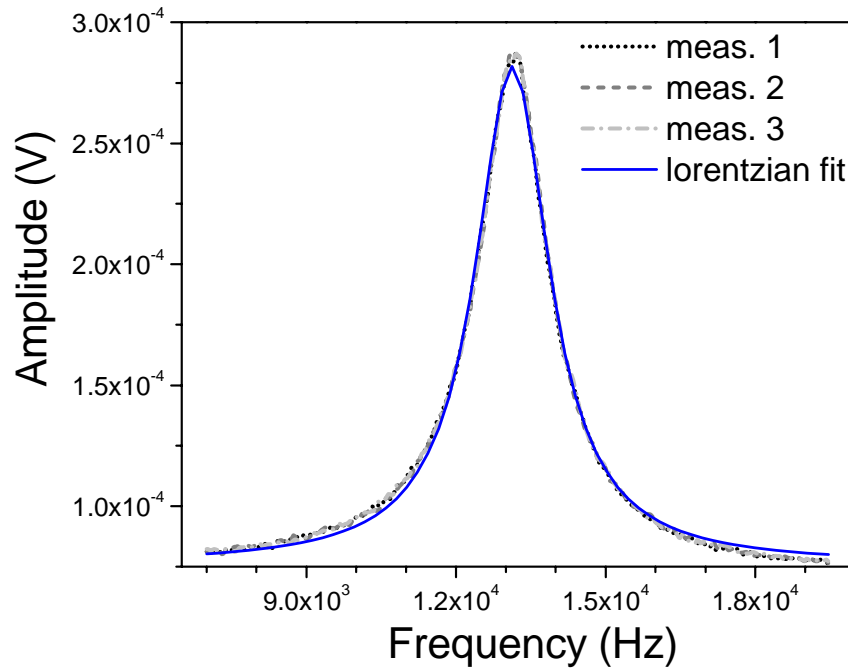


Figure 12: Three experimental resonance spectra of the same bare, rectangular cantilever, and lorentzian fit of one of the curves. From this fit, the radial resonance frequency ω_0 and the quality factor Q_f are derived.

2.5.3 Reference spring method

This method is based on the deflection of a cantilever, when pushed against another one with known spring constant. Two measurements are required: First, the cantilever under test is placed into contact with a fixed substrate (assumed to be infinitely hard relative to the cantilever compliance) and the cantilever deflection, δ_{tot} , is measured as the substrate is pushed vertically against the cantilever. Afterwards, this cantilever is placed into contact

with the free end of a reference cantilever and the deflection of the one under test, δ_{test} , is measured as the base of the reference cantilever pushes vertically against it by the amount δ_{tot} [see Figure 13].

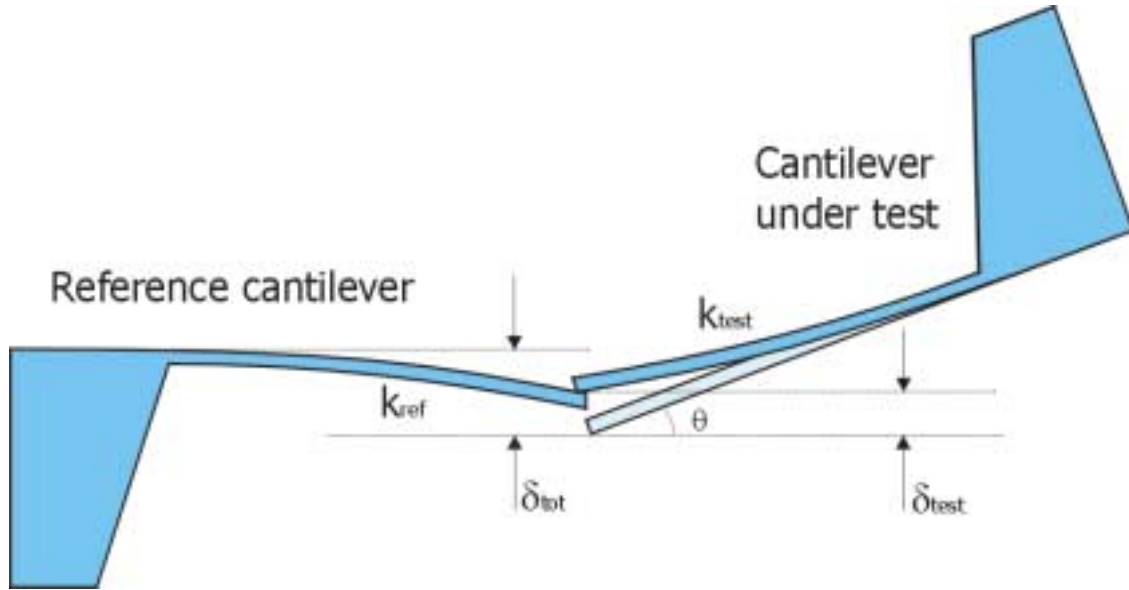


Figure 13: Reference spring method: A cantilever of unknown spring constant k_{test} is pushed against another cantilever of known spring constant k_{ref} . The angle θ between the cantilevers and the measured deflections δ_{tot} and δ_{test} allow to calculate the unknown spring constant.

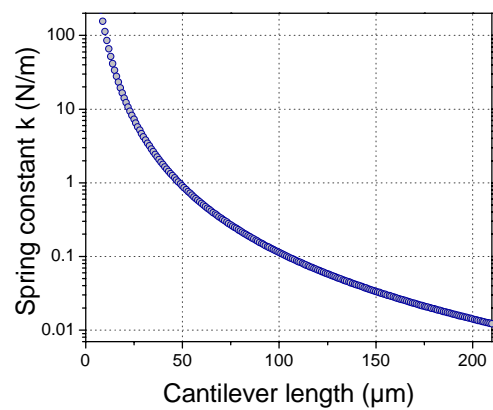
If the spring constant of the reference cantilever is k_{ref} , then the spring constant of the cantilever under test can be calculated [see 56] as:

$$k_{test} = k_{ref} \frac{\delta_{tot} - \delta_{test}}{\delta_{test} \cos \theta} \quad (2.5)$$

where θ is the angle between the test and the reference cantilever, and is measured from the side with a microscope. The method gives most precise results when $k_{test} \approx k_{ref}$.

When acquiring the force curves with a standard force vs. distance software, δ_{tot} and δ_{test} have to be replaced by the sensitivity values resulting from the evaluation of the deflection vs. displacement curve.

The accuracy of this method relies principally on how accurately the reference spring constant has been determined. In addition, the exact



Variation of cantilever spring constant, calculated according to eq. (2.1). $L_{max} = 210 \mu\text{m}$, $w = 52.5 \mu\text{m}$, $a = 0.37 \mu\text{m}$, $E = 170 \text{ GPa}$. The calculated values agree with experimental ones (not represented here).

position where the two cantilevers touch during the calibration process is of extreme importance: The reference cantilever, in fact, becomes stiffer closer to its base. This simply means that k_{ref} is not constant [see Figure on previous page] but increases along the cantilever according to a power law [see eq. (2.1)]. If for instance the contact point of the two beams is at 200 μm from the base instead of 210 μm , the reference spring constant is 0.014 N/m instead of 0.012 N/m, resulting in an **error** of k_{ref} of about 16%. This also supports my choice of the more accurate Sader method for the calibration of the cantilevers.

2.5.4 Comparison of the calibration procedures

I have discussed three commonly used methods, pointing out their benefits and their back draws. The added mass technique is time consuming, and it also suffers from precision loss in case of a misplacement of the reference weights on the free end of the cantilever. The reference spring technique is faster, but it is affected by the same problem as the previous technique: A correct placement of the test cantilever on the reference spring is essential. The Sader technique, combined with the design of two parallel rectangular cantilevers, provides the most precise and reliable results. I therefore elect this method as my standard procedure to determine the spring constant.

2.6 Force Curves and their Evaluation

In a force measurement, the sample is periodically moved up and down at constant speed by applying a voltage to the piezoelectric translator onto which the sample is mounted. During this process the vertical deflection of the cantilever (against which the sample is pushed) is measured.

The direct result of a measurement with the atomic force microscope or with the particle interaction apparatus is a plot of the cantilever deflection, in [V], as a function of the piezo displacement, in [nm]. This has to be converted to a plot of the force, in [N], as a function of separation between probe and sample, in [nm].

Figure 14 shows a standard force curve. The cyclic process of cantilever approach and retraction starts on the right of the drawing in (0). Here, the cantilever and the sample are at rest. Because of the large distance of the probe from the sample, no surface forces affect the sphere and the cantilever is not deflected. Even when the sample starts to move towards the probe there is a whole interval of no interaction (*zero force region*, (1)). When the separation decreases further, the probe gets into the effective range of the surface forces

and it is deflected (2). In the figure a total attractive force is assumed. At a certain distance the probe may "snap" onto the surface. This happens when the attractive forces exceed the sum of the elastic force of the cantilever plus the repulsive forces. If the sample is pushed further against the sphere, the deflection of the cantilever increases by the same amount as the displacement of the sample (*constant compliance region*, (3)). Finally, the sample is retracted from the contact position. During this process the sphere may stick to the surface due to adhesion forces (4), and at the end it suddenly snaps away from the surface. The whole process of measuring and recording a force curve is often referred to as *force scan*.

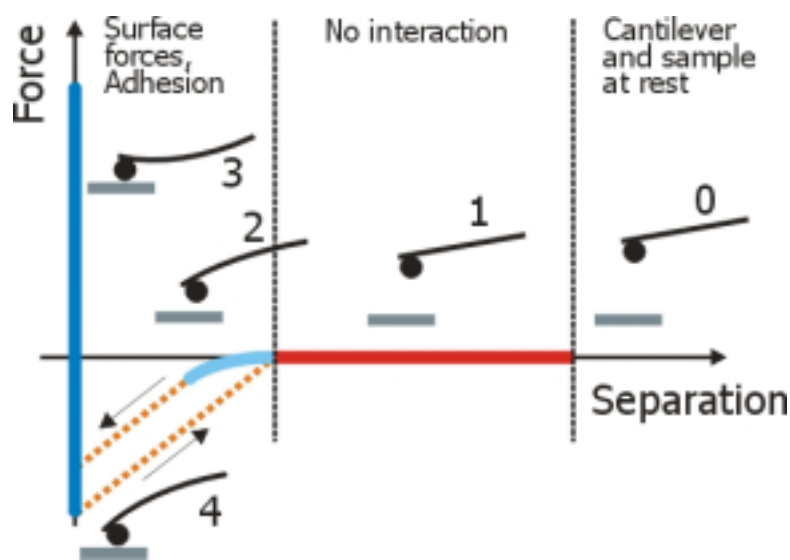


Figure 14: Principle of the measurement of force curves

2.6.1 Force versus distance curves and sphere-sample interaction force

A force vs. distance curve is a plot of the force between a sphere and the sample vs. their separation. The force is obtained by Hooke's law for the cantilever spring:

$$F_{CL} = -k_c \delta_c \quad (2.6)$$

where δ_c is the deflection of the cantilever and k_c the spring constant of the cantilever. To obtain the separation h [see Figure 15] the cantilever deflection δ_c and a possible sample deformation δ_s (both quantities can be positive or negative) have to be subtracted from the position H of the piezo:

$$h = H - (\delta_c + \delta_s) \quad (2.7)$$

Since one does not know in advance the cantilever deflection and the sample deformation, the only distance that one can control is H , i.e. the displacement of the piezo. Therefore, the raw curve obtained by AFM should be called "deflection-displacement curve" rather than "force-distance curve". The latter term should be employed only for curves in which the force is plotted vs. the true sphere-sample separation [see Figure 16], which is obtained with help of eqs. (2.6) and (2.7), once the quantity $\delta_c + \delta_s$ has been measured.

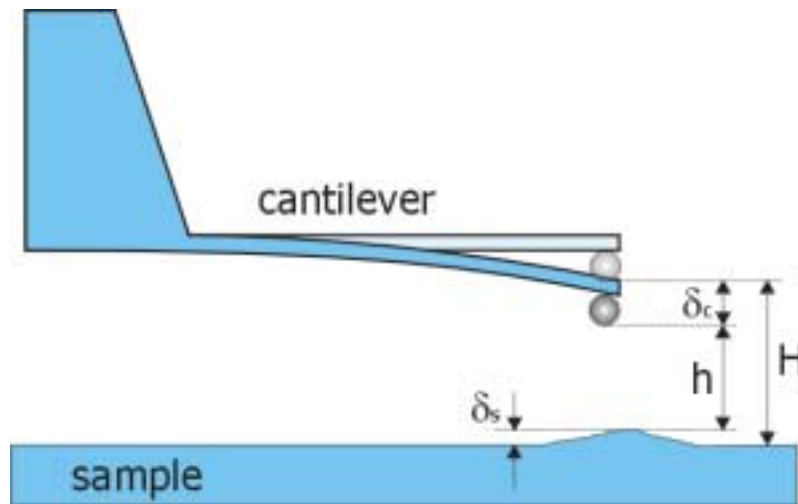


Figure 15: The probe-sample system: h is the actual sphere-surface distance, whereas H is the distance between the sample and the cantilever rest position. These two distances differ by the cantilever deflection δ_c and by the sample deformation δ_s .

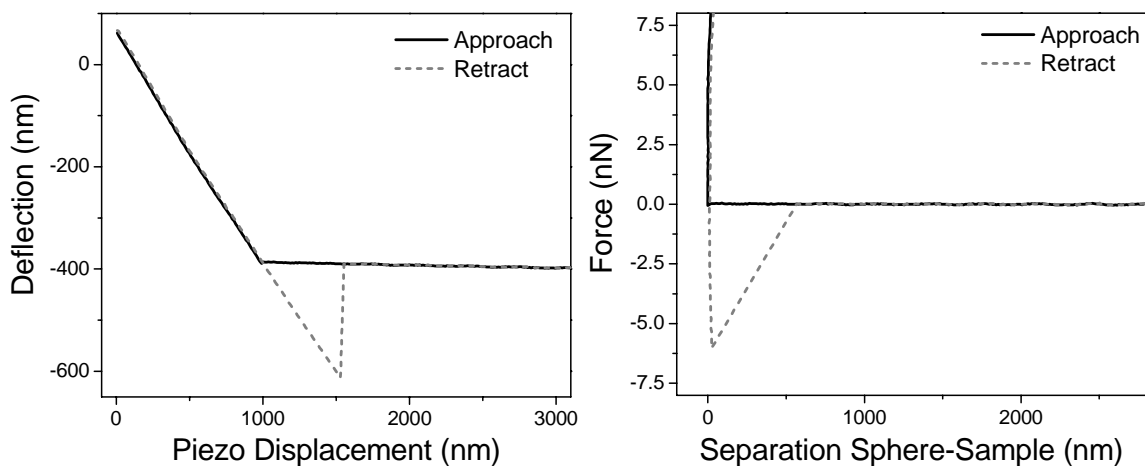


Figure 16: Conversion of a deflection-displacement curve into a force-distance curve. The deflection is multiplied by the spring constant of the cantilever to obtain the force, according to eq. (2.6). The piezo displacement is corrected by the cantilever deflection and the sample deformation to obtain the separation from the surface, according to eq. (2.7).

An AFM distance-displacement (or force-displacement, after multiplication of the deflection with the spring constant) curve does not reproduce the sphere-sample interaction alone, but it is the result of two contributions: The sphere-sample interaction, $F(h)$, and the

elastic restoring force of the cantilever, F_{CL} . This result can be understood by means of the graphical construction shown in Figure 17 [see also 59, 60].

In Figure 17(a) the curve $F(h)$ represents the sphere-sample interaction. For the sake of simplicity, I consider a force modelled like the interatomic *Lennard-Jones* force, i.e., $F(h) = -A/D^n + B/D^m$, with $m > n$. This is representative for the interaction, because it accounts for a long range attraction and a short range repulsion between sample and probe. The lines 1 ÷ 3 represent the elastic force of the cantilever, F_{CL} .

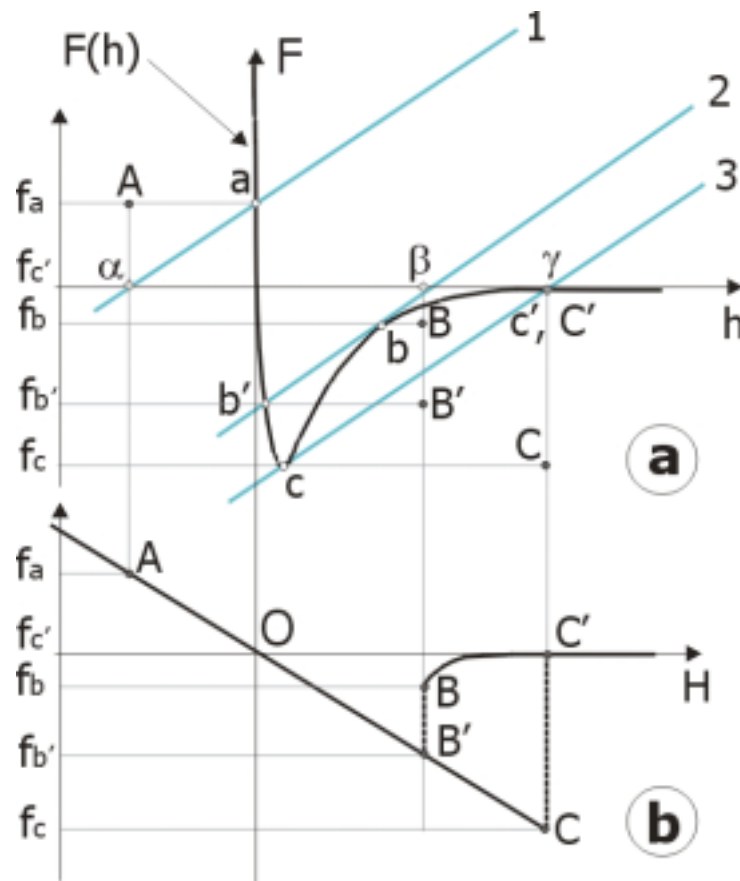


Figure 17: Graphical construction of an AFM force-displacement curve. In panel (a) the curve $F(h)$ represents the sphere-sample interaction and the lines 1, 2 and 3 represent the elastic force of the cantilever. At each distance the cantilever deflects until the elastic force equals the sphere-sample force and the system is in equilibrium. The force values f_a , f_b and f_c at equilibrium are given by the intersections a , b , and c between lines 1, 2 and 3 and the curve $F(h)$. These force values must be assigned to the distances H between the sample and the cantilever rest positions, i.e. the distances α , β and γ given by the intersections between lines 1, 2 and 3 and the horizontal axis. This graphical construction has to be made going both from right to left and from left to right. The result is shown in panel (b). The points A , B , B' , C and C' correspond to the points a , b , b' , c and c' respectively. BB' and CC' are two discontinuities. The origin O in panel (b) is usually put at the intersection between the prolongation of the zero deflection line and the contact line of the approach curve. The force f_c eventually coincides with the zero force.

In Figure 17(b) the AFM force-displacement curve is shown. At each distance value the cantilever deflects until the elastic force of the cantilever equals the sphere-sample

interaction force, so that the system is in equilibrium. The force values at equilibrium f_a , f_b and f_c are given by the intersections a, b and c between lines 1 ÷ 3 and the curve $F(h)$. These force values must not be assigned to the distances h at which the lines intersect the curve $F(h)$, but to the distances H between the sample and the cantilever rest positions, that are the distances α , β and γ given by the intersections between lines 1 ÷ 3 and the horizontal axis (zero force axis). Going from right to left, i.e. approaching the sample, the *approach curve* is obtained. Making the same graphical construction from left to right, i.e. retracting from the sample, gives the *retraction curve*. The points A, B, B', C and C' correspond to the points a, b, b', c, and c', respectively. The analytical expression for the calculation of the sphere-sample force curves was derived by Hao [61].

2.6.2 Hydrodynamic force curves

The force curves described in the experimental part are mostly taken in liquids. They differ from force curves in air because of the resistance of the liquid to the movement of the cantilever and the particle. A schematic of a typical **hydrodynamic force curve** is shown in Figure 18.

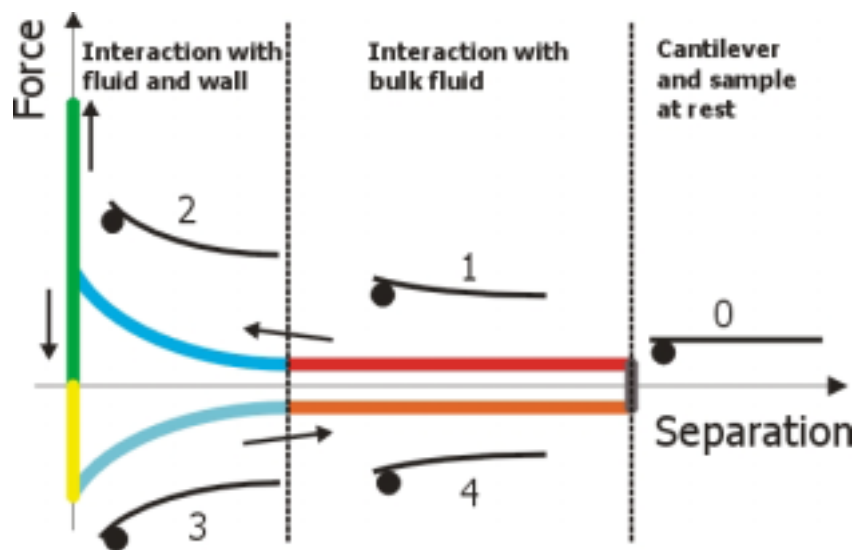


Figure 18: Regions composing a hydrodynamic force curve. Cantilever and microsphere are at rest in (0) and subjected to no force. A constant hydrodynamic force, independent of position, acts on the probe as soon as the sample starts to move (1). Distance dependent forces start to affect the motion of the sphere when it gets closer to the surface (2). After contact, the sample retracts, and the same forces (with an inverted sign) act between sample and probe (3), (4).

The cantilever is at rest in (0), then the sample starts to approach the probe. The cantilever is thus deflected by a constant frictional hydrodynamic force (1) acting on the whole cantilever and on the particle. The position independent force is proportional to the Stokes

friction $6\pi\eta Rv$ with the bulk liquid. The probe starts to "feel" the presence of the wall (2) when the distance dependent hydrodynamic force between sphere and sample starts to play a role. Here, the force is proportional to $6\pi\eta Rv \cdot R/h$, where h indicates the separation. The proportionality continues until contact between sphere and surface is established. When retracting, the cantilever is subjected to a larger deflection as long as the probe interacts with the wall (3). Then the probe is subjected to a constant (lower) deflection (4), due to the sole interaction with the bulk liquid.

Therefore **two physically different regimes** occur: **(I) a constant force** (Stokes friction) acts on both, sphere and cantilever, when $h \gg 0$, and **(II) a position dependent force** adds to the constant force when $h \rightarrow 0$.

2.7 Simulation of Force Curves

I simulated force curves (electrostatic, hydrodynamic and electrokinetic) solving the respective equations (1.20), (1.29), (1.40) and (1.44) in a numerical way, using the mathematical computation program Maple V (Waterloo Maple Inc., Ontario, Canada) and plotting the resulting data.

2.7.1 Electrostatic force

Electrostatic force curves were simulated solving the linearised Poisson-Boltzmann equation (1.17) valid for small potentials, using Derjaguin's approximation (1.29). The sphere moves towards a flat surface in a Newtonian fluid at low velocity ($v_0 = 0.2 \mu\text{m/s}$ in most experiments). Thus, I assume a quasi-static behaviour, i.e. that at every position the equilibrium of the electrostatic forces is achieved. Neglecting other surface forces acting between the sphere and the sample, the electrostatic force is balanced by the restoring force of the cantilever: $F_{es} = F_{CL}$, which is expressed by:

$$F_{CL} = k(h - h_0 - v_0 t) \quad (2.8)$$

h_0 is the initial separation between sphere and surface and v_0 is the velocity the piezo imparts to the sample. In my case the piezo is driven by a triangular function. The term $-v_0 t$ is assumed negative for the approaching and positive for the retracting cycle.

The electrostatic force acting between a rigid, charged sphere and a flat, charged surface, is expressed by eq. (1.29a) for the constant potential case and by eq. (1.29b) for the constant charge case. I simulate the force curves assuming that the surface quantities are identical on the sphere and on the surface

$$\sigma_1 = \sigma_2 = \sigma \quad (2.9)$$

and

$$\Psi_1 = \Psi_2 = \Psi_0 \quad (2.10)$$

Therefore, the equations (1.29) become:

$$F_{es}^{cp}(h) = 4\varepsilon_0\varepsilon\kappa R\Psi_0^2 \left[e^{-\kappa h} - e^{-2\kappa h} \right] \quad (2.11a)$$

$$F_{es}^{cc}(h) = \frac{4}{\varepsilon_0\varepsilon\kappa} R\sigma^2 \left[e^{-\kappa h} + e^{-2\kappa h} \right] \quad (2.11b)$$

Equations (2.11a) and (2.11b) are related with the Grahame's equation:

$$\sigma = \frac{\varepsilon\varepsilon_0\Psi_0}{\lambda_D} \quad (1.23)$$

The dielectric permittivity ε of an electrolyte is described by the empirical expression [62]:

$$\varepsilon = 22 + 57e^{-0.192c} \quad (2.12)$$

where c is the local concentration of the monovalent salt in mol/l. I derive the parameter $\kappa = 1/\lambda_D$ by fitting an experimental electrostatic force curve with a decreasing exponential function of the type of eqs. (1.29a) or (1.29b) having a decay length λ_D .

The above equations (2.11) can be directly plotted, as done in Figure 19. Here the force F is normalised with respect to the radius R of the particle, which is a standard representation of force curves with colloidal probes.

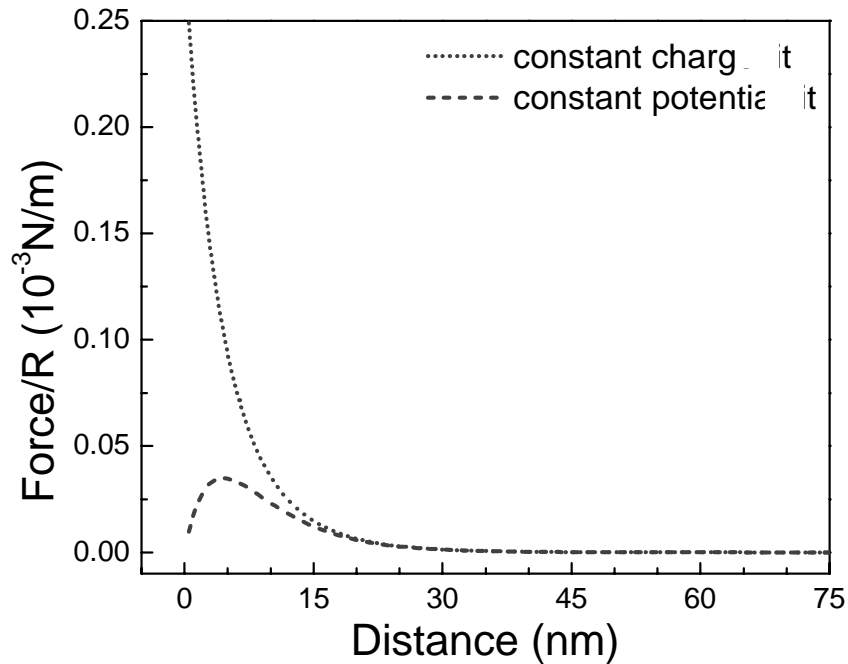


Figure 19: Electrostatic force curve simulation, with $R = 10 \mu\text{m}$, $c = 2 \cdot 10^{-3} \text{ mol/l}$, $\sigma = 1.1 \cdot 10^{-3} \text{ C/m}^2$, $\Psi_0 = 10.1 \text{ mV}$, $\lambda_D = 6.42 \text{ nm}$.

2.7.2 Hydrodynamic force

The hydrodynamic force curves are simulated solving the equation of motion for a sphere moving towards a flat surface in a Newtonian fluid of viscosity η (1.40). This results in a distance dependent force. Constant force contributions accounting for a distributed hydrodynamic pressure on the cantilever and for gravity are also added.

When simulating pure hydrodynamic force curves all surface forces were neglected. In this way the pressure on the sphere is only balanced by the restoring force of the cantilever: $F_{hy} = F_{CL}$. The effect of the viscous drag is to retard the sphere and to modify the separation between sphere and surface at a given time t compared to the ramp driving the piezo. This results in a non-uniform velocity of the sphere during the approach and retraction cycle.

The hydrodynamic resistance to the approach/retraction of a rigid, uncharged sphere of radius R and a flat, uncharged surface is expressed by eq. (1.40), where $f^* = 1$ if applying the no-slip boundary condition.

The restoring force of the cantilever spring is expressed by eq. (2.8).

Combining eqs. (1.40) and (2.8) gives the equation of motion for a particle in a Newtonian fluid, with or without slip:

$$-\frac{6\pi\eta R^2}{h} \cdot \frac{dh}{dt} f^* = \begin{cases} k(h - h_a - v_0 t) & \text{for } 0 < t \leq t_a \\ k(h - h_r + v_0 t) & \text{for } t_a < t \leq t_r \end{cases} \quad (2.13)$$

h_a and h_r are the initial separations of the sphere and the surface, respectively during approach and retraction; t_a and t_r are the approach and retraction intervals. I solve eq. (2.13) numerically in order to obtain the simulated force curves shown in Figure 20 for some typical experimental values. A slip length b of 10 nm has been used, as this value is close to experimental findings.

How can I be sure that I measure the force acting on the particle and have no contribution from the viscous drag on the cantilever? Due to [63], the viscous drag depends linearly on the velocity for rectangular cantilevers of the same dimensions as in my case ($L \approx 200 \mu\text{m}$ and $w \approx 50$) if the radius of the sphere is large enough ($R \geq 5 \div 7 \mu\text{m}$). Moreover, this drag force depends on the length and width of the cantilever and on the viscosity of the liquid in which the cantilever is immersed. This is valid for all my measurements. Thus, the distributed drag on the cantilever is considered as a force, F_{drag} , which appears as a

velocity-dependent but very low offset in the distance-dependent surface forces I am interested in.

This distributed load acting on the whole cantilever has also been used elsewhere to find the value of the spring constant [64].

As already stated in chapter 1.3, the body force term F_b has the form of eq. (1.31). Once the dimension of the particle is given, F_b can be calculated: It is constant too, and always parallel to \vec{g} .

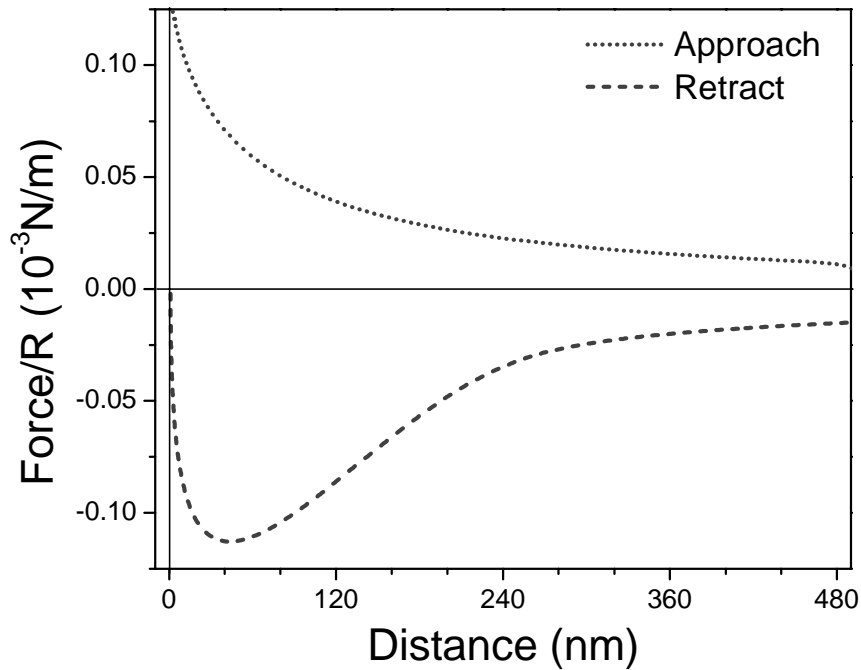


Figure 20: Simulated hydrodynamic force curve, with $R = 10 \mu\text{m}$, $\eta = 0.89 \cdot 10^{-3} \text{ kg/m/s}$, $v_0 = 40 \mu\text{m/s}$, $k = 0.0116 \text{ N/m}$, slip length $b = 10 \text{ nm}$, $h_a = 500 \text{ nm}$, $h_r = 1 \text{ nm}$.

Another term might be considered: The one accounting for the acceleration of the cantilever-particle system, which could be expressed by the formula:

$$F_{acc} = m^* \frac{d^2 h}{dt^2} \quad (2.14)$$

where m^* is the effective mass of the system. This consists of two contributions: The mass of the sphere and the effective mass of the cantilever:

$$m^* = m_{sphere} + C_1 m_{CL} \quad (2.15)$$

For a cantilever immersed in water, the factor C_1 expresses the fact that the moving cantilever drags some liquid along with it, which increases its mass [65]. For my rectangular cantilevers C_1 maximally reaches a value of 50 [65]. The acceleration of the system varies with the distance of the sphere from the surface. It is maximal before contact and this value can be found from experimental curves. Depending on the scanning velocity

of the piezo, $|d^2h/dt^2|_{\max} \sim 0.8 \cdot 10^{-6} \text{ m/s}^2$ for $v_0 = 40 \text{ } \mu\text{m/s}$. This results in a force F_{acc} that is several orders of magnitude smaller than, e.g. F_{drag} or F_b , and may therefore be neglected.

F_{drag}/R is positive for approach, negative for retraction. Its value is approximately $3.5 \cdot 10^{-6} \text{ N/m}$ for cantilever dimensions $l = 210 \text{ } \mu\text{m}$, $w = 52.5 \text{ } \mu\text{m}$ and velocity $v_0 = 40 \text{ } \mu\text{m/s}$. F_b/R is always negative, and its value is approximately $4.9 \cdot 10^{-6} \text{ N/m}$ for a sphere with a radius of $10 \text{ } \mu\text{m}$. This force has been included in the simulation shown in Figure 20.

2.7.3 Electrokinetic force

The electrokinetic force occurs when hydrodynamic and electric effects are present at once [see chapter 1.4 and eq. (1.44)]. To simulate the electrokinetic force curves, first the equation of motion for a sphere moving towards a flat surface in a Newtonian fluid as in the hydrodynamic case has to be solved. Additionally, I account for the distance dependent electrostatic force [eq. (2.11)] by choosing the approach

$$F_{ek} = -\frac{6\pi\eta R^2}{h} \cdot \frac{dh}{dt} f^* + F_1(e^{-h/\lambda_D} \pm e^{-2h/\lambda_D}) \quad (2.16)$$

and neglecting other surface forces acting between the sphere and the sample.

The sign in the brackets depends on the choice of the constant charge ("+") or the constant potential ("-") model. F_1 is proportional to the amplitude of the double layer repulsion and is derived from fits of experimental curves.

The electrokinetic force is balanced by the restoring force of the cantilever: $F_{ek} = F_{cl}$. As stated earlier, the hydrodynamic drag retards the sphere compared to the driving force, resulting in a non-uniform sphere velocity during the approach and the retraction [chapter 2.7.2] whereas the electric effect is responsible for a deceleration of the sphere [chapter 2.7.1].

The restoring force of the cantilever spring is expressed by eq. (2.8).

Combining eqs. (2.16) and (2.8), I obtain the equation of motion for a charged particle in a Newtonian fluid, with or without slip:

$$-\frac{6\pi\eta R^2}{h} \cdot \frac{dh}{dt} f^* + F_1(e^{-h/\lambda_D} \pm e^{-2h/\lambda_D}) = \begin{cases} k(h - h_a - v_0 t) & \text{for } 0 < t \leq t_a \\ k(h - h_r + v_0 t) & \text{for } t_a < t \leq t_r \end{cases} \quad (2.17)$$

I solve eq. (2.17) numerically in order to obtain simulated force curves [see Figure 21]. They contain the constant contributions from the drag on the cantilever and from the body force, as pointed out in chapter 2.7.2.

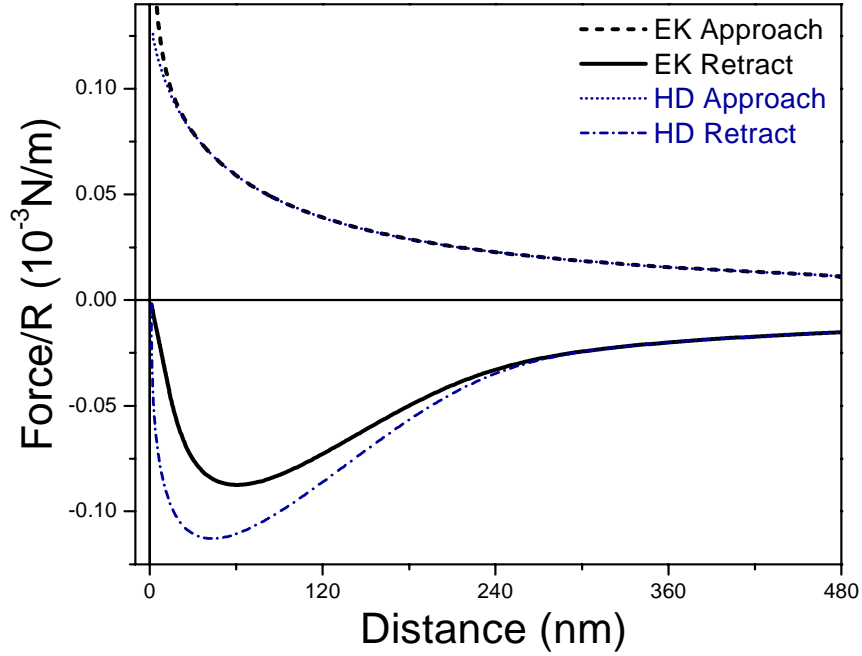


Figure 21: Simulated electrokinetic force curve (EK), with $R = 10 \mu\text{m}$, $\eta = 0.89 \cdot 10^{-3} \text{ kg/m/s}$, $v_0 = 40 \mu\text{m/s}$, $k = 0.0116 \text{ N/m}$, $\lambda_D = 6.42 \text{ nm}$, slip length $b = 10 \text{ nm}$, $F_1 = 2 \text{ nN}$, $h_a = 500 \text{ nm}$, $h_r = 1 \text{ nm}$. The pure hydrodynamic curve (HD) remarkably differs from the electrokinetic force curve only during the retraction. The parameters of (HD) are the same as for the electrokinetic curve, except for $\lambda_D = 0$.

3 Cantilever Fabrication Process

In this chapter I describe the design and the techniques I employed for the fabrication of the cantilevers used for all measurements and experiments. Design, as well as fabrication, were carried out at the facilities of the IMM (Institute for Microtechnology Mainz, Germany). Conventional micro machining techniques (as LIGA, VLSI, E-beam / Ion-beam / X-ray lithography, electroforming, laser structuring) are ideal for fabricating thin planar structures which have lateral dimensions down to about 1 μm . Thin film cantilevers of different geometries can be made out of a variety of materials, including thermally grown oxide films and vapour deposited metals and dielectrics. For my application, the cantilever must meet the following criteria: (1) a small spring constant k , for being able to detect small forces; (2) a high resonant frequency ω_0 and a high mechanical quality factor Q_f in order to be insensitive to external mechanical noise; (3) a high lateral stiffness to be sensitive to vertical forces only (4) incorporation of a reflective surface for deflection sensing. In a first place, these requirements limit the spectrum of the eligible materials, and its choice dictates the suited micro machining procedures. Useful references for the section regarding calculation of spring constant, quality factor and resonant frequency and for design are [60, 66, 67, 68, 69], for material properties see [70], for fabrication see [66, 69, 71].

3.1 Types of Cantilevers and Materials

The most common cantilevers are triangular or rectangular, with a sharp tip (for AFM imaging) or without tip (for fixing any kind of particles at the free end). The lateral stiffness depends on the material and on the shape of the cantilever. Triangular cantilevers are less sensitive to torsional movements compared to rectangular ones. Since my application required the acquisition of force curves with little risk of lateral torsion, I can use rectangular cantilevers,



SEM micrograph of triangular and rectangular cantilevers

because their spring constant can be easily determined from eq. (2.4). To facilitate the placing of the microsphere on the longitudinal axis and at the free end of the cantilever, the rectangular beams terminate with a triangular cap (tip angle 120°).

The materials commonly used for cantilevers are listed in Table 1, together with their relevant mechanical properties.

Material	ρ [kg/m³]	E [GPa]
Silicon	2330	180
SiO ₂	2200	60
Si ₃ N ₄	3100	210
Poly-cristalline silicon	~2300	170

Table 1: Properties of most common cantilever materials.

3.2 Coating Techniques

Here, I present an overview of the commonly used coating processes to deposit layers of different materials on a substrate wafer during the cantilever production. These layers can either serve as the cantilever material itself, or as intermediate or protective layers during the later micro machining processes.

The overview is not intended to give a detailed description of all the process parameters, for which we recommend to refer to the literature cited above.

3.2.1 Thermal oxidation

Oxygen reacts with silicon in an oven at a temperature of about 1100°C and amorphous silicon oxide (SiO₂) forms. Two main kinds of oxidation processes are employed:

- **Dry oxidation:** Oxygen reacts directly with silicon. The result is a low oxidation rate, but a more compact (higher density) layer.
- **Wet oxidation:** H₂ and O₂ are injected in the reaction chamber and water vapour forms which reacts with the silicon. The diffusion coefficient of H₂O into the silicon substrate is higher than that of pure O₂, therefore the growing rate of the oxide layer increases.

3.2.2 Chemical vapour deposition (CVD)

Gases glide over the silicon surface of the wafer and react with it:

- **Low pressure chemical vapour deposition (LPCVD):** Takes place at low pressure (40 Pa), but allows a more homogeneous growth. Even if the wafer surface shows pits or protruding edges, these are smoothed during the deposition process.
- **Plasma enhanced chemical vapour deposition (PECVD):** The reaction is stimulated via a plasma, so the temperature can be kept low and the substrate does not suffer too much from abrupt temperature changes.

Key factors of these processes are mainly temperature and pressure.

3.2.3 Physical vapour deposition (PVD)

Allows the deposition of metals on a substrate.

- **Evaporation:** In a vacuum chamber ($P < 10^{-3}$ Pa) metal is brought to evaporation via an electron beam. The vapour then hits the targets placed above the pot containing the metal.
- **Sputtering:** In a vacuum chamber ($P < 0.5$ Pa) an Argon plasma (Ar^+) is ignited and accelerated towards the metal target (on the cathode), which is pulverised. The metal atoms are attracted by the substrate on the anode.

The evaporation has the advantage that the material hits the target from one direction, depositing a uniform and smooth layer only on the exposed surface. Sputtering, on the contrary, results in rougher layers and the material hitting the target from all directions, but it has the advantage of requiring lower pressures than the evaporation process.

3.3 Structuring Techniques

Several procedures fall under the name of structuring techniques. The desired structures are first designed at a computer (with AutoCAD or with other programs), then transferred to a chromium mask. The structures on the mask is then imprinted on the wafer via lithographic processes, using photosensitive photo resists. These protect those parts of the wafer, which do not need to be structured, during the subsequent etching process.

3.3.1 Photolithography

This is the process by which the pattern on the mask is imprinted on the wafer, during several steps:

Dehydration (30 minutes / 150°C):	The wafer is put in an oven and heated up. This guaranties good adhesion of the photo resist
Spin-coating-(photo resist covering):	The wafer is totally covered with a photo resist. Layers of $0.5 \div 3 \mu\text{m}$ are usual
Pre-bake (60 seconds / 100°C):	During this step the photo resist is hardened and most of the solvent evaporates
Placement of the mask:	The mask is placed on the coated wafer
Exposure to UV light:	The light changes the chemical properties of the photo resist where it is not protected by the mask
Development:	The wafer is immersed in an alkaline bath (e.g. NaOH) and the previously exposed parts of the photo resist dissolve. The structure has now been imprinted in the photo resist on the wafer
Post-bake / Hard-bake (30 minutes / 105°C):	The whole solvent escapes from the photo resist, making it more resistant to subsequent etching baths

Keeping the description very general, the **photo resist** consists of three components:

- **Matrix material:** Resin, it is the core material of the photo resist, not influenced by the UV light and resistant to the etching process.
- **Sensitiser:** Is the photo-active component, it changes its chemical properties upon exposure to UV light.
- **Solvent:** Determines the viscosity of the photo resist.

3.3.2 Chromium mask

Chrome blanks are basically glass plates with defined optical transmission ($T = 85\%$ at $d = 0.35 \text{ m}$), mechanical flatness (2 mm/m), and parallelism. On these blanks a controlled film of chromium (80 \div 100 nm) is deposited maintaining excellent adhesion and uniformity of thickness ($\pm 5\%$) over its extended surface. Since these blanks are used for fabrication of masks by E-beam process, film resistivity ($20 \Omega/\text{m}^2$) is an essential requirement. In addition, deposited chromium film should have a pinhole density of 0.05 pcs/cm², in order to form a close layer.

Different types of chrome masks generally differ for the precision with which they replicate the desired patterns. A measure for the quality of a mask is the absolute precision (distance between two edges) and the roughness at the edges of the structures [see Figure 22]. At present, the technology limits the maximal resolution to 50 nm. I designed the masks for the cantilever production-run at the IMM. At the MZD (Maskenzentrum Dresden, Germany) the structures of the masks were drawn on the chromium layer by means of an E-beam.



Figure 22: Example of bad absolute precision (central image) and of high edge roughness (right image). The original structure is presented in the left drawing, and is also under laid to the other two images to mark the differences. According to one's needs, a trade-off between the two characteristics is usual.

Two methods exist for placing the mask relatively to the photo resist covered wafer during exposure to the UV light:

- **Contact exposure:** The mask is put in contact with the wafer. Advantage is that the structures are transferred with no loss of precision from the mask onto the wafer. Disadvantage is that the mask may be contaminated by photo resist particles after retraction from the wafer.
- **Proximity exposure:** The mask is not in contact, but stays at some distance from the wafer. Advantage is that the mask remains clean from contaminants, so that it can be re-used for other wafers. Disadvantage is that the structure on the wafer is less precise than the original on the mask.

Since I wanted to produce several wafers of SiO₂ and poly-silicon cantilevers, I chose the proximity exposure.

3.3.3 Etching processes

Etching processes differ in the etching direction and in the material which is affected by the etching in the following way:

- **Isotropic:** Same etching rate in any direction
- **Non-isotropic:** Higher etching rate in one direction
- **Selective:** Affects only the desired material
- **Non-selective:** Affects all exposed materials

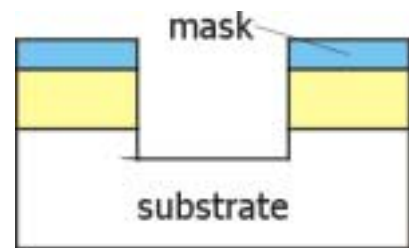
Depending on the combinations of the above processes, one distinguishes four etching processes:

3.3.3.1 Dry etching

Physical etching

Non isotropic, non selective

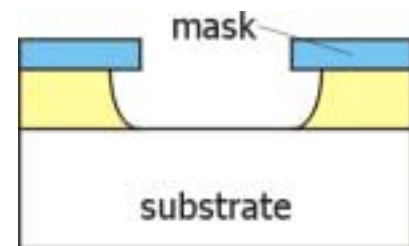
Ar⁺ ions are ionised in a plasma and accelerated towards the substrate, where they beat out atoms, even from the substrate.



Chemical etching

Isotropic, selective

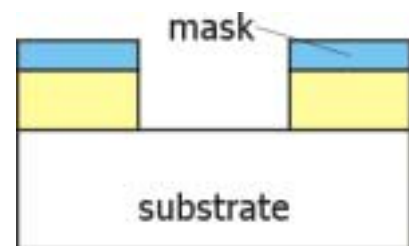
In plasma etching, ions and radicals are generated and the plasma etches the material in any direction.



Chemical-physical etching or reactive ion etching (RIE)

Non isotropic, selective

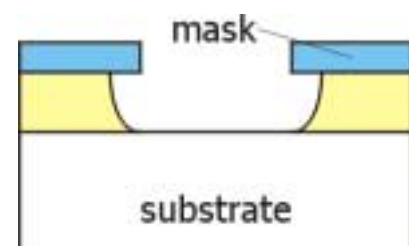
Ions are accelerated towards the substrate and beat out atoms in a selective way, thus not affecting the substrate.



3.3.3.2 Wet etching

Isotropic, highly selective

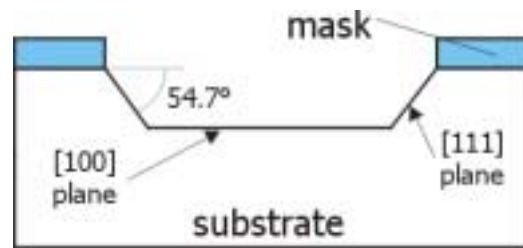
The wafer is immersed in a solution of acids (e.g. buffered hydrofluoric acid - BHF) or bases (e.g. potassium hydroxide - KOH), and the choice of the



proper etching medium allows different etching rates for layers of different materials

3.3.3.3 Silicon wet etching

The figure nearby shows the case of a [100] silicon wafer immersed in an etching bath of KOH. The angle of 54.7° is typical, and depends on the crystallographic structure of silicon.



The etching rate depends on three parameters:

- Temperature
- KOH concentration
- Doping of the substrate

3.4 Example of Flow-Chart for poly-silicon Cantilevers

I utilised two kinds of cantilever materials: Poly-crystalline silicon and silicon oxide. Three masks were necessary, one for the front side (form of the cantilevers) and two for the back side (structure of the chip). Each lithographic process necessitates the use of one mask.

In the following, I describe the single steps in the poly-silicon cantilever production run [see also Figure 23]. Cantilever lengths are $l = 90, 140, 180, 210 \mu\text{m}$, the widths w are equal to $l/4$ for each cantilever and the thickness t is equal to 400 nm.

- 1 Marking of the substrate: 5" DSP silicon wafer
- 2 Thermal oxidation in the diffusion oven: 500 nm SiO_2 on both sides of the wafer
- 3 LPCVD poly-Si deposition: 400 nm poly-Si on both sides of the wafer
- 4 Advanced silicon etching (ASE) for removal of the poly-Si layer from the back side
- 5 PECVD oxide deposition: 500 nm SiO_2 on both sides
- 6 Lithography on the front side
- 7 Structuring of the oxide layer (RIE): Selective etching of 500 nm SiO_2 on the front side up to the poly-Si
- 8 ASE structuring of the cantilevers: Etching of 400 nm poly-Si on the front side
- 9 Structuring of the oxide layer (RIE): Selective etching of 500 nm SiO_2 on the front side up to the silicon
- 10 Removal of the remaining photo resist from the front side
- 11 Deposition of an etching protection (photo resist) on the front side

- 12 First lithography on the back side
- 13 Structuring of the oxide layer (wet etching with BHF): Selective etching of 1 μm SiO_2 on the back side up to the silicon
- 14 Removal of the remaining photo resist from the front and back sides
- 15 Deposition of an etching protection (Poly-Imid) on the front side
- 16 Second lithography on the back side
- 17 ASE chip structuring: 150 μm silicon on the back side
- 18 Structuring of the oxide layer (wet etching with BHF): Selective etching of 1 μm SiO_2 on the back side up to the silicon
- 19 ASE chip structuring: 475 μm silicon on the back side
- 20 Removal of the remaining photo resist from the back side and of the Poly-Imid layer from the front side
- 21 Removal of the oxide layers (wet etching with BHF): Front and back sides

The flow-chart for the SiO_2 cantilever production is similar, it differs only by a reduced number of steps.

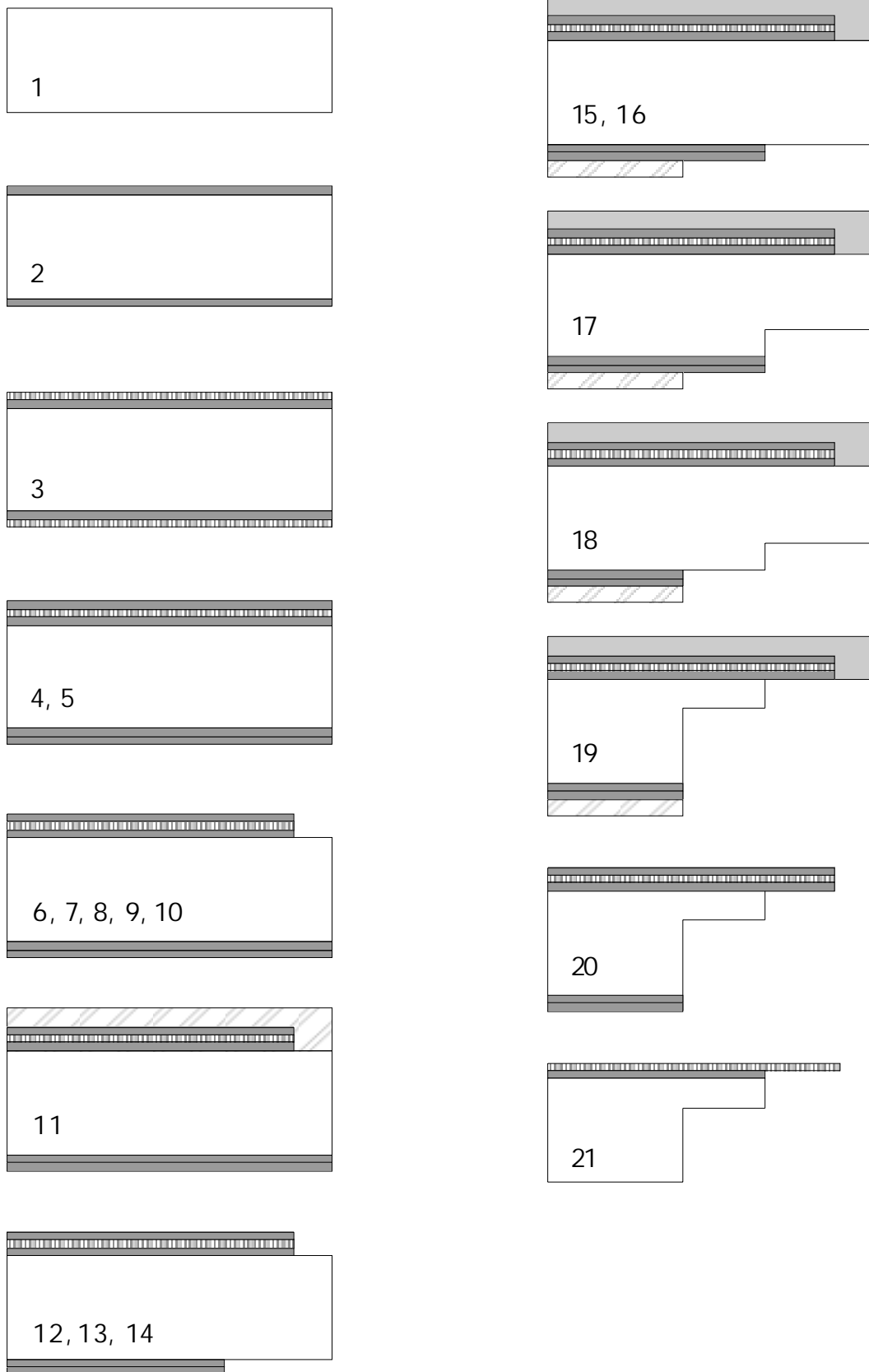


Figure 23: Steps of the flow chart for the production of poly-crystalline silicon cantilevers of 400 nm thickness.

4 Results and Discussion

In this chapter I describe the results of hydrodynamic, electrostatic and electrokinetic force measurements between hydrophilic surfaces (mica and glass) in aqueous medium using the colloidal probe technique.

The *hydrodynamic force* critically depends on the boundary condition at the solid/liquid interface. Thus, by modelling measured force curves the boundary condition can be inferred. My experiments evidence significant slip for water on hydrophilic surfaces. This evidence agrees with a more general boundary condition, stating that the slip length depends not linearly on the shear the liquid undergoes.

Another purpose of this study is to detect *special electrokinetic effects* in force measurements. Electrokinetic effects, such as the occurrence of streaming and sedimentation potentials, arise when a polar liquid flows over a charged solid surface [16]. When a colloidal particle induces shearing of the liquid at, or near, a charged surface, this in turn leads to an electro viscous force [72] acting on the microsphere. These effects have been studied for "small" experimental velocities (particle velocity below a tenth of microns) and "small" shear rates (below 1000 s^{-1}). In my experimental set-up the particle can achieve velocities of a hundred of microns per second and the shear rate can be as large as $8000 \text{ s}^{-1} \div 10000 \text{ s}^{-1}$, therefore the issue arises if some *special* electrokinetic effects might be generated under these conditions.

To detect slip and electrokinetic effects three types of experiments are performed:

- "**Hydrodynamic**" force curves F_{hy} were recorded with high approaching velocities ($5 \text{ } \mu\text{m/s} \leq v_0 \leq 75 \text{ } \mu\text{m/s}$). High salt concentrations (100 and 200 mM, monovalent salt) and preferably small pH values (for a low surface charge density σ) are used, in order to keep the electric double layer force negligible for distances h larger than 2 nm. I therefore assume that for $h > 2 \text{ nm}$ the interaction is purely hydrodynamic.
- "**Electrostatic**" force curves F_{es} were recorded at low approaching velocity ($0.05 \text{ } \mu\text{m/s} \leq v_0 \leq 0.2 \text{ } \mu\text{m/s}$, so that the hydrodynamic force becomes negligible) in 1 or 2 mM monovalent salt at a pH ~ 11 (in order to maximise surface charge density σ). Under these conditions the electrostatic double layer force dominates since the surfaces of silicon oxide and mica are negatively charged and the Debye length is large ($\lambda_D > 6 \text{ nm}$).

- "**Electrokinetic**" force curves F_{ek} were recorded at high approaching velocities ($5 \mu\text{m/s} \leq v_0 \leq 75 \mu\text{m/s}$) in an electrostatic field (1 or 2 mM monovalent salt, pH \sim 11). Electrokinetic force curves are finally compared to simulated force curves, which take into account the electric double layer force and the hydrodynamic force.

All experiments are performed with a NanoScope III **AFM** (Digital Instruments, Santa Barbara, U.S.A.) and with the particle interaction apparatus (**PIA**).

If not stated otherwise, the dimensions of the used cantilevers are $l = 210 \mu\text{m}$ and $w = 52.5 \mu\text{m}$, the radius of the borosilicate sphere fixed on the cantilever is $R = 10 \mu\text{m}$, and the substrate is mica.

Deformations of the **probe** can be neglected in this work. The deformation of the borosilicate glass microsphere in contact with the flat mica surface has been estimated, using JKR theory, to be less than 0.1 nm. References to deformation theories are in [73, 74, 75, 76, 77].

4.1 The Electric Double Layer on Oxide Surfaces and on Mica

The surface charge and potential of an insoluble oxide is partly determined by the pH of the solution in which it is immersed. In fact, the surface charge σ in oxide systems is caused by the pH and ion-dependent dissociation of amphoteric surface hydroxyl (OH) groups. For example, the surface charge of silica (SiO_2) increases with electrolyte concentration and pH [Figure 24], as qualitatively has been shown by titrations of silica in the pH range from 1.8 to 9 [78]. The surface potential Ψ_0 is a function of both pH and the electrolyte concentration.

Mica is a mineral of the alumino-silicate group having a sheet or plate like structure with different composition and physical properties [see Figure on next page]. It forms flat six-sided monoclinic crystals with a remarkably clean cleavage in the direction of the crystal surfaces, which permits them to easily split into optically flat films. In muscovite or white mica one quarter of the tetrahedral silicon atoms are replaced by aluminium. This confers a very large negative charge ($\sim 2e$ per nm^2) to the lattice on each sheet. This charge is balanced by K^+ ions, placed in the hexagonal hole of the silica sheet. The ideal formula is $K^+ [(AlO(OH))_2(AlSi_3O_8)]^-$.

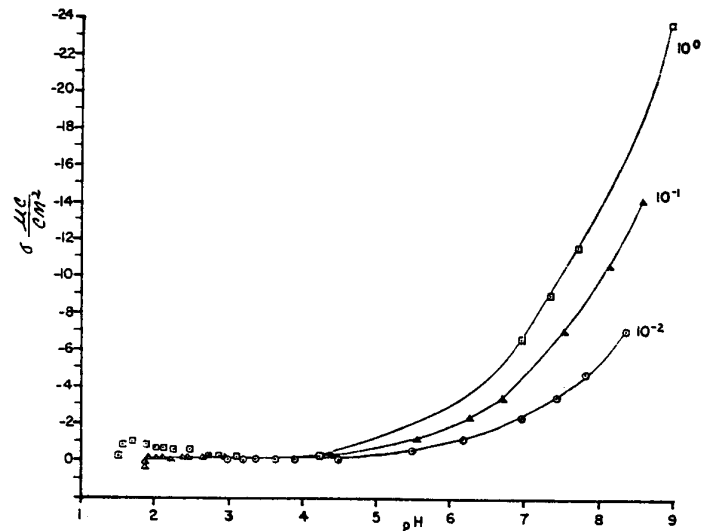
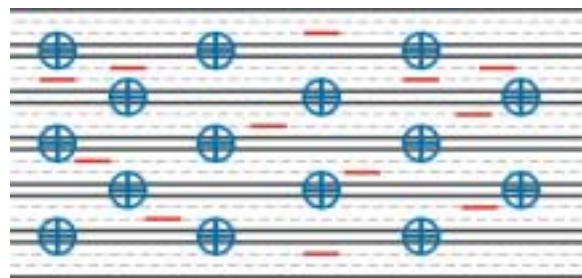


Figure 24: Charge densities for CAB-O-SIL M-7 (a pyrogenic type of silica) in KCl as a function of concentration [from 78].

When cleaved sheets are immersed in aqueous solution some fraction of these exposed ions dissociates to form a diffuse electric double layer which can be accurately measured using the SFA or the AFM. In addition, the exposed basal plane acts as an ion-exchanger so that the K^+ ions can be almost completely replaced with other cations in the solution.



Schematic diagram of the muscovite mica structure. The potassium ions are shown \oplus and they balance negative charges in the silica layers caused by the substitution of about a quarter of the silicon ions by aluminium [from 16].

4.2 Hysteresis in High-Speed Force Curves

It is a known fact that force curves taken at high speeds show a **scan-rate dependent hysteresis** in the contact region [Figure 25]. The hysteresis increases linearly with increasing scan-rate. It has been previously [79] stated that this hysteresis might be caused by the rolling of the sphere on the substrate, or by frictional or adhesive forces. Due to experiments performed in this work, it was shown that this effect is caused by a retarded response of the piezo to the driving signal. This is done by simultaneously generating the driving signal and monitoring the actual position of the piezo on an oscilloscope. The retardation leads to a loss of synchronization between data generation for piezo control and

deflection data acquisition. This effect can easily be corrected during the off-line calibration procedure of the force curves.

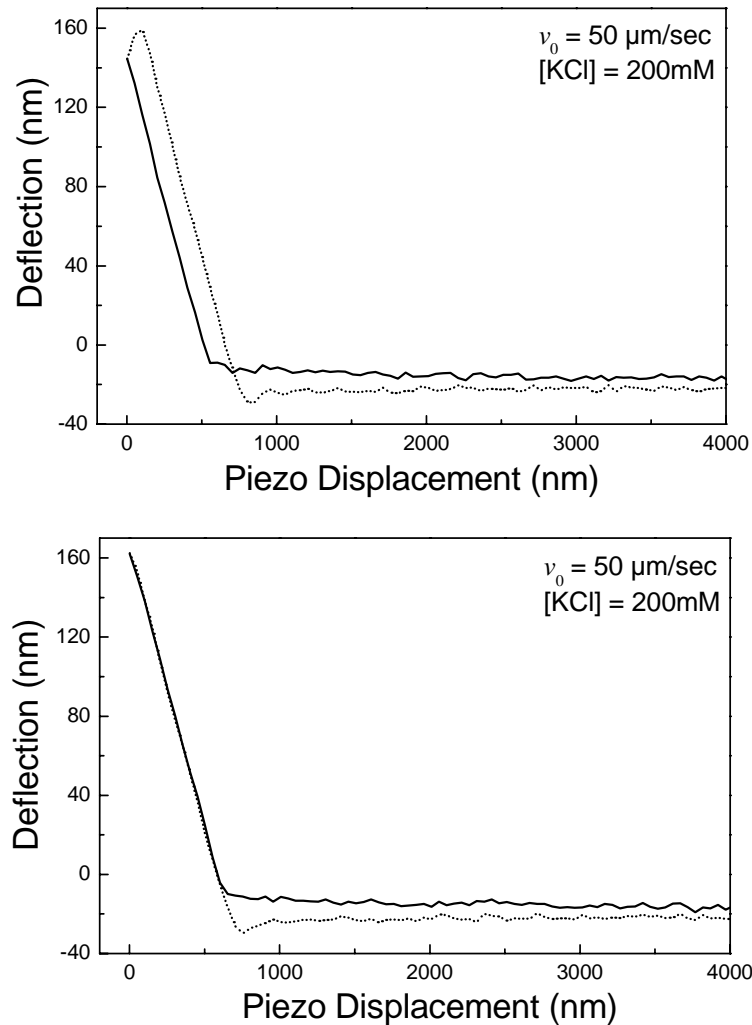


Figure 25: Hysteresis in a deflection-displacement curve at a speed $v_0 = 50 \mu\text{m/s}$. The upper curve shows the originally acquired data. The lower curve shows data after the off-line correction.

4.3 The Hydrodynamic Force

A set of typical hydrodynamic force curves are presented in Figure 26. The measurement is performed in an electrolytic solution of NaOH 0.1 M, at a pH value of 13. The calibrated spring constant (Sader method) is $k = 0.0129 \text{ N/m}$. The force is normalised by dividing it by the radius R of the glass particle. Approaching and retracting parts of force curves are indicated by arrows. Positive forces are repulsive, negative forces attractive. The curves are recorded varying the scan velocity v_0 of the piezo.

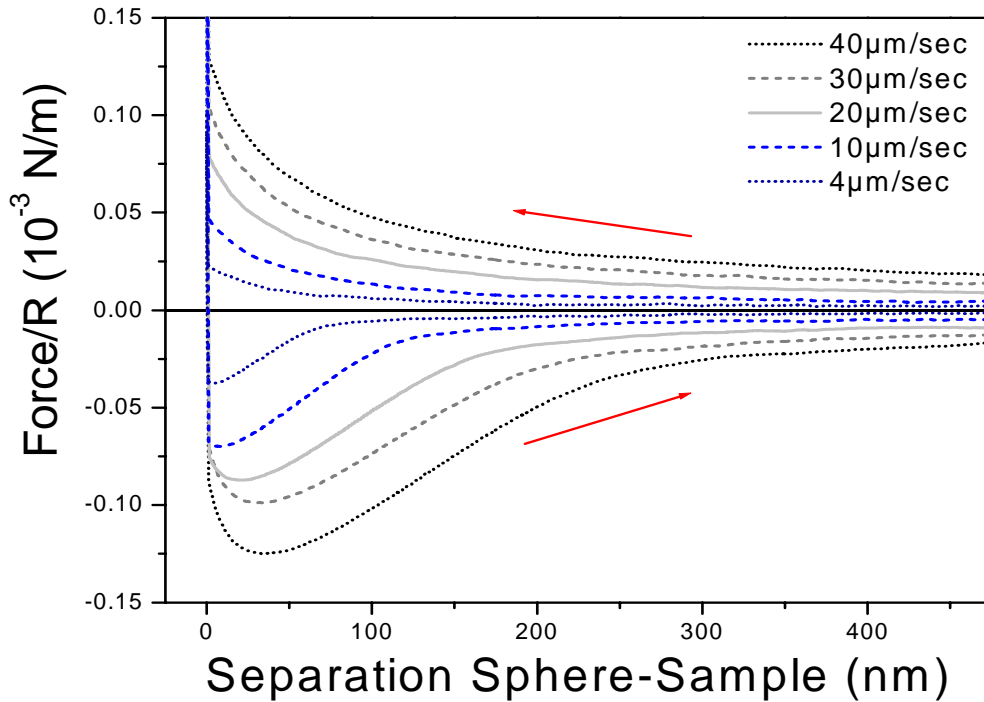
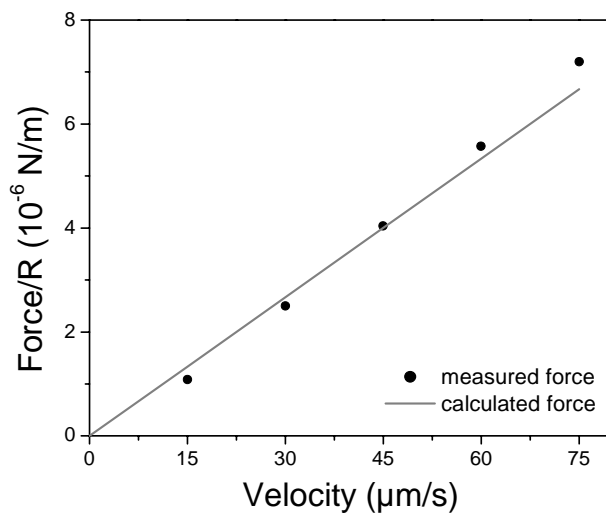


Figure 26: Set of five measured hydrodynamic force curves. The sample approach velocity v_0 varies from $4 \mu\text{m/s}$ to $40 \mu\text{m/s}$. The bulk viscosity of the liquid is $\eta = 0.89 \cdot 10^{-3} \text{ kg/m/s}$.

At high velocities the Stokes friction causes a deflection of the cantilever which does not depend on the distance [79, 80, 81]. More precisely, an apparent constant repulsive force is observed. Likely, an apparent attraction is observed at large distances when retracting the sample. This distance-independent Stokes friction [see Figure nearby] increases linearly with the velocity v_0 . With the Stokes equation of a sphere, $F_{St} = 6\pi\eta R^* v_0$, I derive an *effective radius*



Stokes friction, increasing linearly with velocity. The full circles (●) represent the measured data. The line represents the Stokes friction assuming an *effective radius* $R^* \sim 53 \mu\text{m}$.

R^* for the system cantilever plus particle of about $53 \pm 4.5 \mu\text{m}$. This is larger than the particle radius, because the cantilever adds a constant hydrodynamic friction, as already described before [see chapter 2.7.2]. On the other hand, it is smaller than the square root of the area of the cantilever, which is $R^* < \sqrt{wL} = 105 \mu\text{m}$. The reason is that those parts of

the cantilever which are close to its base contribute less since the effective spring constant is higher than at the end of the cantilever [see chapter 2.5.3].

When the particle approaches the mica surface the repulsive force increases. This hydrodynamic distance-dependent repulsion increases with increasing approaching velocity. When retracting the particle with a low velocity usually the particle adheres to the sample and an adhesion force has to be overcome. At high retracting velocities a stronger apparent attraction is observed because an additional hydrodynamic force has to be overcome: Before the particle can retract, the liquid has to fill the widening gap between particle and flat surface.

Two hydrodynamic force curves recorded at $v_0 = 4 \mu\text{m/s}$ and $v_0 = 40 \mu\text{m/s}$ are shown in Figure 27.

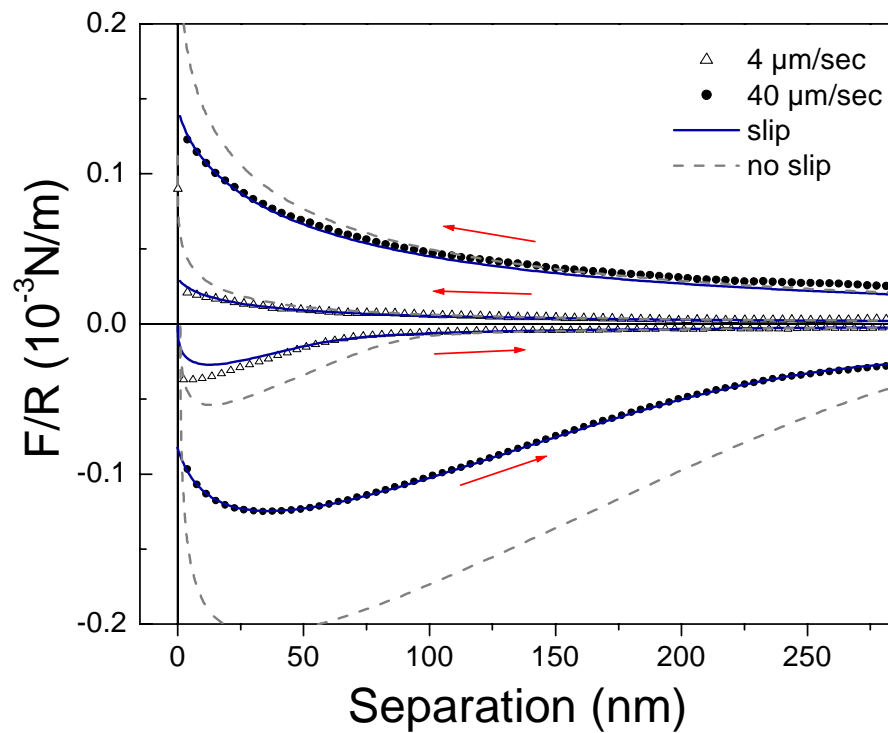


Figure 27: Hydrodynamic force curves measured at low velocity ($v_0 = 4 \mu\text{m/s}$, Δ) and high velocity ($v_0 = 40 \mu\text{m/s}$, \bullet) in aqueous electrolyte (200 mM KCl, pH 5) on mica. The force is normalised by dividing it by the radius of the glass particle $R = 10 \mu\text{m}$. Only each 15th point is shown. Approaching and retracting parts of force curves are indicated by arrows. Simulations are calculated according to eq. (2.16) without slip ($f^* = 1$, dashed) and with slip (slip length $b = 8.6 \text{ nm}$, continuous line). Positive forces are repulsive, negative forces attractive.

The measurement is performed in a KCl solution of 200 mM at pH 5. The calibrated spring constant is $k = 0.0130 \text{ N/m}$. Simulations are shown together with the experimental curves, using both the no-slip and the slip conditions. The slip length b is the only adjustable parameters in the simulation, since the radius R of the particle, the spring constant k , the driving velocity v_0 and the viscosity η are well determined. Different values for b are

tested, until a good agreement between the experimental and the simulated curve is obtained.

The hydrodynamic force retards the particle, resulting in a **non uniform velocity** $|dh/dt|$ of the sphere during approach and retraction, as confirmed in Figure 28. Data are the same as those presented in Figure 27, where the driving velocity v_0 is $40 \mu\text{m/s}$. The simulation accounts for a slip length b of 8.6 nm .

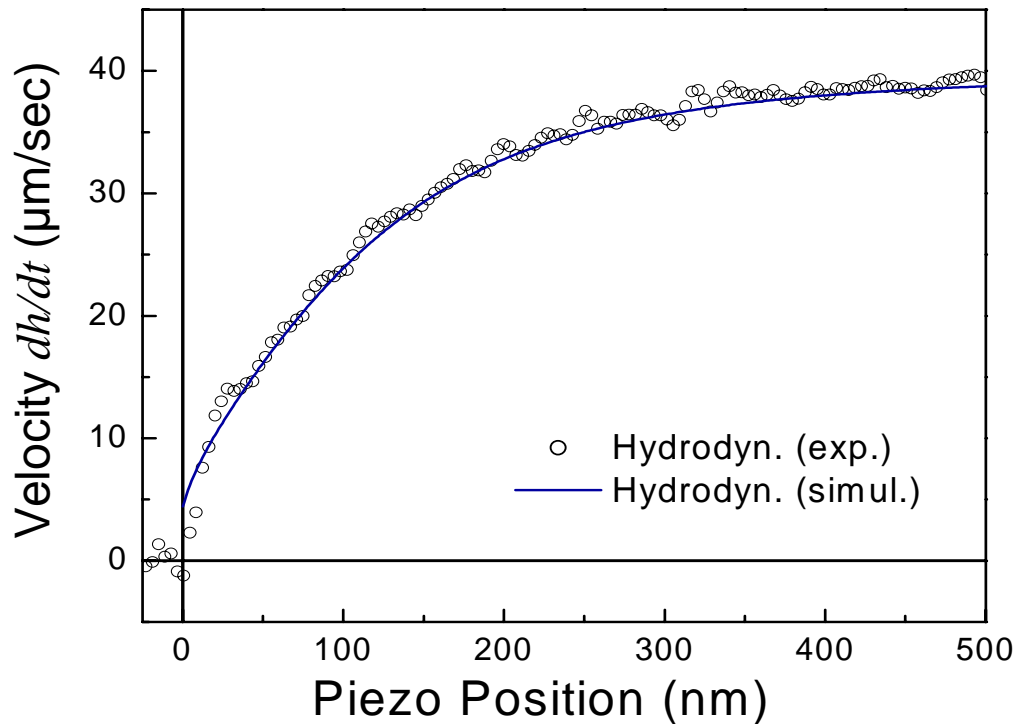
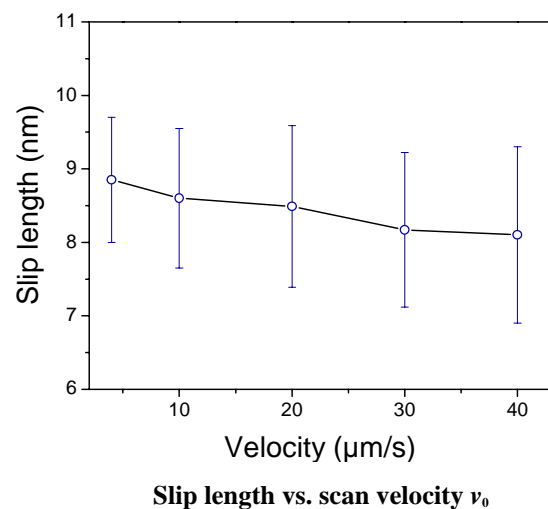


Figure 28: Real velocity of the particle $|dh/dt|$ vs. piezo position for a typical hydrodynamic force curve ($v_0=40 \mu\text{m/s}$, pH 5, 200 mM KCl). The continuous line shows the result of the simulation using eq. (2.16) and a slip length $b = 8.6 \text{ nm}$.

Force curves simulated with the no-slip boundary condition ($f^* = 1$) deviate significantly from measured force curves, especially at distances below 50 nm [see Figure 27]. Even when introducing an additional pre-factor to allow for possible inaccuracies in R or k no agreement is achieved. When correcting for slip and simulating force curves with eq. (2.17), the calculations agree well with experimental



force curves. **Slip lengths** in the order of $b \sim 8.5$ nm (± 1 nm) are obtained. Comparing simulated force curves with experimental ones taken at various velocities further evidences that slip lengths do not significantly depend on the sample scan velocity v_0 within the accuracy of this analysis [see Figure].

It is worth to point out that except for the slip length, all parameters (R , k , l , w) are determined independently: The radius of the particle is measured with a scanning electron microscope and with the AFM. The dimensions of the cantilever are determined with help of scanning electron micrographs and with optical microscopy.

Significant slip lengths of up to 20 nm were also found for by Craig *et al.* [82] in aqueous sucrose solutions (viscosities of 0.01-0.08 Pa·s). They measured hydrodynamic forces between gold coated silica spheres and gold coated mica. The gold surfaces were coated with a self-assembled monolayer of alkanethiols leading to advancing and receding contact angles of 70° and 40° , respectively. In their case, slip lengths increased with viscosity and shear rate. Other authors [83] detected significant slip (175 nm ± 50 nm) for hexadecane on bare saffire, but in this case no dependence of the slip length on the shear rate was observed.

In my measurements I wanted to keep the experimental system as simple as possible. Therefore, I tried to avoid any superfluous uncertainty factors such as the gold/thiol coating (which increases the surface roughness in an uncontrolled way), the use aqueous media with a viscosity different from that of water (sucrose viscosities, e.g., being very temperature sensitive), and the use of partially hydrophobized surfaces (it is indeed a difficult task to determine precisely the wettability of sphere with a radius of 10 μ m).

My experimental results lead to the conclusion that boundary slip occurs, and this slip can be quantified using the slip length. The occurrence of a significant slip length does not necessarily imply slip on the molecular scale. It could also be a hint for a **reduced viscosity**. If the viscosity of the liquid in a surface layer of thickness δ is reduced from its bulk value η to η_s , the effective slip length is given by $b = \delta(\eta/\eta_s - 1)$. Previous experiments with the surface forces apparatus [28, 84] and flow measurements through thin capillaries [85, 86] indicate that the liquid maintains its bulk viscosity down to separations below 10 molecular diameters [29] which is much lower than the here presented slip lengths. Thus, a reduced viscosity obviously is not the reason for slip in my experiments.

Surface roughness could lead to an apparent slip length because the surrounding liquid can still flow out of the gap beside the asperities. To exclude this possibility, an image of the used particle is taken with a commercial AFM in contact mode [Figure 29 and Figure 30]. The roughness of the glass spheres is below 1 nm *rms*. Peak-to-valley distances of sample areas of 1 μm^2 are below 2 nm. The mica sample surface is atomically flat. Thus, surface roughness can not account for the slip lengths obtained.

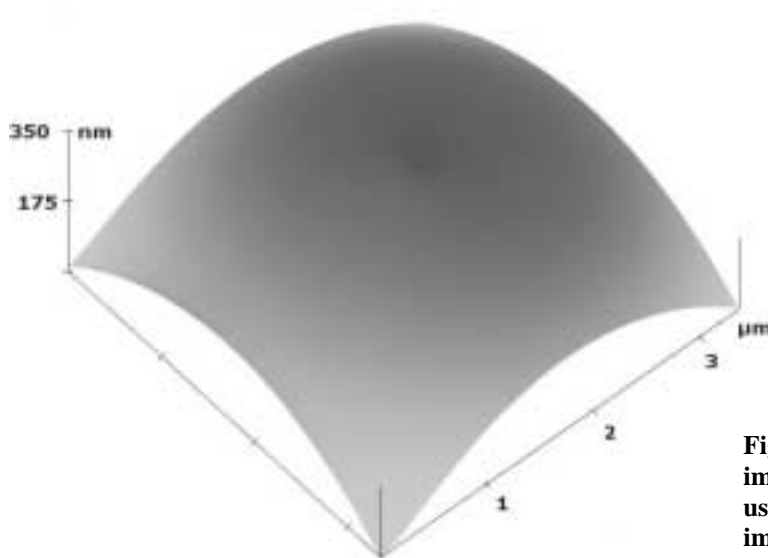


Figure 29: AFM contact mode image of a borosilicate glass sphere used for measurements. From this image the radius of the sphere is determined ($R = 10 \mu\text{m}$).

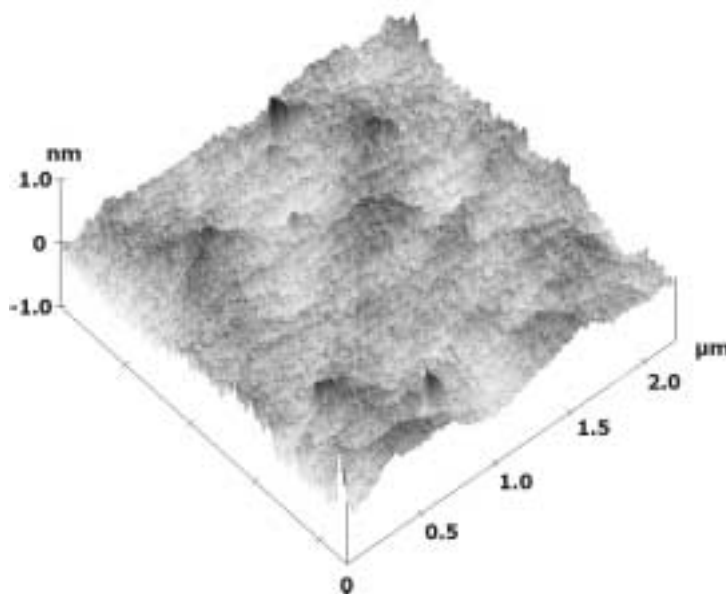


Figure 30: Flattened image of the borosilicate sphere of Figure 29. Roughness is below 1 nm *rms*. Peak to valley distances are below 2 nm

Another reason for slip could be that the surfaces are chemically heterogeneous with different surface energies. Slip on **hydrophobic** surfaces has already been reported [87, 88]. To verify that my surfaces are homogeneously hydrophilic, I determined the receding contact angle Θ_r of my glass particles by **microsphere tensiometry**, measuring the

interaction of the particle with an air bubble in aqueous medium [41, 89]. The result is a zero contact angle, as can be observed in Figure 31. From the force curve, I can deduce that the particle is hydrophilic because it is repelled by the bubble (no jump-in) according to an exponential decay similar to the EDL repulsion law. If the microsphere were partially hydrophobic ($0^\circ < \text{contact angle} < 180^\circ$), I would observe jump-in of the sphere into the bubble.

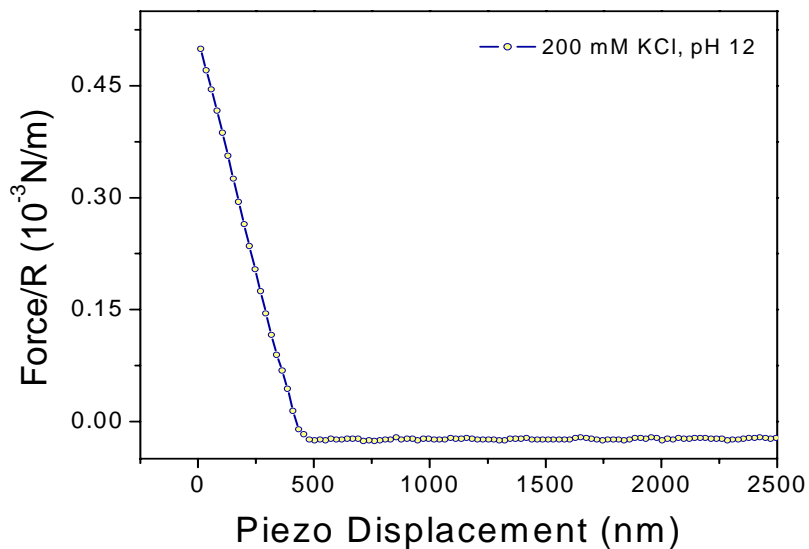


Figure 31: Force-displacement curve for a hydrophilic (zero contact angle) particle, surrounded by electrolyte and interacting with an air bubble. Only each 10th data point is shown.

Additionally, I measured the contact angle on mica with the sessile drop method (Drop Shape Analysis DSA 10, Krüss GmbH, Hamburg, Germany). Again complete wetting was observed.

Why do I detect slip while in previous experiments slip for water on smooth hydrophilic surfaces was never detected? A possible explanation is the **high shear rate**. In the general case, the shear rate $\dot{\gamma}$ is equal to the velocity gradient $\partial \bar{v} / \partial z$. There are hints, according to molecular dynamic simulations of Newtonian liquids under shear, that there exists a general non-linear relationship between the slip at a solid surface and the local shear rate. This leads to the formulation of a general boundary condition relating the degree of slip to the underlying static properties and dynamic interactions of the wall and the fluid [90].

Therefore, I calculated the value of the shear rate in my experiments to figure out when the effects begin to be significant. The shear rate is not uniform in the sphere-wall geometry[see Figure 32]. It is maximal on the surfaces of the sphere and of the sample (at $z = 0$ and $z = h$). In Figure 32 is represented the profile of the shear rate on the sample

surface (at $z = 0$), and in Figure 33 the same profile is represented in a three dimensional simulation. In the simulation, I account for a slip length b of 8 nm. The shear rate is zero on the axis normal to the apex of the sphere and at large distance from this axis, because here the gradient of the velocity is zero.

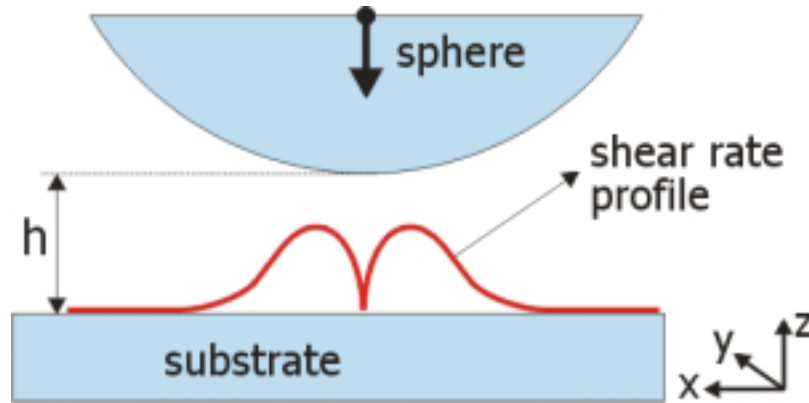


Figure 32: Section of the calculated shear rate profile on the sample interface for the geometrical construction of a sphere approaching a flat surface.

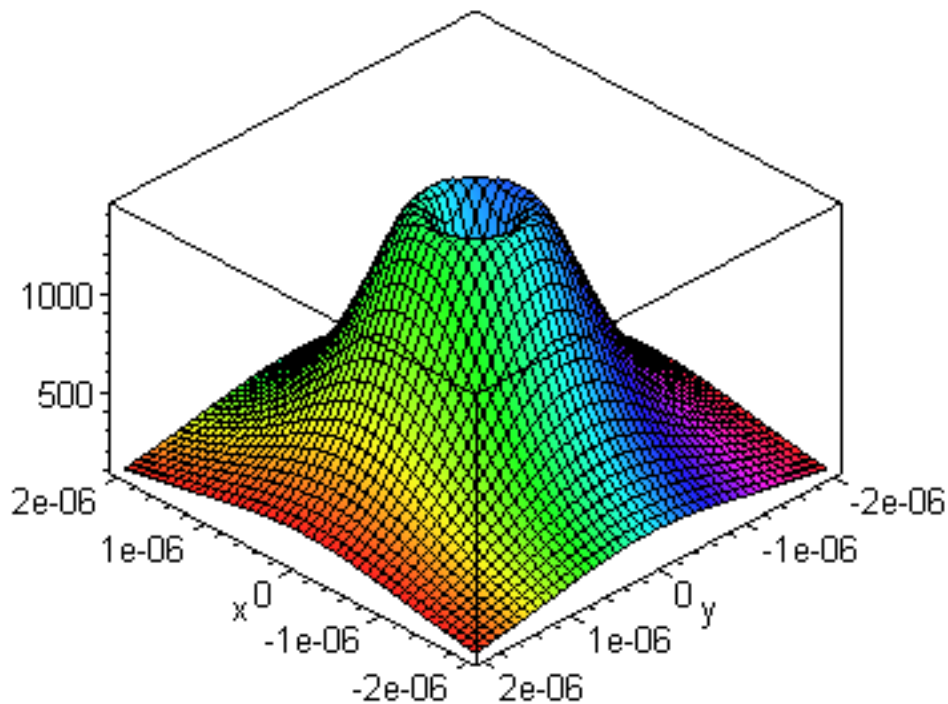


Figure 33: Three dimensional shear rate simulation for a sphere at a distance of 60 nm from a flat surface. The approaching velocity v_0 is 40 $\mu\text{m/s}$ in a liquid having a water-like viscosity η of $0.89 \cdot 10^{-3}$ kg/m/s. The sphere radius R is set to 10 μm . The slip length b is set to 8 nm.

In Figure 34 is represented a sequence of two dimensional sections of shear rate profiles, at various separations between sphere and surface. The parameters are the same as in Figure 33, for separations from 1 to 50 nm.

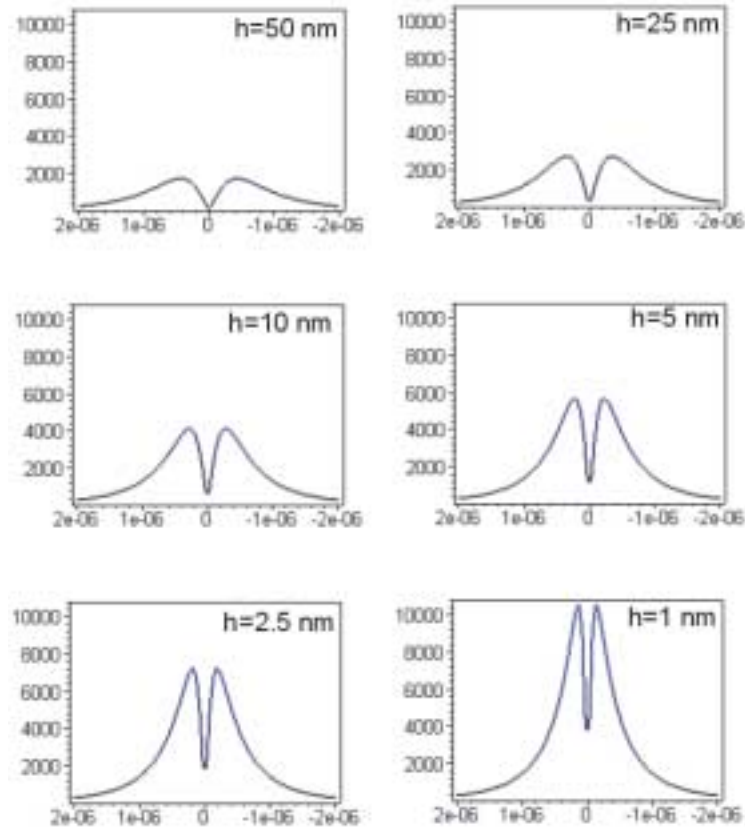


Figure 34: Sequence of transversal cuts of simulated shear rate profiles. The separation between approaching sphere and surface is indicated in each graph.

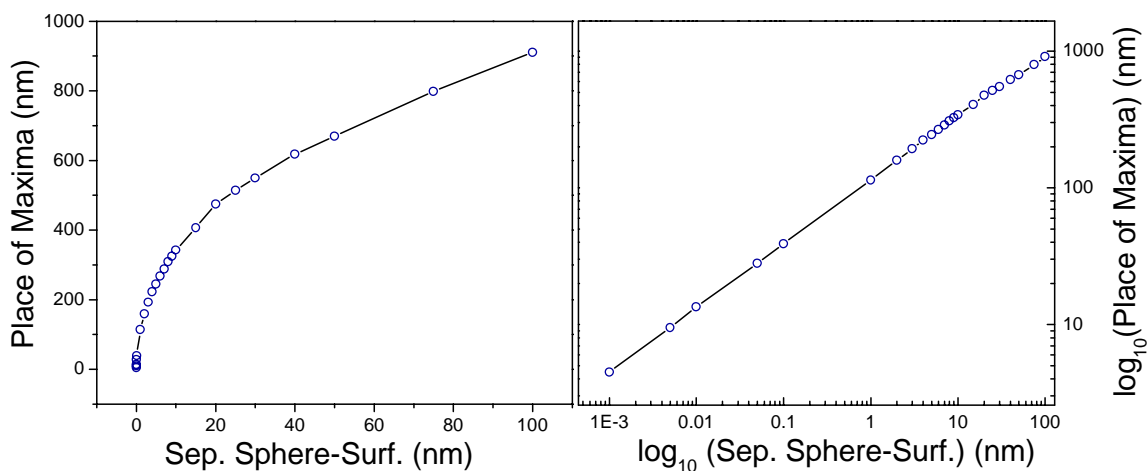


Figure 35: Position of the shear rate maxima with respect to the separation between sphere and surface. The representation on the left is a linear plot, the one on the right a double logarithmic. The linear fit of the logarithmic representation results in a curve of the type $y = px + q$, thus the place of the maxima can be described by a law of the type $y = C_0 \cdot x^p$.

The maxima of the shear rate profiles are located on a "circle", representing the symmetry of the spherical colloidal particle [see Figure 33]. The law that describes the position of the maxima with respect to the distance of the sphere from the surface is of the type $y = C_0 \cdot x^p$, where C_0 is a constant and p is the slope of the line resulting from the double logarithmic representation [see Figure 35].

The absolute value of the **maximal shear rate** for water can be derived by my simulations [see Figure 34], or calculated with an expression derived by Horn et al. [91] and taking into account that the velocity of the particle decreases from v_0 at large distance to zero for $h \rightarrow 0$. Typical shear rates at the distance $h = 1$ nm are 6500 s^{-1} for $v_0 = 20 \text{ }\mu\text{m/s}$ and 10500 s^{-1} for $v_0 = 40 \text{ }\mu\text{m/s}$, for a slip length of 8 nm [see Figure 36]. If I exclude slip, even higher shear rates (up to two

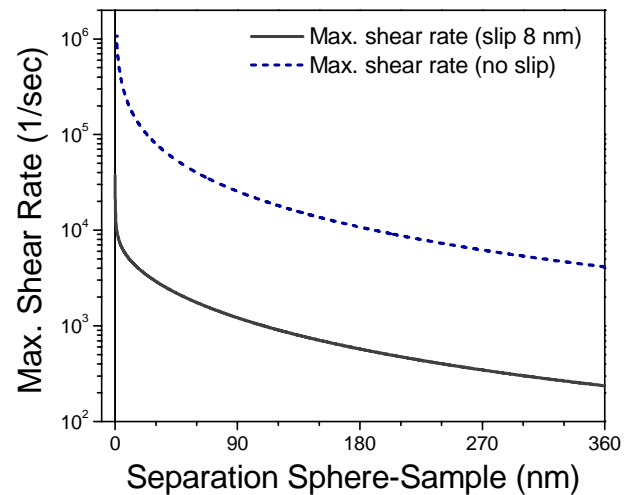


Figure 36: Calculation of maximal shear rate vs. separation between sphere and sample, according to [91]. $v_0 = 40 \text{ }\mu\text{m/s}$ in water (viscosity $\eta = 0.89 \cdot 10^{-3} \text{ kg/m/s}$), sphere radius $R = 10 \text{ }\mu\text{m}$

orders of magnitude) result. In previous hydrodynamic experiments with the surface force apparatus [28, 84, 91], the AFM [82] or thin capillaries [92] the applied shear rates were significantly lower. This might be the reason why no evidence of slip has been observed there.

4.4 The Electrostatic Force

A set of electrostatic force curves is presented in Figure 37. The measurements are performed in an electrolyte solution of KOH 1.5 mM, at pH 12. The spring constant is $k = 0.0116 \text{ N/m}$. Only the approach of the force curve is shown, the retraction curve being identical. The scan velocity v_0 of the piezo is $0.2 \text{ }\mu\text{m/s}$. In the picture, three single force curves (taken under the same experimental conditions after 20 and 40 seconds) are shown. These curves exhibit the characteristic exponentially decaying EDL repulsion. The fit of the first of the curves shows a Debye length λ_D of 8.1 nm, whereas the calculated Debye length for a 1.5 mM 1:1 electrolyte solution is $\lambda_D = 7.8 \text{ nm}$. Also the simulations for the

constant charge and the constant potential models [93] which fit best the experimental data are shown. Values for the surface charge density σ of $8.0 \cdot 10^{-3} \text{ C/m}^2$ and for the surface potential Ψ_0 of 93 mV have been used. With Grahame's formula one can find that if the surface charge is set to $8.0 \cdot 10^{-3} \text{ C/m}^2$, a surface potential of 89 mV results; if the surface potential is set to 93 mV, a surface charge of $8.3 \cdot 10^{-3} \text{ C/m}^2$ results. These results can be viewed as a cross-check for the consistency of the simulated data. I can deduce from Figure 37 that the constant charge model fits the data better when the separation decreases to zero.

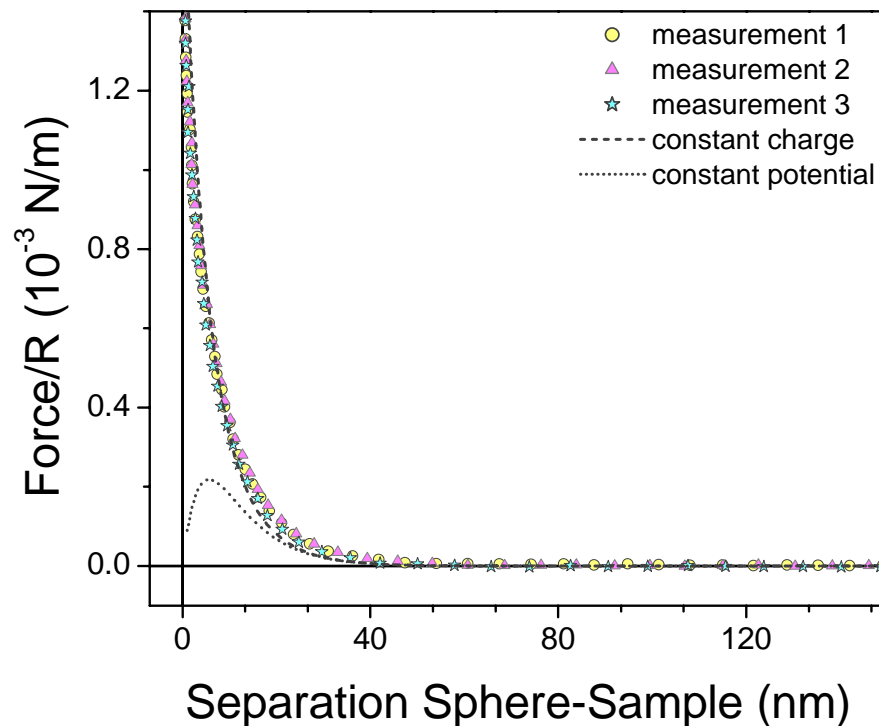


Figure 37: Three experimental electrostatic force curves, a constant charge and a constant potential simulation. The electrolytic solution has a concentration of 1.5 mM and the scan velocity was set to $v_0 = 0.2 \mu\text{m/s}$. The theoretical Debye length is 7.8 nm, the experimentally determined is 8.1 nm. The constant potential model gives a best fit using $\Psi_0 = 93 \text{ mV}$, the constant charge model fits best using a surface charge $\sigma = 8.0 \cdot 10^{-3} \text{ C/m}^2$.

For comparison, in Figure 38 a force curve recorded with a low speed ($v_0 = 0.15 \mu\text{m/s}$) at pH 5 in 200 mM monovalent salt (KI) is shown together with a typical curve recorded under the above conditions of Figure 37 (low speed: $v_0 = 0.2 \mu\text{m/s}$; high pH: pH 12 in 2 mM KOH).

At high electrolyte concentration, the EDL force is negligible for distances larger than 2 nm. Fitting this curve with a decaying exponential leads to decay lengths λ_d of about 0.4 nm, whereas the expected decay length λ_d is 0.7 nm. Fitting the curve at low electrolyte

concentration with a single exponential leads to decay lengths λ_D of about 6.4 nm, which agrees with the expected Debye length λ_D of 6.4 nm.

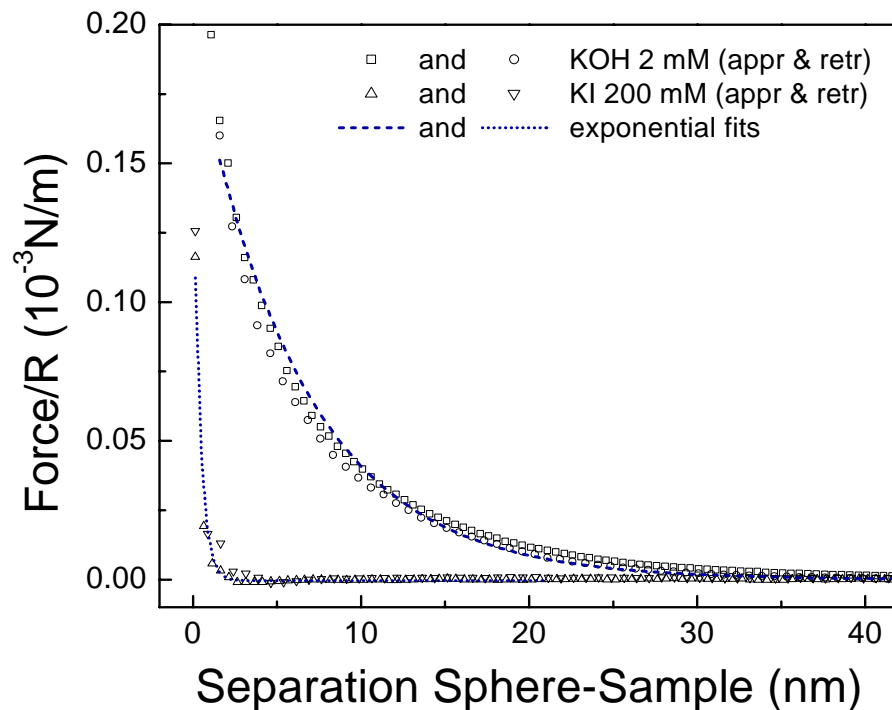


Figure 38: Comparison between two force curves at high (200 mM) and low (2 mM) electrolyte concentration, and corresponding exponential fits.

4.5 The Electrokinetic Force

Electrokinetic forces are more repulsive than electrostatic or hydrodynamic forces upon approach and retract [see Figure 39]. When retracting the sample, the electrostatic repulsion decreases the apparent hydrodynamic attractive force. Similar results are obtained for different 1:1 electrolytes (NaCl, KCl, KOH, NaOH, and KI). Hence, the effect does not seem to depend on the ionic species as expected.

Electrokinetic forces are less repulsive than the sum of the corresponding hydrodynamic and electrostatic forces in the approaching and retracting part [see Figure 39]:

$$F_{ek} < F_{hy} + F_{es}$$

Thus, **hydrodynamic** and **electrostatic** double layer forces are **not additive**. Why do hydrodynamic and electrostatic double layer forces not simply add to give the electrokinetic force?

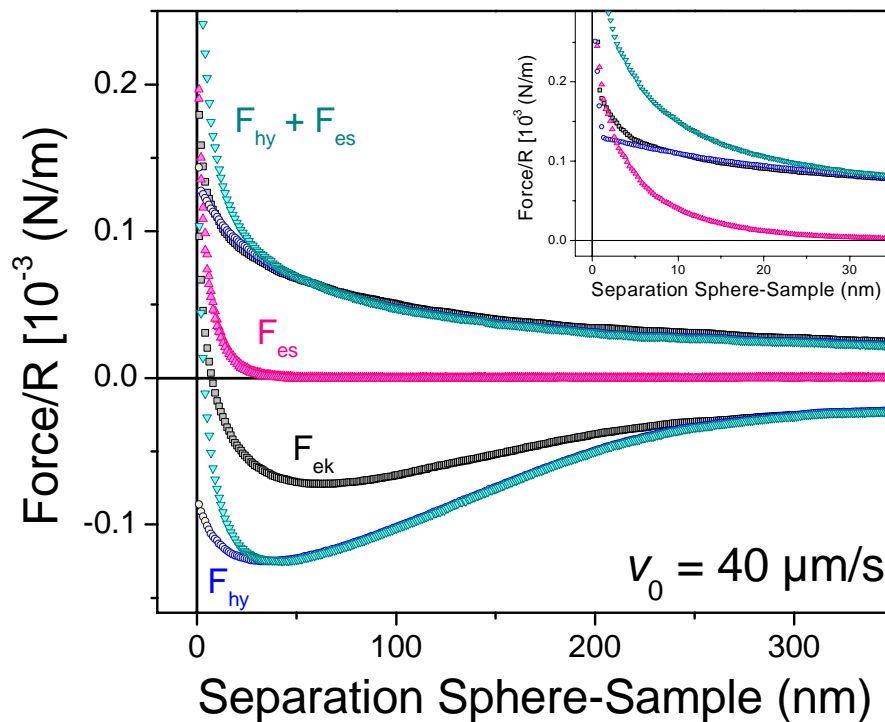
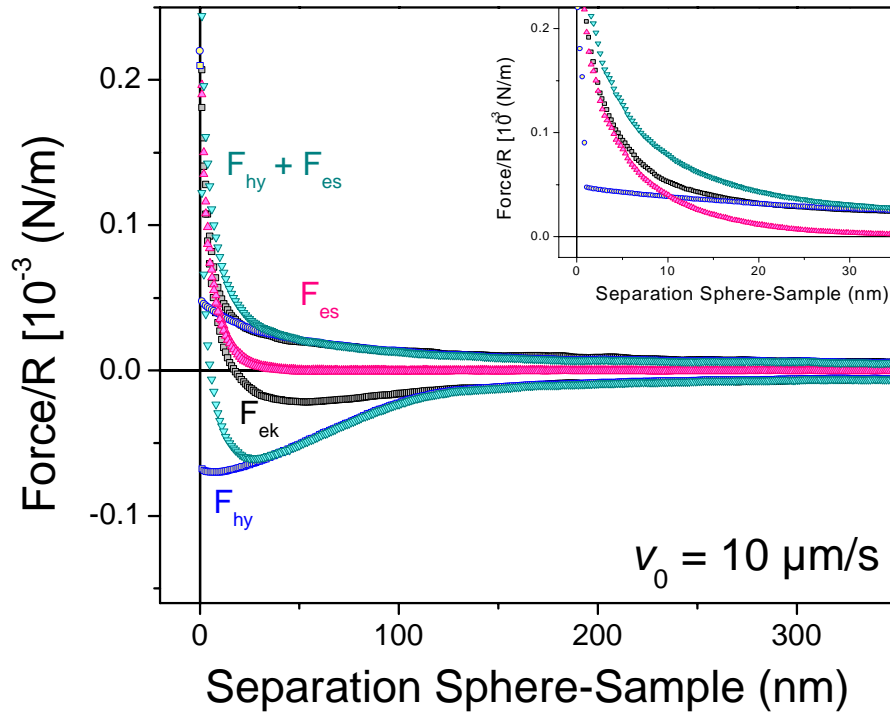


Figure 39: Normalised experimental electrostatic F_{es} ($v_0 = 0.2 \mu\text{m/s}$, pH 11, 2 mM KOH) and electrokinetic F_{ek} ($v_0 = 10 \mu\text{m/s}$ upper graph, $v_0 = 40 \mu\text{m/s}$ lower graph, pH 11, 2 mM KOH) force curves (approach and retraction, insert: approach in detail). For comparison, also the hydrodynamic force F_{hy} ($v_0 = 10 \mu\text{m/s}$ upper part, $v_0 = 40 \mu\text{m/s}$ lower part, pH 5, 200 mM KCl) taken with the same microsphere ($R = 10 \mu\text{m}$) and cantilever ($l = 210 \mu\text{m}$, $w = 52.5 \mu\text{m}$) is shown. In the range of the EDL the sum of the electrostatic and hydrodynamic force, ($F_{hy} + F_{es}$) is higher than the electrokinetic force, showing the non-additivity of the hydrodynamic and electrostatic forces.

When the particle approaches a charged surface and encounters an electrostatic repulsion its velocity $|dh/dt|$ decreases. The velocity in the presence of an electrostatic repulsion is lower than without a double layer [Figure 40]. This simultaneously reduces the hydrodynamic force, which depends on the velocity, and thus the total interaction. This explains the lower electrokinetic force, if compared with the sum of the hydrodynamic and the electrostatic forces.

Simulations of velocity curves [Figure 40] show again an excellent agreement assuming a realistic slip length of $b \sim 8.5$ nm [see also Figure 28]. For comparison, the simulation of the hydrodynamic velocity assuming no slip is also shown. This curve differs strongly from the simulation accounting for slip.

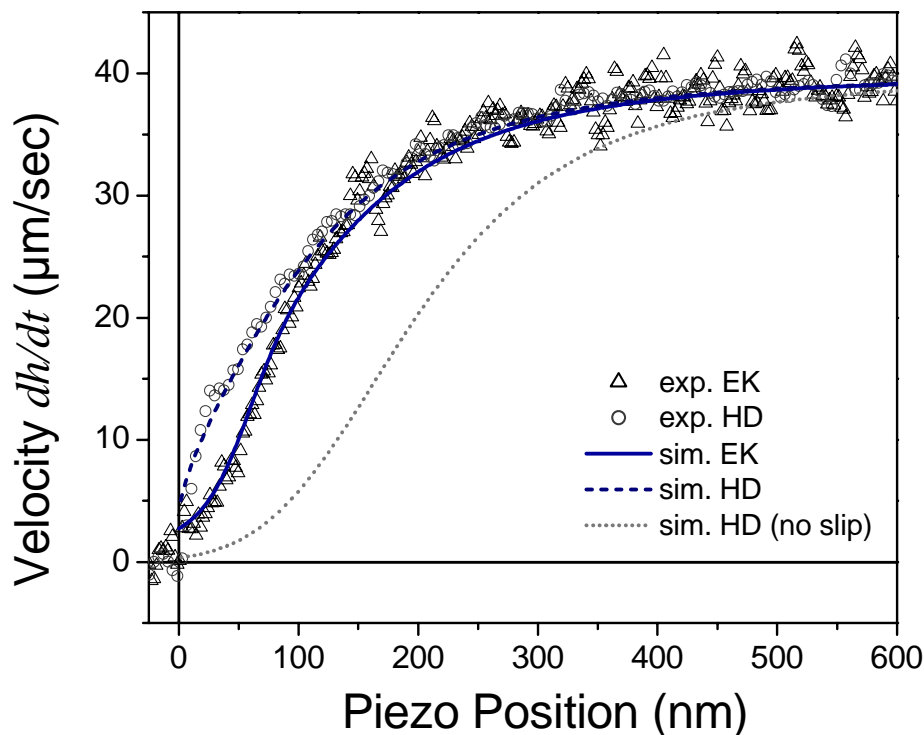


Figure 40: Real velocity of the particle $|dh/dt|$ vs. piezo position for a typical hydrodynamic (exp. HD) force curve ($v_0 = 40$ $\mu\text{m/s}$, pH 5, 200 mM KCl) and an electrokinetic (exp. EK) force curve ($v_0 = 40$ $\mu\text{m/s}$, pH 11, 2 mM KOH) recorded with the same particle. The lines (continuous, dashed, dotted) show results of simulations using eq. (2.13) for the hydrodynamic (sim. HD) case. Electrokinetic (sim. EK) velocities are simulated with eq. (2.17). Only each fourth data point is displayed.

In Figure 41 experimental and simulated hydrodynamic (HD), electrostatic (ES) and electrokinetic (EK) force curves, plus the sum of the hydrodynamic and the electrostatic curves (HD + ES) are presented together. Generally, there is a good agreement between the measured and the calculated curves. I conclude that **no special electrokinetic effects** are present up to shear rates of typically 10^4 s^{-1} and that the electric double layer does not change its structure.

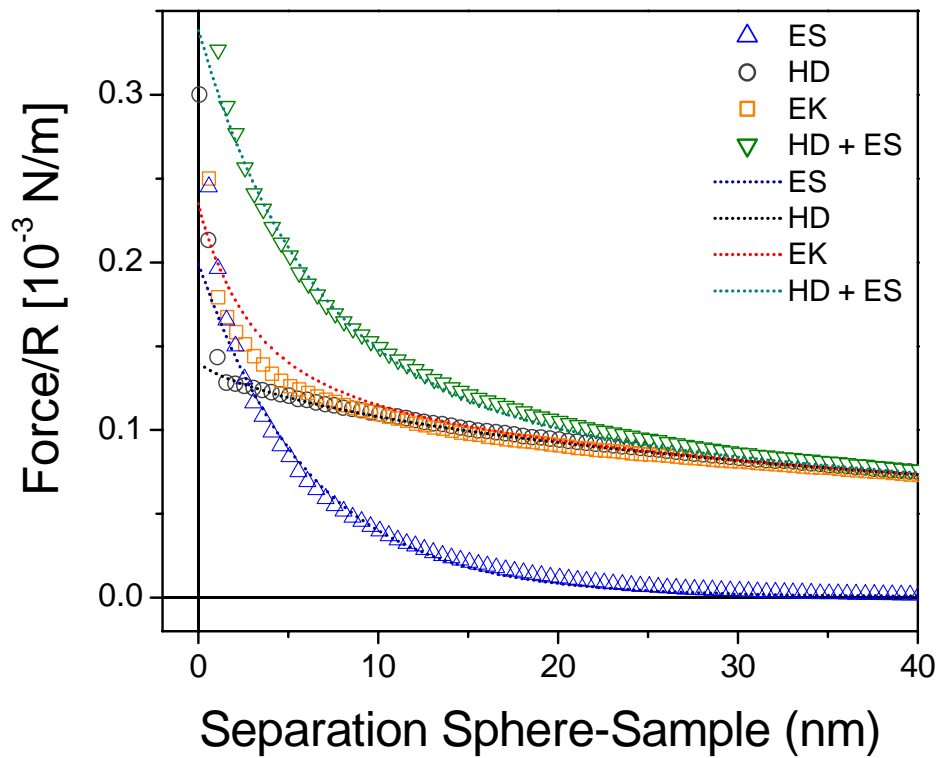


Figure 41: Comparison between experimental (Δ , \circ , ∇ and \square) and simulated (dashed lines) force curves (approach only). The radius of the microsphere is $R = 10 \mu\text{m}$. Liquid viscosity is assumed to be $\eta = 0.89 \cdot 10^{-3} \text{ kg/m/s}$. Rectangular poly-silicon cantilever dimensions are $l = 210 \mu\text{m}$ and $w = 52.5 \mu\text{m}$. The hydrodynamic force curve is taken in 200 mM KCl at pH = 5 with $v_0 = 40 \mu\text{m/s}$, the electrostatic force curve in KOH 2 mM at pH 11 with $v_0 = 0.2 \mu\text{m/s}$, the electrokinetic force curve in KOH 2 mM at pH 11 with $v_0 = 40 \mu\text{m/s}$.

Conclusions

In this work I investigate hydrodynamic, electrostatic and electrokinetic effects on a hydrophilic micrometer-sized sphere approaching a flat hydrophilic solid surface in water with varying velocities (from $0.15 \mu\text{m/s}$ to $40 \mu\text{m/s}$) by means of a modified AFM. This instrument is called PIA, and it was developed and built in our group. By means of laser beam deflection, it allows to detect the bending of a tiny cantilever against which a sample surface is pushed. A microsphere is fixed at the free end of the cantilever, so that the force acting between the flat surface and the particle is measured as a function of their separation. These measurements are called "force curves. By adjusting the ionic strength and the pH of the water and the particle's velocity it was possible to distinguish between electrostatic, hydrodynamic and electrokinetic interactions.

For the force measurements presented here, I designed and attended the production of my own cantilevers (IMM, Mainz). I achieved a high sensitivity and flexibility of the sensors using rectangular beams of different geometries and different spring constants, preferably without a reflective metal coating on their back side. The **design** involved knowledge of CAD software, of the theory on the bending of plates and of the properties of cantilever materials. The **fabrication** involved knowledge on silicon micro machining processes.

For a pure hydrodynamic approach of the particle (high velocity, high salt concentration, low pH), my investigations show that a slip of the surface adjacent water layers has to be considered for large shear rates. Typically measured **slip lengths** were in the order of 8.5 nm ($\pm 1 \text{ nm}$). It is independent on the shear rate in the considered range of velocities, from $0.15 \mu\text{m/s}$ up to $40 \mu\text{m/s}$. These results are in excellent agreement with theoretically derived boundary conditions which more realistically allow for a slip of fluids with a finite velocity on the adjacent solid.

The analysis of electrokinetic force curves (high velocity, low salt concentration, high pH) show that this force is always less than the sum of the pure hydrodynamic and the pure electrostatic force. Simulations of these force curves show that a correct description must already include electrostatic effects at the stage of formulation of the equations of hydrodynamic motion. I explain these findings by the presence of an electrostatic repulsion reducing the particle velocity and thus diminishing the hydrodynamic drag on it. Moreover,

even at high particle velocities (shear rate up to 10^4 s^{-1}) the resulting force curves in the presence of long range electrostatic forces could satisfactorily be simulated assuming a **static** double layer. Hence, it keeps its structure even at high shear rate.

Bibliography

1. B.V.Derjaguin, L.D.Landau, JETP 11, 802 (1941)
2. B.V.Derjaguin, L.D.Landau, Acta Phys. Chim. URSS 14, 633 (1941)
3. E.J.W.Verveij, J.Th.G.Overbeek, Theory of the stability of lyophobic colloids, Elsevier (1948)
4. C.Huh, L.E.Scriven, J. Colloid Interface Sci. 35, 85 (1971)
5. L.M.Hocking, J. Fluid Mech. 76, 801 (1976)
6. E.B.Dussan, Annu. Rev. Fluid Mech. 11, 371 (1979)
7. J.Koplik, J.R.Banavar, J.F.Willemsen, Phys. Rev. Lett. 60, 1282 (1988)
8. P.A.Thompson, M.O.Robbins, Phys. Rev. Lett. 63, 766 (1989)
9. P.A.Thompson, W.B.Brinkerhoff, M.O.Robbins, J. Adhesion Sci. Technol. 7, 535 (1993)
10. H.K.Moffatt, J. Fluid Mech. 18, 1 (1964)
11. J.Koplik, J.R.Banavar, Phys. Fluids 7, 3118 (1995)
12. S.Richardson, J. Fluid Mech. 59, 707 (1973)
13. L.M.Denn, Annu. Rev. Fluid Mech. 22, 13 (1990)
14. T.Dabros, T.G.M.van de Ven, Colloid Polym. Sci. 261, 649 (1983)
15. J.N.Israelachvili, Intermolecular and Surface Forces, Academic Press, London (1992)
16. R.J.Hunter, Foundations of Colloid Science, Vol I+II, Clarendon Press, Oxford (1995)
17. P.Debye, Physik. Zeitschr. 21, 178 (1920)
18. W.H.Keesom, Physik. Zeitschr. 22, 129 (1921)
19. F.London, Zeitschr. f. Physik 63, 17 (1930)
20. J. Mahanty, B.W. Ninham, Dispersion Forces, New York, Academic Press (1976)
21. G.Gouy, Journ. de Phys. 9, 457 (1910)
22. D.L.Chapman, Phil. Mag. 25, 475 (1913)
23. G.Gouy, Ann. Phys. 7, 129 (1917)
24. P.Debye, E.Hückel, Physik. Zeitschrift 24, 185 (1923)
25. V.A.Parsegian, D.Gingell, Biophys. J. 12, 1192 (1972)
26. B.V.Derjaguin, Koll. Zeitschrift 69, 155 (1934)
27. H.Brenner, Chem. Eng. Sci. 16, 242 (1961)
28. D.Y.C.Chan, R.G.Horn, J. Chem. Phys. 83, 5311 (1985)
29. O.I. Vinogradova, Langmuir 11, 2213 (1995)
30. P.G.de Gennes, C.R. Acad. Sci. B 288, 219 (1979)
31. R.J Hunter, Zeta potential in colloid science, Principles and applications, Academic Press, London (1981)
32. S.S.Dukhin, B.V.Derjaguin, Elektrokinetic phenomena, in E.Matijevic (Ed.), Surface and Colloid Science, Vol.7, John Wiley Interscience, New York (1974)
33. T.G.M.van de Ven, Colloidal hydrodynamics, Academic Press, London (1989)
34. T.G.M.van de Ven, J. Colloid Interface Sci. 124, 138 (1988)
35. S.G.Bike, D.C.Prieve, J. Colloid Interface Sci. 136, 95 (1990)
36. P.M.Claesson, T.Ederth, V.Bergeron, M.W.Rutland, Adv. Colloid Interface Sci. 67, 119 (1996)
37. D.Tabor, R.H.S.Winterton, Nature 219, 1120 (1968)
38. J.N.Israelachvili, D.Tabor, Proc. Roy. Soc. London A 331, 19 (1972)
39. J.N.Israelachvili, G.E.Adams, J. Chem. Soc. Faraday Trans. I 74, 975 (1978)
40. G.Binnig, C.F.Quate, C.Gerber, Phys. Rev. Lett. 56, 930 (1986)
41. M.Preuss, H.-J.Butt, Langmuir 14, 3164 (1998)
42. W.A. Ducker, T.J. Senden, R.M. Pashley, Nature 353, 239 (1991)
43. H.J. Butt, Biophys. J. 60, 1438 (1991)
44. D.E.Aston, J.C.Berg, J. Colloid Interface Sci. 235, 162 (2001)
45. D.Y.C.Chan, R.R.Degastine, L.R.White, J. Colloid Interface Sci. 236, 141 (2001)
46. V.S.J.Craig, A.M.Hyde, R.M.Pashley, Langmuir 12, 3557 (1996)
47. J.L.Parker, Langmuir 8, 551 (1992)
48. W.A. Ducker, T.J. Senden, R.M. Pashley, Langmuir 8, 1831 (1992)
49. M.Preuss, H.-J.Butt, Langmuir 14, 3164 (1998)
50. R.Raiteri, M.Preuss, M.Grattarola, H.-J.Butt, Colloids Surfaces A 136, 191 (1998)
51. J.L Hutter, J. Bechhoefer, Rev. Sci. Instr. 64 (7), 1868 (1993)
52. J.P.Cleveland, S.Manne, D.Bocek, P.K.Hansma, Rev. Sci. Instrum. 64 (2), 403 (1993)
53. D.Walters, J.Cleveland, et al., Rev. Sci. Instrum. 67 (10), 3583 (1996)
54. J.E. Sader, Rev. Sci. Instrum. 70 (10), 3967 (1999)

55. A.Torii, M.Sasaki, K.Hane, S.Okuma, *Meas. Sci. Technol.* 7 (2), 179 (1996)
56. M.Tortonese, M.Kirk, *Proc. SPIE* 3009, 53, (1997)
57. J.E.Sader, I.Larson, P.Mulvaney, L.R.White, *Rev. Sci. Instrum.* 66 (7), 3789 (1995)
58. J.E. Sader, *J. Appl. Phys.* 84, 64 (1998)
59. B.Cappella, G.Dietler, *Surface Science Reports* 34, 1, (1999)
60. D.Sarid, *Scanning Force Microscopy*, Oxford University Press (1991)
61. H.W.Hao, A.M.Baro, J.J.Saenz, *J.Vac. Sci. Tech. B* 9, 1323 (1991)
62. O.I.Vinogradova, H.-J.Butt, G.E.Yakubov, F.Feuillebois, *Rev. Sci. Instrum.* 72 (5), 2330 (2001)
63. N.Meda, T.Senden, *Langmuir* 16, 9282 (2000)
64. B.E.Conway, J.O'M.Bockris, I.A.Ammar, *Trans. Faraday Soc.* 47, 756 (1951)
65. H.-J.Butt, P.Siedle, K.Seifert, K.Fendler, T.Seeger, E.Bamberg, A.L.Weisenhorn, K.Goldie, A.Engel, *Journal of Microscopy* 169 (1) 75 (1992)
66. T.R.Albrecht, S.Akamane, T.E.Carver, C.F.Quate, *J. Vac. Sci. Technol. A* 8 (4), 3386 (1990)
67. J.E.Sader, *Rev. Sci. Instrum.* 66 (9), 4583 (1995)
68. M.Tortonese, R.C.Barrett, C.F.Quate, *Appl. Phys. Lett.* 62 (8), 834 (1992)
69. A.Boisen, *Passive & Active AFM Probes*, Industrial Ph.D. Project Thesis, ISBN: 87-89935-06-3 (1997)
70. D.Maier-Schneider, A.Köprülü, S.Ballhausen Holm, E.Obermeier, *J. Micromech. Microeng.* 6, 436 (1996)
71. W.Menz, J.Mohr, *Mikrosystemtechnik für Ingenieure*, Wiley-VCH (1997)
72. P.Warszynski, *Adv. Colloid Interface Sci.* 84, 47 (2000)
73. H.Hertz, *Reine Angew. Math.* 92, 156 (1881)
74. J.N.Sneddon, *Int. J. Eng. Sci.* 3, 47 (1965)
75. B.V.Derjaguin, V.M.Muller, Yu.P.Toporov, *J. Colloid Interface Sci.* 56, 314 (1975)
76. K.L.Johnson, K.Kendall, A.D.Roberts, *Proc. Roy. Soc. London A* 324, 301 (1974)
77. D.Maugis, *J. Colloid Interface Sci.* 150, 243 (1992)
78. R.P.Abendroth, *J. Colloid Interface Sci.* 34 (4), 591 (1970)
79. J.H.Hoh, A.Engel, *Langmuir* 9, 3310 (1993)
80. P.I.Oden, G.Y.Chen, R.A.Steele, R.J.Warmack, T.Thundat, *Applied Physical Letters* 68, 3814 (1996)
81. N.Maeda, T.J.Senden, *Langmuir* 16, 9282 (2000).
82. J.N.Israelachvili, *J. Colloid Interface Sci.* 110, 263 (1986)
83. R.Pit, H.Hervet, L.Leger, *Phys. Rev. Lett.* 85 (5), 980 (2000)
84. B.V.Derjaguin, V.V.Karasev, *Surface Colloid Sci.* 15, 221 (1993)
85. J.M.Macaulay, *Nature* 139, 587 (1936)
86. V.S.J.Craig, C.Neto, and D.R.M.Williams, *Phys. Rev. Lett.* 87 (5), 054504-1 (2001)
87. O.I.Vinogradova, *Langmuir* 14, 2827 (1998)
88. J.-L.Barrat, L.Bocquet, *Phys. Rev. Letters* 82 (23), 4671 (1999)
89. S.Ecke, M.Preuss, H.-J.Butt, *J. Adhesion Sci. Technol.* 13, 1181 (1999)
90. P.A.Thompson, S.M.Troian, *Nature* 389, 360 (1997)
91. R.G.Horn, O.I.Vinogradova, M.E.Mackay, N.Phan-Thien, *J. Chem. Phys.* 112, 6424 (2000)
92. N.V.Churaev, V.D.Sobolev, and A.N.Somov, *J. Colloid Interface Sci.* 97, 574 (1984)
93. H.-J.Butt, *Nanotechnology* 3, 60 (1992)

Acknowledgements

This thesis would not appear in its present form without the kind assistance and support of the following individuals and organizations:

Professor Hans-Jürgen Butt, without whom this thesis would not have seen the light. Thanks to his precious suggestions, his interest and his personal commitment the thesis has also seen an ending!

Dr. Roberto Raiteri, who introduced me to the world of AFM and to the (well hidden) secrets of the bending of cantilevers.

The people of the Nanotechnology department at IMM (Oliver Haverbeck, Bernd Limburg, Heiko Prüßner, Uwe Rietzler, Felix Schmitz and Michael Stepputat) for all practical suggestions and technical advice during the first two years of my PhD. Above all, however, for the good feeling always present in the group!

The people in the group of Prof. Butt, for the friendly atmosphere during these years, for all the coffee we had together and for keeping up the "self-aid group" to resist the terrible food of the cafeteria in Mainz. My thanks go to: Simona Loi, Volker Franz, Stefan Ecke, Gleb Yakubov, Dr. Karlheinz Graf, Dr. Michael Kappl and Dr. Markus Preuß. Thanks also to the technical staff of the group: Peter Rickert, Hanne Christian and Brigitte Niesenhaus, and to our secretary Annelie Schäfer.

Bernd Limburg (IMM), Volker Franz and Christoph Reiner (AK Prof. Deiseroth), for the SEM pictures of the cantilevers and the microspheres.

Markus Preuß for all the preparatory work he did on PIA. Michael Kappl, Stefan Ecke and Roberto Raiteri for the refinements.

Prof. Butt, Volker Franz, Michael Kappl, Roberto Raiteri and above all Karlheinz Graf for taking their time to read the drafts of this work and give me good advices.

Simona Loi for persistent Italian speaking, so that I really felt like home!

The Foundation for Innovation and Research of Rhineland-Palatinate for financing the first two years of this PhD, the Institute for Microtechnology Mainz for providing the facilities.

Dedication

This thesis is dedicated to my family and to my sister Cristina, without whom none of this would have been even possible. It is especially dedicated to Corinna for her invaluable support (she knows what!) during the last two years.

To all the good friends, wherever they are!

Dedica

Questa tesi e' dedicata alla mia famiglia e a mia sorella Cristina, senza i quali nulla di questo sarebbe stato possibile. E' in special modo dedicata a Corinna per il suo prezioso sostegno (lei sa di che parlo!) durante questi ultimi due anni.

A tutti i veri amici, dovunque si trovino!

List of used mathematical symbols, constants and abbreviations

A_{AB}	Hamaker constant [J]
C	interaction constant [Jm^6]
E	electric field strength [V/m], or elastic (or Young) modulus [N/m^2]
F	force [N]
H	distance [m]
M	concentration [mol/l]
P	pressure [N/m^2]
Q	charge [C]
Q_f	quality factor of a cantilever
R	particle radius [m]
Re	Reynolds number
T	temperature [K], optical transmission
U	voltage [V]
V	potential energy [J]
W	electric work [J]
a	cantilever thickness [m]
b	slip length [m]
c	aqueous solute concentration [mol/l], or light speed in vacuum [$2.998 \cdot 10^8$ m/s]
d	distance [m], or derivative
e	exponential function
f	electrostatic force per unit area [N/m^2]
h	distance [m], or Planck constant [$6.626 \cdot 10^{-34}$ Js]
k	spring constant [N/m]
k_B	Boltzmann constant [$1.381 \cdot 10^{-23}$ J/K]
l	cantilever length [m]
m	mass [kg]
n_i	local ion density [particles/ m^3]
q_e	electronic elementary charge [$-1.602 \cdot 10^{-19}$ C]
t	time [s]
v	velocity [m/s]
w	cantilever width [m]

∂	partial derivative
α	polarizability [$\text{C}^2\text{m}^2/\text{J}$]
δ	layer thickness, or distance [m]
ϵ	relative permittivity
ϵ_0	permittivity of free space [$8.854 \cdot 10^{-12}$ C ² /J/m]
γ	surface tension [N/m]
η	viscosity [kg/m/s]
κ	Debye-Hückel parameter ($\kappa^{-1} = \lambda_D$) [1/m]
λ_D	Debye length [m]
μ	dipole moment [Cm]
π	Pi (3.1415...)
ρ	material density [kg/m^3]
ρ_e	electric charge density [C/m^3]
σ	surface charge density [C/m^2]

ν frequency [Hz]
 ω radial frequency [1/s]
 Ψ electrostatic potential [V]
 Ψ_0 electrostatic surface potential [V]
 $\Gamma(\omega)$ hydrodynamic function

AFM atomic force microscope
ASE advanced silicon etching
BHF buffered fluoridric acid
CVD chemical vapour deposition
DLVO Derjaguin, Landau, Verwey, Overbeek
DSP double side polished (of silicon wafer)
EDL electric double layer
LFM lateral force microscopy
LPCVD low pressure chemical vapour deposition
PECVD plasma enhanced chemical vapour deposition
PIA particle interaction apparatus
PSD position sensing device
PVD physical vapour deposition
RIE reactive ion etching
SFA surface force apparatus
vdW van der Waals
